

Accepted for publication in the Astrophysical Journal
07/11/08

X-ray flares in Orion young stars. I. Flare characteristics

Konstantin V. Getman¹, Eric D. Feigelson¹, Patrick S. Broos¹, Giuseppina Micela², Gordon P. Garmire¹

gkosta@astro.psu.edu

ABSTRACT

Pre-main sequence (PMS) stars are known to produce powerful X-ray flares which resemble magnetic reconnection solar flares scaled by factors up to 10^4 . However, numerous puzzles are present including the structure of X-ray emitting coronae and magnetospheres, effects of protoplanetary disks, and effects of stellar rotation. To investigate these issues in detail, we examine 216 of the brightest flares from 161 PMS stars observed in the Chandra Orion Ultradeep Project (COUP). These constitute the largest homogeneous dataset of PMS, or indeed stellar flares at any stellar age, ever acquired. Our effort is based on a new flare spectral analysis technique that avoids nonlinear parametric modeling. It can be applied to much weaker flares and is more sensitive than standard methods. We provide a catalog with > 30 derived flare properties and an electronic atlas for this unique collection of stellar X-ray flares. The current study (Paper I) examines the flare morphologies, and provides general comparison of COUP flare characteristics with those of other active X-ray stars and the Sun. Paper II will concentrate on relationships between flare behavior, protoplanetary disks, and other stellar properties.

Several results are obtained. First, the COUP flares studied here are among the most powerful, longest, and hottest stellar X-ray flares ever studied. Peak luminosities are in the range $31 < \log L_{X,pk} < 33$ erg s $^{-1}$; rise (decay) timescales range from 1 hour to 1 day (few hours to 1.5 days); many peak temperatures exceed 100 MK. The scale of their inferred associated coronal structures is

¹Department of Astronomy & Astrophysics, 525 Davey Laboratory, Pennsylvania State University, University Park PA 16802

²INAF, Osservatorio Astronomico di Palermo G. S. Vaiana, Piazza del Parlamento 1, I-90134 Palermo, Italy

$0.5 - 10 R_\star$. Second, no significant statistical differences in peak flare luminosity or temperature distributions are found among different morphological flare classes, suggesting a common underlying mechanism for all flares. Third, comparison with the general solar-scaling laws indicates that COUP flares may not fit adequately proposed power-temperature and duration-temperature solar-stellar fits. Fourth, COUP super-hot flares are found to be brighter but shorter than cooler COUP flares. Fifth, the majority of bright COUP flares can be viewed as enhanced analogs of the rare solar “long-duration events”.

Subject headings: open clusters and associations: individual (Orion Nebula Cluster) - stars: flare - stars: pre-main sequence - X-rays: stars

1. INTRODUCTION

All solar-type stars exhibit their highest levels of magnetic activity during their pre-main sequence (PMS) phase (Feigelson et al. 2007). This includes ‘superflares’ with peak luminosities $\log L_x \gtrsim 32 \text{ erg s}^{-1}$ in the $0.5 - 8 \text{ keV}$ band, 10^4 more powerful than the strongest flares seen in the contemporary Sun (e.g. Tsuboi et al. 1998; Grosso et al. 2004; Favata et al. 2005). PMS stars thus join RS CVn binary systems (e.g. Osten et al. 2007) as laboratories to study the physics of the most powerful magnetic reconnection events. PMS stars are more distant and fainter than the closer RS CVn systems, but hundreds of flaring PMS stars can be simultaneously studied due to their concentration in rich clusters.

The magnetic field structure of PMS stars, and thus the nature of their reconnection and flaring, may (or may not) qualitatively differ from other stars due to the presence of a protoplanetary disk during the early PMS stages. The intense high energy radiation from these PMS reconnection events may affect the physical and chemical properties of the surrounding circumstellar environment and play an important role in the formation of planets (Glassgold et al. 2005; Feigelson et al. 2007). A consensus has emerged during the past decade that PMS accretion is funneled by magnetic field lines linking the disk inner edge to the stellar surface (e.g. Hartmann 1998; Shu et al. 2000). However, while early theory assumed a dipolar field morphology, recent studies point to a complex multipolar field structure similar to the Sun’s (Jardine et al. 2006; Donati et al. 2007; Long et al. 2008).

It is also unclear whether the X-ray flares occur primarily in large loops with both footprints anchored on the stellar surface, or in loops linking the stellar photosphere with the inner rim of the circumstellar disk (Isobe et al. 2003; Favata et al. 2005). The first case may suffer instability due to centrifugal force (Jardine & Unruh 1999) while the second

case may load the loop with cool accreting material so that X-rays may not be produced (Preibisch et al. 2005).

The 13-day nearly continuous observation of ~ 1408 PMS stars in the Orion Nebula, the Chandra Orion Ultradeep Project (COUP; Getman et al. 2005a), enables both studies of individual flare properties and statistical studies of flaring from Orion stars (Wolk et al. 2005; Flaccomio et al. 2005; Stassun et al. 2006; Caramazza et al. 2007; Albacete Colombo et al. 2007). COUP also provided a unique opportunity to study relatively rare superflares and long-duration flares. Favata et al. (2005) have analyzed the strongest 32 flares in the COUP dataset using a long-standing method of time resolved spectroscopy (TRS) modeled as cooling plasma loops. They concluded that at least 1/3 of these are produced by magnetic reconnection in very long coronal $5 - 20 R_\star$ structures. Such structures were predicted in magnetosospheric accretion models (e.g Shu et al. 1997) but not clearly identified before COUP. Favata et al. (2005) recognized that their sample was too small to quantitatively probe the relationship between long coronal flaring structure and disks or accretion.

The aim of the current study is to extend the flare sample of Favata et al. (2005) utilizing a more sensitive technique of flare analysis, the “method of adaptively smoothed median energy” (MASME) introduced by Getman et al. (2006). We combine this method with the astrophysical cooling loop models of Reale et al. (1997) to trace the evolution of the flare plasma in temperature-density diagrams and derive flaring loop sizes. The method allowed us to examine 216 of the brightest flares from 161 brightest COUP PMS stars. These constitute the largest homogeneous sample of powerful stellar flares ever acquired in the X-ray band. In Getman et al. (2008) (Paper II), we use these results to study in detail the relationships between PMS X-ray flares, stellar properties, protoplanetary disks, and accretion.

Our flare analysis and the derived flare properties and classifications are presented in §2. Properties of the stars themselves are also provided. Global properties of our flares are considered in §3 and compared to published studies of older stars.

2. FLARE ANALYSIS

We analyze 216 of the brightest X-ray flares from 161 brightest COUP young stars. This is a > 5 -fold increase from the bright flare sample of Favata et al. (2005). The major steps of our analysis are presented below.

2.1. Flare Sample

Among 1616 COUP X-ray sources, 1408 have been associated with the stellar members of the Orion region (Getman et al. 2005b). With the exception of 10 hot OB-type stars, 1398 are identified as cool young members of the Orion region (Feigelson et al. 2005).

We start with the sub-sample consisting of the brightest 188 cool Orion stars, those with net counts $NC \geq 4000$ as tabulated by Getman et al. (2005a, Table 4). All of them show signs of variability, i.e. their X-ray lightcurves are characterized by at least two Bayesian Block segments (Table 7 of Getman et al.) during the 13.2-day COUP observation. The complete set of 1616 COUP lightcurves are available in the Source Atlas provided as a figure set in the electronic edition of Getman et al. Individual examples of strong flares are published in Favata et al. (2005) and Wolk et al. (2005).

Using the interactive software graphical program *function_1d* in the IDL-based TARA package¹, we identify flare-like events in which the peak count rate is ≥ 4 times that of the “characteristic” level. The characteristic level is the typical pre-flare or inter-flare; as explained by Wolk et al. (2005). We avoid the designation “quiescent” level because it probably arises from the integrated effect of many weaker flares. This results in 216 flares from 161 cool stars with median of ~ 1500 counts. Only 20 flares have < 600 counts.

2.2. MASME Spectral Modeling

Our analysis of flare spectral evolution is based on the method of adaptively smoothed median energy (MASME) introduced by Getman et al. (2006). We compare its results to the long-standing method of time-resolved spectroscopy (TRS), which involves statistical fitting of multiparameter spectral models, in Appendix A. The MASME method is simpler, statistically more stable, and computationally quicker than TRS. It employs an adaptively smoothed estimator of the median energy² of flare counts and count rate to infer the evolution of plasma temperatures and emission measures during the flare. This procedure is similar to the analyses of Reale & Micela (1998); Wargelin et al. (2007) which avoid nonlin-

¹Description and code for the “Tools for ACIS Review & Analysis” (TARA) package developed at Penn State can be found at <http://www.astro.psu.edu/xray/docs/TARA/>.

² X-ray source median energy is an observed quantity (Getman et al. 2005a) and can be effectively used as an indicator of plasma temperature if absorbing column is known, or indicator of column density at median energies > 1.7 keV (Feigelson et al. 2005). Other researches have also found that median energies are effective spectral estimators in X-ray CCD spectroscopy (Hong et al. 2004).

ear parametric flare modeling using hardness ratios.

The smoothing kernel is a rectangle (“boxcar”) of variable width; as it moves through the time series its width is adjusted so that it encompasses a specified number of X-ray counts. Kernels are evaluated on a time grid with bin width $\Delta t = 1.14$ ks, chosen to divide the total COUP observation span of 1140 ks into 1000 bins. Flux and median energy estimates are computed from the counts found in each of these overlapping kernels, forming smoothed flux and median energy time series which are then used for spectral modeling. Similar flux and median energy time series are produced by the ACIS Extract software package³. For each flare, the target number of counts in the kernel is chosen such that the resulting smoothed light curve closely matches the binned lightcurve given in the COUP Source Atlas of Getman et al. (2005a). This generally results in ~ 100 to ~ 600 counts included in each kernel for the weakest to the brightest flares, respectively. The typical width of the smoothing kernel is a few kiloseconds at the peak of the flare and ~ 10 ks at the base of the flare.

PMS X-ray spectra are typically modeled as emission by hot plasmas at one or two temperatures subject to absorption by a column density, N_H . If we adopt the N_H inferred from the time-integrated spectral fits of Getman et al. (2005a) and assume that N_H does not change during the COUP observation, then we can calibrate median energies and count rates to plasma temperatures (kT) and emission measures (EM). Figure 1 shows the median energy to plasma temperature calibration based on simulations similar to those described by Getman et al. (2006). For each COUP source, the *fakeit* command in XSPEC (Arnaud 1996) is used to simulate a grid of high signal-to-noise ACIS-I spectra with absorbed plasma models (WABS \times MEKAL) and fixed column density. Simulated spectra are then passed through ACIS Extract to perform photometric analysis, including calculation of fluxes (observed count rates) and median energy. At each time point of interest comparison of simulated count rates with that of the observed flare provides an estimate of flare emission measure; comparison of simulated and observed median energies provides an estimate of flare plasma temperature⁴. Due to the curved dependency of the true plasma temperature on observed median energy (Figure 1), estimated plasma temperatures of $\lesssim 200$ MK ($\lesssim 17$ keV) are expected to be quite reliable, while temperature values of $\gtrsim 200$ MK are much more uncertain. The accuracy of our temperature estimates is discussed in detail in Appendix B. We find the

³ACIS Extract is a *Chandra*-ACIS source extraction and analysis package developed at Penn State. It was used for the COUP data analysis and is described at http://www.astro.psu.edu/xray/docs/TARA/ae_users_guide.html.

⁴XSPEC fitting of simulated spectra using the χ^2 statistic tends to overestimate plasma temperature. In order to avoid this systematic bias in our simulations, we adopt the input plasma temperature rather than the temperature derived from XSPEC fit of the simulated spectrum.

1σ errors of peak flare temperature are generally $< 30\%$ for $T_{obs,pk} < 50$ MK, around 45% for $T_{obs,pk} \sim 200$ MK, but reach up to 65% for the hottest flares. Nonetheless, we establish that ‘superhot’ flares with derived peak temperatures above 200 MK are definitely hotter than 100 MK.

The major advantage of the MASME over TRS is that spectral analysis is performed at dozens of points along the decay phase of a flare light curve, rather than at just a handful of points typical of TRS. This higher time resolution often results in the discovery of a more detailed, often more complex flare behavior. A drawback of the MASME procedure is that the weak “characteristic” background is ignored. We discuss these issues further in Appendix A where the TRS and MASME analysis methods are carefully compared.

2.3. Loop modeling

One of the major goals of our flare analysis is to derive sizes of coronal structures responsible for the COUP flares. We employ the time-dependent hydrodynamic model of Reale et al. (1997) for a single coronal magnetic loop. Reale et al. establish a formula for estimating loop size taking accounting for the possibility of prolonged heating during the decay phase. They find

$$L = \frac{\tau_d \sqrt{T_{pk}}}{3.7 \times 10^{-4} F(\zeta)} \quad (1)$$

where L is the half-length of the loop (cm), τ_d is the flare decay e-folding timescale (sec), and T_{pk} is the flare maximum temperature at the loop apex (K). $F(\zeta)$ is a correction factor for prolonged heating that is a function of the slope ζ of the trajectory in the temperature-density diagram. In practice, $F(\zeta)$ and T_{pk} must be calibrated for each X-ray telescope and detector; the slope ζ is usually measured in the $\log T - \log(EM^{1/2})$ plane where EM is the changing emission measure and $EM^{1/2}$ is used as a proxy for the plasma density. We reproduce calibration formulas for $F(\zeta)$ and T_{pk} derived for *Chandra*-ACIS in Favata et al. (2005)

$$F(\zeta) = \frac{0.63}{\zeta - 0.32} + 1.41 \quad (2)$$

and

$$T_{pk} = 0.068 \times T_{obs}^{1.2} \quad (3)$$

where T_{pk} is a temperature at the loop apex (K), and T_{obs} is an “average” loop temperature (K) obtained from our *Chandra*-ACIS data.

This model is simplistic in a number of ways. It assumes the plasma has a uniform density with unity filling factor confined within a single semicircular loop of uniform cross-section

and 10:1 length:radius shape. Furthermore, the model assumes that this geometry remains unaltered during the flare, that energy is efficiently transported along magnetic field lines of the loop, and that there is continuous energy balance between the loop heating and the thermal conduction and radiative losses. Despite these limitations, the Reale et al. (1997) model has been applied successfully to a variety of solar and stellar flares (e.g. Crespo-Chacón et al. 2007; Testa et al. 2007; Franciosini et al. 2007; Giardino et al. 2007), including the COUP flares studied by Favata et al. (2005). It has the advantage over earlier and simpler cooling loop models (e.g. Rosner et al. 1978; Serio et al. 1991) which neglect reheating during the decay phase and thereby tend to overestimate loop sizes.

2.4. Flare Characteristics

Empirical and derived quantities obtained in our MASME flare analysis are reported in Tables 1 and 2. We explain them in this section and illustrate them in detail for one flare in Figure 2. The electronic edition of this paper contains a figure set similar to Figure 2 for our full sample (216 flares). Many sources show more than one bright flare during the 13-day COUP observation. In two sources (COUP #682 and 1463) we have analyzed four bright flares, ten sources have three flares; and forty three sources have two flares. The *FlareNo* quantity in conjunction with the *Source* number in Tables 1 and 2 provides a unique identifier for each of the 216 flares.

Several reported quantities are associated with the characteristic level between flares. Quantities t_{char1} and t_{char2} represent the start and stop times (offsets from the beginning of the COUP observation) of the “characteristic” lightcurve block with the lowest count rate. These intervals were defined visually using the interactive graphical tool *function_1d* in the *TARA* package; the duration of this block is always > 20 ks. The median count rate in this interval is CR_{char} . These quantities are labeled in blue in Figure 2a.

The flare events are defined by the quantities t_{flare1} and t_{flare2} (labeled in red in Figures 2a and b) giving start and stop times for the flare, with the peak count rate given by $CR_{flare,pk}$. Both CR_{char} and $CR_{flare,pk}$ are obtained from the binned histogram data (black points in Figures 2a and b), and not from the adaptively smoothed version of the lightcurve (dashed blue curve in Figure 2b). Following the recommendation of Reale et al. (1997), we choose the flare stop time as the moment at which the flare count rate has decreased to $\sim 1/10$ of the peak value. However, often an earlier t_{flare2} was chosen because a COUP observational gap or minor flare fell near the end of the studied flare.

Quantity Bgf represents the number of background counts expected in the flare time

interval, obtained by scaling the source’s background from Getman et al. (2005a) to the duration of the flare. With a few exceptions, this correction is very small ($Bgf/NCf < 0.02$). We therefore have chosen to ignore the background in estimating the median energy MEf during the flare.

Quantities τ_r , τ_{d1} , and τ_{d2} give $1/e$ rise time and decay times determined from a least-squares fit of the count rate histogram. This is illustrated by the red and green curves on Figure 2b. These are fits of the exponential function $CR = CR_{flare,pk} \times \exp[(t - t_{CR,pk})/\tau]$ where $t_{CR,pk}$ is the time of the peak count rate, and τ is $-\tau_{d1,2}$ or $+\tau_r$. Decays of many COUP flares deviate from a pure exponential shape. This is not unusual — Osten & Brown (1999) found that 8 of 33 flares from RS CVn binaries observed with the Extreme Ultraviolet Explorer showed changing exponential decays. Complex, often bumpy, decays arise from both reheating of a single loop and the illumination of associated loops. These issues are discussed in the next section. For COUP X-ray flares, we introduce two decay e-folding timescales, τ_{d1} for the initial purely exponential decay phase lasting at least to the time point t_{exp} , and τ_{d2} for the e-folding decay timescale averaged over the entire decay phase from $t_{CR,pk}$ until t_{flare2} . As the data become less consistent with a single exponential decay model, the difference between τ_{d1} and τ_{d2} increases.

The adaptively smoothed count rate and median energy time series are shown as the blue dashed curve in Figure 2b and the black symbols in Figure 2c. These are converted into plasma temperature (Figure 2d) and flare emission measure (Figure 2e) time series using calibration simulations described in §2.2. Information on maximum values of flare X-ray luminosity ($\log L_{X,pk}$), observed temperature ($T_{obs,pk}$), emission measure (EM_{pk}), and corresponding time points, such as $t_{T,pk}$ and $t_{EM,pk}$ is then easily obtained.

Considering that the proper decay phase begins at the time of the density peak, not count rate or temperature peak (at least for an impulsive flare event), Reale (2007) encourages using the temperature at the density peak rather than the brightness peak when determine the loop length. We thus introduce the quantity $T_{EM,pk}$, the plasma temperature at the peak of the emission measure. Cross symbols in Figure 2c-f mark the rise phase, the time period prior to the moment when emission measure reaches its maximum value, whereas circle symbols mark the decay phase of the flare.

Several remaining obtained quantities listed in Tables 1 and 2 and shown in Figure 2 remain to be discussed. Quantity t_{sep} is the time point separating the two distinct decay phases when a simple exponential decay is not present. Quantities ζ_1 , ζ_2 , and ζ_3 are the inferred slopes of the trajectory in the $\log T - \log(EM^{1/2})$ diagram. The morphological flare type is discussed in §2.5. Quantities L_1 , L_2 , and L_{lim} are the lengths of the flaring structures inferred from equation (1). Flag₁ provides details on a number of decay phases and indicates

the “dominant” slope used in estimation of loop sizes.

2.5. Flare Morphology and Classification

In order to obtain optimal results within the framework of the Reale et al. (1997) single loop model, the X-ray lightcurve should not present significant deviations from a pure exponential decay, and the decay trajectory in the $\log T - \log(EM^{1/2})$ plane should be linear. Strong deviations from an exponential decay and the absence of a single linear trajectory are indications of more complex events such as multiple coronal loops (e.g. sequential reconnection in a loop arcade as in a 2-ribbon solar flare) and/or complex heating sequences within a single loop (e.g. Reale et al. 2004; Reale 2007).

However, even in the case of complex flares it is appropriate to apply the single loop approach to a lightcurve segment if there is an indication for the presence of a single dominant loop. Reale (2007) argues that when multiple loop structures are involved in the flare, the rise and early decay are often dominated by a single primary loop. This is supported by detailed time-dependent loop modeling of the “bumpy” decay flare observed with XMM-Newton on Proxima Centauri (Reale et al. 2004). Here it was found that the X-ray emission from the primary single loop dominated the initial phases of the flare, but later was overlapped by the emission from an arcade of several loops of similar size as the primary loop.

Similar complex, multiple-component flares have been seen in the contemporary Sun, including the well-studied Bastille Day flare in July 2000 (Aschwanden & Alexander 2001) and a variety of bumpy flares seen with the GOES and TRACE satellites. They are seen in both 2-ribbon flares and compact flares⁵. Reale et al. (2004) speculate that this is a common pattern in large solar and stellar magnetic reconnection.

We have adapted these ideas, together with our careful examination of the X-ray morphology of the 216 COUP flares, into a classification scheme consisting of four well-defined groups and two groups to gather flares which cannot be clearly characterized. In order of their morphological complexity, these classes are:

Typical flares (typ) These have simple X-ray lightcurves with rapid monotonic rise and generally slower monotonic decay. This is the most populous class with 84 of the 216

⁵Examples of “bumpy” solar flares seen in soft X-rays by GOES 8, and EUV light by TRACE, can be found in the TRACE Flare Catalog (http://hea-www.harvard.edu/trace/flare_catalog/index.html). See, for example, the 16 Jan 05 (22:03:00UT, M2.4) and 08 Sep 05 (20:29:00UT, M2.1) 2-ribbon flares and the 14 Nov 05 (22:00:00UT, M1.0) and 02 Dec 05 (10:12:00UT, M7.8) compact flares.

COUP flares. Seven of them have symmetrical lightcurve shape with similar rise and decay timescales.

Step flares (stp) These look like a typical flare but with a shoulder or bump overlayed on its decay phase. These morphologies are commonly seen on the Sun and are due either to a reheating event or to a triggered reconnection in a nearby magnetic loop. Thirty-eight COUP flares fall into this category. The “bumpy” decay flare from Proxima Centauri (Reale et al. 2004) is a good example of this class.

Double flares (dbl) Double flares look like two overlapped typical flares, or a typical flare with a bump on its rise phase. Eight flares clearly show double peaks in appearance.

Slow rise, top flat flares (srtf=srf) These are more complex events where variations appear to occur more slowly than in most flares. They have slow rises, long duration peaks, and/or very long decays. One of these (a T-Tauri star in the Orion B cloud) was discussed by Grosso et al. (2004) without a clear interpretation, and a few (COUP #43, 597, 1384) appear in Favata et al. (2005, see their Figure 9). In our study, twenty COUP flares are in this class.

Incomplete (inc) These are 42 flares with their *Chandra* lightcurves severely interrupted by the COUP observational gaps.

Others (oth) These are 24 flares with poorly defined shapes generally due to their low statistics.

The four well-defined classes are illustrated in Figures 3-6 along with their inferred trajectories on the $\log T - \log(EM^{1/2})$ plane. For about 56% (34%) out of 84 (38) typical (step) flares, trajectories can be approximated by a single slope. In these cases, the derived loop sizes are most reliable. In many of the remaining cases, two slopes can be discerned in the $\log T - \log(EM^{1/2})$ trajectories, while in some the patterns are too complex to interpret. Flare classifications based on lightcurve morphology may not be correct in all cases; for example, a few flares with simple lightcurve decays classified as typical flares show double-peaked temperature evolutions. These effects are included in the loop reheating model (§2.3) and thus the derived loop sizes, but such flares have not been reclassified as double-peaked flares.

Flag₁ in Table 2 encodes the number of inferred dominant decay slopes of $\log T - \log(EM^{1/2})$ trajectories; values of 01 ($= \zeta_1$), 02 ($= \zeta_2$) and 03 ($= \zeta_3$) refer to a single dominant slope, while 12 ($= \zeta_1, \zeta_2$), 13 ($= \zeta_1, \zeta_3$) and 23 ($= \zeta_2, \zeta_3$) refer to a double slope. In cases with a single slope, the slope value used is generally the average slope ζ_1 (green solid

line in Figure 2f) derived within the the whole flare time interval. In double slope cases, the two slopes are generally described by ζ_2 (slope within the initial decay; red dotted line in Figure 2f) and ζ_3 (slope within the late decay; orange dashed line in Figure 2f) separated in time by the point t_{sep} (given in Table 1).

While we do not know of a similar flare classification effort in other solar or stellar studies, a similar range of flare behaviors is seen in the contemporary Sun. Analysis of Solar Maximum Mission observations of 66 solar flares by Sylwester et al. (1993) showed 26% of flares have $\log T - \log(EM^{1/2})$ trajectories with two or more branches while the majority show single-branched trajectories.

2.6. Flare Loop Sizes

Due to the complexity of flare behavior in our sample (described above, shown in Figure 2 and in the electronic atlas), it seems reasonable to present a range of possible loop sizes rather than a single size value for a given flare. The range of sizes is derived with the assumption for the presence of dominant coronal structures even during the complex flare events. This approach should be suitable for the goals of the current work, which is oriented towards examination of statistical relationships between flare behaviors, magnetic loop sizes, global star properties, protoplanetary disks and accretion.

The loop size range ($[L_1 : L_2]$, reported in Table 2) is estimated through equations (1)–(3) in §2.3 using the combination of both decay timescales (initial, τ_{d1} , and averaged over the entire decay phase, τ_{d2}) with the decay slopes indicated by Flag₁. If a single dominant slope is indicated by Flag₁, then two loop size estimates emerge after applying both decay timescales with the combination of that single slope. If a double slope is indicated by Flag₁, then two loop size estimates emerge in the following ways: for Flag₁ = 23, we combine τ_{d1} with ζ_2 and τ_{d2} with ζ_3 ; for Flag₁ = 13, we combine τ_{d1} with ζ_1 and τ_{d2} with ζ_3 ; and for Flag₁ = 12, we combine τ_{d1} with ζ_2 and τ_{d2} with ζ_1 . T_{obs} in formula (3) is the observed *Chandra*-ACIS flare temperature at the peak of the emission measure ($T_{EM,pk}$ from Table 2).

L_{lim} , the limiting maximum loop length assuming a freely decaying loop with no sustained heating, is computed using τ_{d2} in equation (14) of Serio et al. (1991). This estimate is based on the older cooling loop theory of Rosner et al. (1978) and may over-estimate loop lengths if reheating or triggered events extend the decay phase.

We compared our methodology with the well-studied case of the August 2001 flare on the dMe star Proxima Centauri observed with XMM-Newton (Reale et al. 2004). This flare has a “bumpy” decay similar to our “step” (stp) flares. Using our procedures, we obtain

$\zeta_1 = 0.6$, $\zeta_2 = 0.7$, $\zeta_3 = 0.4$, $\tau_{d1} = 1.7$ ks, $\tau_{d2} = 3.3$ ks, $t_{sep} = 4.7$ ks, $\text{Flag}_1 = 01$. The inferred loop size range is $L_1 = 5 \times 10^9$ cm and $L_2 = 1 \times 10^{10}$ cm. Reale et al. (2004) obtained a value of 1×10^{10} from a detailed time-dependent hydrodynamic model of the flare evolution. We conclude that our procedures are consistent with other analyses of similar complicated flares.

2.7. Collected Source Properties

Properties of the 161 COUP stars hosting our flare sample are presented in Table 4. These stellar properties will be extensively used in Paper II. Many of the quantities have been taken from the COUP tables of Getman et al. (2005a) including: time-integrated net counts, background counts, median energy, column density. JHK_s magnitudes obtained from the merged 2MASS-VLT catalog with a flag indicating quality of the 2MASS photometry. Optical data include the 8542 Å Ca II line strength as an accretion indicator, and stellar mass and radius estimated from position in the Hertzsprung-Russell diagram. See Getman et al. for full details and references for these quantities. Stellar rotational periods are taken from the extended rotational data collection of Flaccomio et al. (2005). For stars with known masses (M) and rotational periods (P) we calculate the Keplerian corotation radius where centrifugal force balances gravity from $R_{cor} = (G \times M \times P^2 / 4 \times \pi^2)^{1/3}$.

The near-infrared (NIR) color excess $\Delta(H - K_s)$, an indicator of dusty inner circumstellar disks, is calculated here as an excess from the rightmost reddening vector on the $J - H$ vs. $H - K_s$ color-color diagram originating at $\sim 0.1 M_\odot$ assuming an age of 1 Myr and using PMS models of Siess et al. (2000). $\Delta(H - K_s)$ is given only for sources with reliable 2MASS photometry (Fl = AAA000).

A more sensitive measure of disk dust is derived from mid-infrared (MIR) images of the Orion region in the 3.6 and 4.5 μm IRAC bands using the *Spitzer* archived data (*Spitzer* observing program #50; G. Fazio, PI). For each band, the 3×4 shallow maps, each with 24 dither pointings, processed by the Spitzer Science Center pipeline (ver. S14.0.0) were combined into one mosaic with pixel size $0.86''$ using IDL software developed by R. Gutermuth of the IRAC instrumental team. Aperture photometry was performed with the routine *aper.pro* in the IDLPHOT package⁶ for isolated COUP sources using an aperture radius of 4 pixels with a 4–8 pixel annulus for sky subtraction. For these aperture and sky regions, we adopted zero-point magnitude values of 19.490 and 18.751 mag, for the 3.6 and 4.5 μm bands, respectively (K. Luhman, private communication). High signal-to-noise photometric results

⁶IDLPHOT is available at <http://idlastro.gsfc.nasa.gov/ftp/pro/idlphot/aaareadme.txt>.

in both bands are presented for 112 stars in Table 4. The majority of stars without MIR photometry are those located in the outer regions of the Orion Nebula where [3.6] and [4.5] images do not overlap. For several sources located near the BN/KL region, MIR photometry is unreliable due to strong nebular contamination in infrared images, and is omitted.

3. RESULTS

3.1. Global flare properties

Figure 7 summarizes some of the inferred physical properties of the COUP flares in the form of univariate cumulative distributions differentiated by the flare morphological classes defined in §2.5. The panels plot distributions of several quantities relating to flare rise and decay timescales, peak luminosities, and peak temperatures.

Panel *a* of Figure 7 shows that 90% of these powerful COUP flares have rise times between 1 hour and 1 day (3 – 100 ks). “Typical” (typ) and “step” (stp) flares have similar rise times with medians around ~ 3 hours (10 ks). In contrast, as expected from their class definition, “slow-rise-top-flat” (srtf) flares have much longer rise timescales with median around 12 hours (44 ks)⁷. It is unclear whether this slow rise is due to multiple heating events of a single magnetic loop, or a sequence of triggered reconnection events in a loop arcade. In contrast to all of these PMS flares, a rise time of the soft X-ray emission in a typical solar flare is typically only a few minutes (e.g. Priest & Forbes 2002) because solar chromospheric material fills the smaller solar flare volumes more quickly. Franciosini et al. (2007) provide statistics on rise and decay times for Taurus flares from the XEST study.

Panel *b* shows that the decay e-folding timescales derived over the whole flare interval, (τ_{d2}), ranging from 3 hours to 1.5 days (10 ks to 150 ks) for 90% of the COUP flares. The median of $\tau_{d2} \sim 6$ hours (22 ks) for “typical” flares is much shorter than that of all other morphological flare classes which have median decay times around 12 hours (~ 45 ks). The τ_{d1} decay timescales derived over the initial exponential decay phase [$t_{CR,pk} - t_{exp}$] are on average a factor of 1.2 shorter than τ_{d2} , again with decays systematically shorter in “typical” flares than other classes (panels *c* and *e*). The decay timescales in typical solar flares are

⁷We caution that our procedure for estimating the e-folding rise timescales for COUP “srtf” flares, in which the rise phase is defined as the time interval between the flare start and the time point with a maximum observed count rate, may give longer timescales than those derived in other works. For example, Grosso et al. (2004) report $\tau_{rise} \sim 2$ hours (7.2 ks) for the slow-rise flare in LkH α 312 by restricting the rise to the period of very rapid count rate change. For this flare, our procedure would give $\tau_{rise} \sim 5$ hours (~ 20 ks).

even shorter or comparable with this, and are of 10 min to a few hours (e.g. Reale et al. 1997; Priest & Forbes 2002). The ratios of rise and decay timescales serve as good quantitative discriminators between major different morphological flare classes. The median ratio τ_{d2}/τ_{raise} is 1.2, 2.6, and 4.3 ks for “srtf”, “typical”, and “step” flares, respectively (panel *d*). The median of τ_{d2}/τ_{d1} for “step” flares of 1.7 is much higher than the values of 1.1-1.2 for the “typical”, “srtf” and other classes (panel *e*).

Panel *f* of Figure 7 indicates that peak flare X-ray luminosities in the [0.5 – 8.0] keV band for our flare sample span $\log L_{x,pk} \simeq 30.6$ to 32.3 erg s $^{-1}$ (90% range) with 10% of flares reaching luminosities $\log L_{x,pk} \gtrsim 32$ erg/s. The strongest flare, flare #1 from COUP #1462, has peak luminosity of 32.9 erg s $^{-1}$; it is also one of the hottest flares ($T_{obs,pk} \gg 200$ MK). While the lower end of this distribution has no scientific importance due to our selection criteria, it is relevant that no significant luminosity differences are seen between different flare morphological classes, except for a possible indication that “srtf” flares do not achieve the highest peak luminosities. Similarly, no statistical differences in temperature distributions are seen (panel *g*). Temperatures span 20 to ~ 500 MK (90% range) with median around 63 MK. Recall that individual values of temperatures above ~ 200 MK are quite uncertain (Figures 1 and 14b).

These results thus characterize the global properties of PMS flares with peak X-ray luminosities between 31 and 33 erg s $^{-1}$. The temperatures and luminosities of the brightest COUP flares are similar to the most luminous X-ray flares ever recorded in young stellar objects: V773 Tau in the Taurus clouds with $L_{pk} \gtrsim 10^{33}$ erg s $^{-1}$ and $T_{pk} \gtrsim 100$ MK (Tsuboi et al. 1998), YLW 16A in the ρ Ophiuchi Cloud with $L_{pk} \sim 2 \times 10^{32}$ erg s $^{-1}$ and $T_{pk} \sim 140$ MK (Imanishi et al. 2001), LkH α 312 in the M 78 reflection nebula of Orion with $L_{pk} \simeq 10^{32}$ erg s $^{-1}$ and $T_{pk} \simeq 90$ MK (Grosso et al. 2004), and star #294 in the Cep OB3b region with $L_{pk} \simeq 2 \times 10^{32}$ erg s $^{-1}$ and $T_{pk} \gg 100$ MK (Getman et al. 2006). Recall that even the most powerful solar flares today rarely exceed 28.5 erg s $^{-1}$ in the Chandra band.

While the differences between rise and decay timescales between our morphological classes mostly reflect our class definitions, the similarities in $L_{X,pk}$ and $T_{obs,pk}$ distributions among classes (Figure 7f and g) are real results. They demonstrate that differences in flare morphology – particularly the difference between typical flares with fast-rises and exponential-decays and atypical flares with slow-rises and flat-tops – are not reflected in large differences in luminosity or temperature. This suggests that all types of flare morphologies arise from similar magnetic reconnection mechanisms.

3.2. Comparison with flares on older stars

3.2.1. Comparison with general solar-stellar scaling law

From their compilation and comparison of comprehensive data sets of solar and stellar⁸ flares, Aschwanden et al. (2008) find a common scaling law between peak flare emission measure (EM_{pk}) and peak flare plasma temperature ($T_{obs,pk}$), $EM_{pk} \propto T_{obs,pk}^{4.7}$, but with stellar emission measures ~ 250 times higher than that of solar flares. They also find that solar and stellar flare durations, τ_f , follow the trend $\tau_f \propto T_{obs,pk}^{0.9}$. For flare loop lengths, L , they find the trend $L \propto T_{obs,pk}^{0.9}$ for solar flares only. Here we relate our 216 COUP flares to these scaling laws of solar-stellar flares.

Figure 8 compares the EM_{pk} – $T_{obs,pk}$ relation between COUP flares (black circles), stellar flares of Güdel (2004) (grey boxes), and solar-stellar trends obtained by Aschwanden et al. (2008) (dashed and dotted lines). The COUP flares represent the most luminous flare events ever detected from stellar objects, occupying the highest range in stellar emission measures, $53.5 < \log(EM_{pk}) < 56 \text{ cm}^{-3}$. The lower boundary corresponds to our selection cut of $NC > 4000$ source counts (§2.1).

In agreement with the scaling-law of Aschwanden et al. (2008), about 60% of the COUP flares are located within the 67% range of flares from older stars (dashed lines). But the remaining stars do not follow the scaling-law of Aschwanden et al. (2008): 34% (73 out of 216) of the COUP flares with unexpected super-hot plasma temperatures of $T_{obs,pk} \gtrsim 100 \text{ MK}$ strongly deviate from the expected $EM_{pk} \propto T_{obs,pk}^{4.7}$ trend. These deviations may not be restricted to COUP flares; a careful examination of the stellar flare sample of Güdel (2004) shows that 10 out of their 11 flares (grey boxes) with $T_{obs,pk} \gtrsim 100 \text{ MK}$ are located below the regression line of Aschwanden et al. (2008), in agreement with the COUP super-hot flares. Considered by themselves, the COUP flares follow a much shallower scaling law, $EM_{pk} \propto T_{obs,pk}^{0.4}$. The statistical significance of this shallow correlation is strong: COUP flares with $T_{obs,pk} < 100 \text{ MK}$ have median $\log(EM_{pk}) = 54.09 \text{ cm}^{-3}$ while super-hot flares with $T_{obs,pk} \gtrsim 100 \text{ MK}$ with median $\log(EM_{pk}) = 54.45 \text{ cm}^{-3}$ with two-sample probability of similar EM distributions $P_{KS} << 10^{-4}$.

Figure 9 compares flare duration τ_f to peak plasma temperature $T_{obs,pk}$ for our COUP flares (black circles), stellar flares compiled by Güdel (2004) (grey boxes) and the regression fits for solar-stellar flares obtained by Aschwanden et al. (2008) (dotted lines). Here we use our longest decay timescale τ_{d2} to correspond with their flare durations τ_f . Flare durations

⁸Stellar flare parameters for PMS and older active stars were taken from the compilation of Güdel (2004).

for solar LDEs (long decay events, see §3.2.2) are $\tau_f = (t_{end} - t_{start})$ on their GOES lightcurves which are, on average, 3 times longer than their e-folding decay timescales.

First, we note that the remarkably long duration (13 days) of the COUP observation provided a unique opportunity to capture stellar flares with decay timescales longer than a day. As in the $EM_{pk} - T_{obs,pk}$ plot, the COUP flares do not exhibit the reported solar-stellar relationship, $\tau_f \propto T_{obs,pk}^{0.9}$. While some COUP flares studied here are consistent with the relation, the majority deviate strongly with peak plasma temperatures either too cool or too hot. For COUP flares, we find a weak trend in the other direction, $\tau_{d2} \propto T_{obs,pk}^{-0.2}$. Similar results are obtained using our flare rise timescale τ_r and initial flare decay timescale τ_{d1} , and the trends are confirmed with Kolmogorov-Smirnov tests⁹. The median duration for flares with $T_{obs,pk} < 100$ MK is $\tau_{d2} = 45$ ks compared to 25 ks for super-hot flares with $T_{obs,pk} \gtrsim 100$ MK. However, we do not analyze here many hundreds of weaker and shorter COUP flares that could potentially compensate some of these deviations.

Although stellar and COUP flare loop lengths are derived from cooling models rather than directly from the observations, it is useful to compare COUP, stellar, and solar length distributions. Figure 10a shows the COUP flares (black circles), stellar flares (grey boxes), and locus of solar flares (dotted lines) in the $L-T_{obs,pk}$ diagram. For COUP flares, L is the mean value of the inferred $[L_1 - L_2]$ range. COUP loop sizes range from $< 10^{11}$ cm to $\gtrsim 10^{12}$ cm, a range of very large loops previously occupied by only dozen stellar flares. These loop sizes are $10^2 - 10^3$ larger than seen in solar flares. Figure 10b shows that the variables L and L/R_* are roughly equivalent; COUP flare loop lengths range from ~ 0.2 to $\gtrsim 10$ stellar radii. COUP loop lengths slowly increase with peak flare temperature roughly as $L \propto T_{obs,pk}^{(0.4-0.5)}$, consistent with the slope seen in solar flares but offset to much larger lengths at a given temperature. This trend, however, emerges from the assumptions underlying our loop modeling (§2.3, equations (1) and (3)) and thus may not be physically significant.

We thus find that flares in our COUP sample are indeed among the most luminous, hottest, largest (in term of loop length) and long-lived of any X-ray flares known. Comparison with the stellar-solar scaling laws of Aschwanden et al. (2008) provides non-trivial results. One-third of the COUP sample have super-hot temperatures of $T_{obs,pk} > 100$ MK. These do not fit the strong $EM_{pk} \propto T_{obs,pk}^{4.7}$ solar-stellar scaling law; rather, in the COUP regime, temperatures can increase several fold above 100 MK with only slight increase in plasma emission measures. This may be related to the low efficiency of filling up very large coronal

⁹KS results indicate significant differences between distributions of τ_r ($P_{KS} = 0.004$) with median values of $\tau_r = 15.8$ ks and $\tau_r = 9.7$ ks for $T_{obs,pk} < 100$ MK and $T_{obs,pk} \gtrsim 100$ MK flares, respectively; and τ_{d1} ($P_{KS} = 0.001$) with median values of $\tau_{d1} = 30.1$ ks and $\tau_{d1} = 21.5$ ks for $T_{obs,pk} < 100$ MK and $T_{obs,pk} \gtrsim 100$ MK flares, respectively.

loops of PMS stars with hot plasma from chromospheric evaporation. COUP flares also do not follow the solar-stellar correlation between flare duration and peak plasma temperature; indeed, we find a slight anti-trend where hotter COUP flares are on average slightly shorter in duration than cooler flares. However, a previously reported correlation between flare loop length and peak plasma temperature is present, though offset to longer loops than seen in solar and older stellar flares. Further analysis of COUP super-hot flares is presented in Paper II.

Some form of saturation of previously reported relationships is clearly present. Unlike solar flares which arise in small-scale multi-polar fields, COUP flaring magnetic structures are typically larger than the radii of their host stars. We turn now to possible relationships with a rare class of long duration solar flares which are also believed to be associated with large scale coronal structures.

3.2.2. Solar long decay flare events

Giant X-ray arches and streamers with altitudes reaching up to several hundred thousand kilometers produced during some solar flares have been observed by the *Skylab*, SMM and *Yohkoh* space observatories (Hiei 1994; Švestka et al. 1995; Farnik et al. 1996; Švestka et al. 1997; Hiei 1997, and references therein). Such events were originally called long decay events (LDEs, Kahler 1977). Corresponding X-ray lightcurves of solar LDEs often exhibit flares lasting from a few hours to a day, similar to flare durations in our sample. Figure 11 exemplifies the GOES lightcurves of long solar flares associated with giant X-ray arches. The origin of solar X-ray giant arches and streamers is not well understood. A popular model explains that the powerful prominence eruption or coronal mass ejection, often (but not always) associated with an impulsive flare (Priest & Forbes 2002), expands into an overlying large-scale magnetic field with the subsequent reconnection of magnetic lines through a vertical current sheet and formation of a system of giant closed loops in a shape of arches and streamers (Sturrock 1966; Kopp & Pneuman 1976; Forbes & Acton 1996).

Flare parameters for a number of solar LDEs are shown in Figures 8-10 (grey diamonds)¹⁰. Peak emission measures of solar LDEs vary from $\log(EM_{pk}) \sim 44 \text{ cm}^{-3}$ for X-ray

¹⁰Flare parameters are presented for the following solar LDEs: giant arches observed on 2 Nov 1991, 4 Nov 1991, 21 Feb 1992, and 15 Mar 1993; X-ray streamers seen on 24 Jan 1992 and 28 Oct 1992. Peak flare emission measures, plasma temperatures, and maximum altitudes are taken from Švestka et al. (1995); Švestka et al. (1997); Getman & Livshits (2000). Flare durations are $\tau_f = (t_{end} - t_{start})$ in their GOES lightcurves.

streamers to $\log(EM_{pk}) \sim 50$ cm $^{-3}$ for giant arches, with flare durations $\tau_f > 10$ ks and altitudes of $L \gtrsim 1 \times 10^{11}$ cm. Both durations and altitudes are well above loci of typical solar flares. In addition, several solar flare limb events observed on *Skylab* with inferred durations of > 12000 seconds, temperatures of $> 7 - 8$ MK, and altitudes of $> 3 - 4 \times 10^{10}$ cm, which are called Class II events (Pallavicini et al. 1977), are also located far the usual solar flare locus (see diamond symbols in Figure 4 of Aschwanden et al. 2008). These may represent a sub-class of solar LDEs.

With their extremely long flare durations, often hot temperatures, and associated large-scale flaring structures, LDEs are thus outliers from the solar flare scaling laws, similar in many respects to the COUP flares analyzed here. It is reasonable to propose that the majority of the flares in our COUP flare sample are enhanced analogs of these solar LDEs. Concerns regarding possible effects of centrifugal forces and magnetic field confinement on the COUP PMS flares are discussed in Paper II.

4. CONCLUSIONS

We analyze 216 bright X-ray flares from the Chandra Orion Ultradeep Project which provides the longest nearly-continuous observation of a rich PMS stellar cluster in the X-ray band. Our effort is based on a new spectral analysis technique (MASME) that avoids nonlinear parametric modeling and is more sensitive than standard methods. Flare loop parameters are derived from the well-established flare plasma model of Reale et al. (1997).

We thus emerge with the largest dataset of PMS flares, or indeed stellar flares at any stellar age, with peak luminosities in the range $31 < \log L_{X,pk} < 33$ erg s $^{-1}$, several orders of magnitude more powerful than any solar flare. For each flare we provide a catalog of > 30 derived flare properties including inferred sizes of associated coronal loops and flare morphological classes. We give an electronic atlas with flare lightcurves, temporal evolution plots of X-ray median energy, plasma temperature, emission measure, and derived temperature density diagram. This collection of empirical and model-dependent information can serve as a valuable testbed for stellar flare models.

The powerful COUP flares studied here have rise timescales ranging from 1 hour to 1 day and decay timescales ranging from a few hours to 1.5 days. An important empirical result is that peak plasma temperatures are often 100 MK, in some cases > 200 MK. These temperatures are derived from a robust calibration of median energies; traditional time-resolve spectroscopy often does not have the time resolution to detect this brief super-hot phase. No significant differences in peak flare luminosity or temperature distributions are

found among the wide range of morphological flare classes: typical fast-rise exponential-decays, step decays, double peaks, and slow-rise flat-top. This suggests that all flare types arise from similar underlying magnetic reconnection mechanisms and geometries.

Comparison of the COUP flare properties with the general solar-stellar scaling laws of Aschwanden et al. (2008) presents surprising results. Our flares do not follow the solar-stellar trend between plasma peak emission measure and temperature, $EM_{pk} \propto T_{obs,pk}^{4.7}$. The trend between flare duration and peak temperature is also absent. Super-hot COUP flares are found to be brighter but shorter in duration than cooler COUP flares. This is further developed in Paper II.

Compared to non-PMS systems, the inferred sizes of COUP flaring structures are remarkably large, ranging widely from $L = 0.5$ to $10 R_*$. These large flaring structures must be associated with large-scale stellar magnetic fields. Rare long decay solar events associated with the largest known X-ray emitting structures are possible solar analogs to these COUP flares.

Our flare sample provides a valuable laboratory for the study of the physics and astronomy of magnetic reconnection events. This study (Paper I) examines flare morphologies, and provides general comparison of COUP flare characteristics with those of other active X-ray stars and the Sun. Paper II concentrates on relationships between flare behavior, protoplanetary disks (both passive and accreting), and other stellar properties including rotational periods and Keplerian corotation radii. Paper II further investigates super-hot COUP flares and magnetic field strength on Orion T-Tauri stars.

KG thanks Moisey Livshits for introducing him to the physics of solar long decay events. We thank Vinay Kashyap, Rachel Osten, and Paola Testa for the stimulating discussions, and Kevin Luhman for assistance with *Spitzer*-IRAC data analysis. We also thank the referee, Jeffery Linsky, for his time and many useful comments that improved this work. This work was supported by the *Chandra* ACIS Team (G. Garmire, PI) through the SAO grant SV4-74018. G.M. acknowledges contribution from contract ASI-INAF I/088/06/0. This publication makes use of data products from the Two Micron All Sky Survey (a joint project of the University of Massachusetts and the Infrared Processing and Analysis Center/California Institute of Technology, funded by NASA and NSF), and archival data obtained with the *Spitzer Space Telescope* (operated by the Jet Propulsion Laboratory, California Institute of Technology under a contract with NASA).

A. COMPARISON OF MASME WITH TIME-RESOLVED SPECTROSCOPY

Studies of stellar flare evolution have been conducted for some years using low-spectral resolution time series characteristic of CCD detectors on the ASCA, Chandra, XMM-Newton, and Suzaku satellites. Most of these studies have used a method we call Time Resolved Spectroscopy (TRS) where the lightcurve is divided into intervals (e.g. flare rise, flare peak, and several flare decay intervals) and full multiparameter fits to the spectra are made in each interval. These fits are typically made with a code such as XSPEC (used here and throughout the COUP effort), Sherpa, or MIDAS with the assumption of a one- or two-temperature plasma subject to absorption. In cases of very high signal, non-solar elemental abundances may also be added as free parameters. Examples of such analyses applied to powerful PMS stellar flares include the reheated flare of the weak-lined T Tauri star V773 Tau in the Taurus clouds seen with ASCA (Tsuboi et al. 1998), the complex flare of the protostar YLW 16A in the Ophiuchi cloud seen with Chandra (Imanishi et al. 2001), the slow-rise flare of the weak/classical T Tauri star LkH α 312 in the Orion B cloud seen with Chandra (Grosso et al. 2004), the strong flare in the Herbig Ae star V892 Tau in Taurus clouds seen with XMM-Newton (Giardino et al. 2004), 18 more brightest flare-like events from T Tauri stars in Taurus clouds analyzed in the XEST project (Franciosini et al. 2007), and the study of 32 powerful Orion Nebula Cluster flares in Orion A based on COUP data (Favata et al. 2005).

The main difference between our MASME method and the TRS method is that we obtain the temperature and emission measure evolutions on rapid timescales directly from the smoothed median energy and count rate evolutions without using a fitting procedure for analyzed data (§2.2). The calibration curves shown in Figure 1 are crucial for converting median energies to plasma temperatures. This permits estimation of temperature and emission measure (luminosity) at many more time points using fewer counts at each time step than possible with TRS. No fitting based on least-squares or maximum likelihood statistical procedures is made. Drawbacks to MASME include the omission of characteristic level emission and the inability to track possible N_H variations; note that these capabilities of TRS are also neglected in many previous studies.

To compare the two methods, we have conducted a TRS analysis of the 216 COUP flares as follows. We examine the consistency of the two procedures, and examine the effects of neglecting the characteristic emission. The peak plus decay interval of each flare is divided into a number of segments (SegNum), each hosting a roughly constant number of X-ray flare counts ($< N >_{\text{seg}}$). For the majority of flares ($\sim 54\%$), we defined ≥ 5 segments with ~ 200 counts each. For weaker flares ($\sim 28\%$), we defined $\gtrsim 3$ segments with 100 to 200 counts

each. For the brightest flares (18%), we defined $\gtrsim 10$ segments with $\gtrsim 300$ counts each.

Table 3 presents the results of the TRS analysis including information on lightcurve segmentation, “characteristic” background spectrum, inferred flare peak temperatures, and temperature-density slopes. Several “typical” flares with simple single-decay slopes are presented in Figures 12-13. Results are provided for cases with (“CH”) and without (“noCH”) accounting for the characteristic non-flare emission. The spectrum of each segment is fitted with the WABS \times MEKAL model (compatible with previous COUP spectroscopic fits; Getman et al. 2005a) plus a similar model of the characteristic component in the “CH” cases. The absorption N_H is frozen to the value obtained from the global fits of Getman et al. (2005a), and 0.3 times solar elemental abundances are assumed. The characteristic spectrum was obtained from the $[t_{\text{char}1} - t_{\text{char}2}]$ segment which is the > 20 ks lightcurve block with the least median value of the count rate. There is, of course, no guarantee that the characteristic emission is the same during the flare interval.

Figure 14 compares several outcomes of the MASME technique with those of TRS. Panel (a) shows that the inferred TRS slopes of the trajectories in the $\log(T) - \log(EM^{1/2})$ diagram which omit the characteristic emission ($\zeta_{\text{TRS,noCH}}$) are systematically steeper by $\simeq 20\%$ to $\simeq 15\%$ with increasing number of TRS segments than those which account for characteristic emission ($\zeta_{\text{TRS,CH}}$, see open boxes and the dashed regression line in panel a). This arises because the flare spectrum is generally harder than the characteristic spectrum.

There is no strong systematic difference in slope steepness when TRS is compared to MASME: in $\sim 45\%$ ($\sim 60\%$) of all flares the inferred average MASME slopes (ζ_1 from Table 2) are steeper than the TRS slope $\zeta_{\text{TRS,noCH}}$ ($\zeta_{\text{TRS,CH}}$). The MASME-TRS slope difference is quite high ($\sim 50 - 65\%$) for generally weak flares with only few TRS segments, but decreases to $\sim 20 - 30\%$ for generally brighter flares with the number of TRS segments $\gtrsim 10$ (black and grey circles and lines in panel a). We believe that the major reason for the observed MASME-TRS slope difference is not the presence or absence of the “characteristic” background, which contributes only a few percent to the difference (offset between the grey and black lines), but is rather due to the poor sampling of the temperature-density trajectory slope by the TRS method when only few TRS segments are available in the case of weak flares.

Panel b of Figure 14 shows that the peak flare temperatures $T_{\text{pk,TRS,noCH}}$ and $T_{\text{pk,TRS,CH}}$ obtained from the TRS method are essentially the same, and MASME-vs.-TRS temperature differences are within 20%. A 20% difference in temperature corresponds to a $< 20\%$ difference in estimated loop sizes. Large scatter in temperatures are seen for $T \gtrsim 200$ MK; this inability to quantify very high plasma temperatures is expected given the 8 keV high-energy limit and low high-energy sensitivity of Chandra spectra.

Panel *c* of Figure 14 examines MASME *vs.* TRS estimates of the correction factors associated with flare prolonged heating or triggered flare events (the factor $F(\zeta)$ presented in §2.3). This comparison is restricted to 108 flares with a single average decay slope ζ_1 (i.e., flares with $\text{Flag}_1 = 01$ in Table 2). Here again the two methods generally agree within 20%.

We emerge with considerable confidence in the MASME approach. Except for temperatures $T \gtrsim 200$ MK, basic physical flare properties such as temperature, emission measure, and luminosity evolution are essentially the same using the TRS and MASME methods. Flare model parameters such as reheating corrections and loop sizes are also reproduced. A reasonable estimate for the precision of loop sizes is < 40%, understanding that the underlying model of Reale et al. (1997) may not be adequate for understanding the more complex flares. The advantage of the MASME method is its ability to treat weaker and more rapidly variable flares than TRS. In the case of COUP, we are able to study > 6 times more flares than could be studied using TRS by Favata et al. (2005).

B. ERROR ANALYSIS OF MASME SPECTRAL MODELING

Here we describe our estimation procedure of statistical errors on peak flare plasma temperature in our MASME modeling. This is important both for estimation of magnetic loop sizes and for identification of ‘superhot’ flares. We use the median absolute deviation (MAD) normalized by $0.6745/\sqrt{N}$

$$\Delta\text{Med}E = \text{median}|E_i - \text{Med}E|/0.6745/\sqrt{N} \quad (\text{B1})$$

where $|...|$ indicates absolute value, E_i is the energy of each of the N X-ray photons appearing within the sliding boxcar kernel used to calculate peak flare median energy $\text{Med}E$. The MAD is a well-established estimate of the uncertainty of the median which is scaled to the standard deviation when the distribution is Gaussian (Beers et al. 1990).

Figure 15*a* compares errors on median energy estimated using Monte-Carlo simulations for flaring PMS stars in the Cepheus B region (grey symbols from Getman et al. 2006) with errors on COUP peak flare median energy (black symbols) obtained with the simple MAD formula above. There is a perfect match between the two completely different methods of error analysis, even for different $\text{Med}E$ strata (circles vs. \times).

The errors on peak flare plasma temperature are shown in Figure 15*b*. They are derived through propagation of errors on peak flare $\text{Med}E$ using the simulation-based $T_{\text{obs},pk} - \text{Med}E$ calibration curves (Figure 1). Upper errors for many sources with $T_{\text{obs},pk} \gtrsim 300$ MK are unreliable due to the lack of calibration data above 700 MK (Figure 1). Lower 1σ errors

are generally < 20% for $T_{obs,pk} < 50$ MK, < 30% for $T_{obs,pk} < 100$ MK, < 40% for $T_{obs,pk} < 200$ MK, and $\sim 60\%$ for the hottest flares.

We now further consider how uncertainties of inferred X-ray column densities may affect the errors of derived flare peak plasma temperatures shown in Figure 15b. First, it is important to note that 89% of super-hot flares (compared to 50% for cooler flares) are found in stars for which their inferred X-ray column densities are $\log N_H > 21.3 \text{ cm}^{-2}$ (Figure 16). This indicates that the super-hot flares are not a result of some data analysis bias, such as an effect of a systematic underestimate of N_H , but rather related to real physical phenomena relating to actively accreting disks around young stars, as it is shown in Paper II.

Second, because the studied COUP stars are extremely strong sources with thousands of counts, statistically, their $\log N_H$ is measured with very high accuracy. Formal statistical uncertainties are less than ± 0.03 dex (1-sigma) for sources with $\log N_H > 21.2 \text{ cm}^{-2}$ and less than ± 0.07 dex for most of the softer COUP sources. Such statistical errors on N_H have only marginal effects on the resulting temperature errors. For example, in a representative case of a super-hot flare from the COUP source #1309 with the $\log N_H = 22.00 \pm 0.02 \text{ cm}^{-2}$, the propagation of statistical errors on N_H will change the errors on plasma temperature of $T_{obs,pk} = 188^{+75}_{-67} \text{ MK}$ shown in Figure 15b from 40% to 53% and from 36% to 43% of an inferred mean temperature value for the upper and lower error limits, respectively. For a representative case of a cooler flare from COUP source #1492 with $\log N_H = 21.07 \pm 0.05 \text{ cm}^{-2}$, its errors on temperature of $T_{obs,pk} = 51^{+21}_{-19} \text{ MK}$ will change from 41% to 50% and from 37% to 38%, for the upper and lower error limits, respectively.

However, for the group of 8 extremely soft sources¹¹ with their reported $\log N_H$ values truncated at 20.0 cm^{-2} , the spectral model assumed by Getman et al. (2005) used to derive $\log N_H$ (two plasma MEKAL temperatures with $0.3 \times$ solar elemental abundances with Wisconsin gas absorption) is not sufficiently complex to fit the observed spectra well around the O VII and O VIII emission line complex. The reason is that spectral lines are present from FIP-related abundance anomalies which are not in the Getman et al. spectral model. These abundance effects are documented in detail by Maggio et al. (2007) for nearly the same sample of bright COUP stars as we analyze here. We re-fitted these 8 extremely soft spectra with two-temperature component VMEKAL models with individual elemental abundances as free parameters to obtain statistically good spectral fits. In accord with the results of Maggio et al. who used VAPEC models, we find that while for some of these spectra (#71, 597, 1481) their formal $\log N_H$ reported by XSPEC continue to be less than 20.0, for others their inferred $\log N_H$ may increase to $20.5\text{-}20.7 \text{ cm}^{-2}$. In the former cases,

¹¹These are COUP stars ## 71, 152, 394, 597, 971, 1481, 1516, 1595.

our calibration curves in Figure 1 assuming $\log N_H = 20.0 \text{ cm}^{-2}$ will not change due to the insensitivity of ACIS-I spectra to very low column densities. In the latter cases, the shift from $\log N_H = 20.0$ to $20.5 - 20.7 \text{ cm}^{-2}$ only slightly affects the lower error limits on peak flare plasma temperatures, which are typically around 30 MK. For example, the lower error on the plasma temperature $T_{obs,pk} = 27^{+7}_{-6} \text{ MK}$ of the source # 1595 will change only from 22% to 26% of an inferred mean temperature value when the shift from $\log N_H = 20 \text{ cm}^{-2}$ towards newly inferred 20.5 cm^{-2} is applied.

Time-integrated COUP spectra are typically several times stronger than spectra of individual flares. To take advantage of this fact in our flare analysis, we fixed column densities to N_H values derived from the two-temperature fits of time-integrated COUP spectra (Getman et al. 2005a). To verify if this produces a source of systematic uncertainty on column density, flare spectra were extracted within flare time range of $[t_{\text{flare1}} - t_{\text{flare2}}]$ and fitted by one-temperature WABS \times MEKAL model with $0.3 \times$ solar abundances allowing both temperature and column density to be free parameters. Figure 16 comparing column densities resulted from these flare fits, N_{Hf} , with column densities from time-integrated fits, N_H , shows no systematic differences in the case of super-hot flares (shorter solid regression line vs. dashed line), but suggests that N_H can be systematically overestimated by ~ 0.12 dex in the case of “cooler” flares (longer solid regression line vs. dashed line). This has only marginal effect on resulting temperature errors. For example, in a representative case of a “cooler” flare from COUP source #1492 considered above, this systematic shift will only change the temperature upper limit from 50% to 55% of an inferred mean temperature value of 51 MK.

Finally, systematic uncertainty on column densities may arise from performance uncertainties of the *Chandra*-ACIS detector. Such uncertainties have been evaluated by Drake et al. (2006). They show that in 10^4 source count regime appropriate for COUP flares, instrumental uncertainties for unabsorbed ($\log N_H \sim 20 \text{ cm}^{-2}$) sources may become comparable to (but not exceed) statistical uncertainties. For example, their spectral simulations predict a 0.07 dex instrumental systematic error on N_H , which is similar to our statistical errors of $\lesssim 0.07$ dex for soft COUP sources.

We thus find that the typical flare peak temperature errors shown in Figure 15b (typically 20-40%) could be slightly larger (typically 25-55%) if statistical and systematic uncertainties of $\log N_H$ values are applied. There is no evidence that the super-hot temperatures are an artifact of our analysis procedures or uncertainties. From equations (1)–(3), 25-55% errors on peak flare temperature result in 15-30% errors on inferred loop sizes.

As with median energies, we expect the statistical errors on COUP peak flare X-ray luminosities to be comparable with those obtained from Monte-Carlo simulations of Cepheus B

sources which are $\lesssim 0.2$ dex (see bottom-right panel in Figure 12 in Getman et al. 2006).

REFERENCES

- Arnaud, K. A. 1996, Astronomical Data Analysis Software and Systems V, 101, 17
- Aschwanden, M. J., & Alexander, D. 2001, Sol. Phys., 204, 91
- Aschwanden, M. J., Stern, R. A., Güdel, M. 2008, ApJ, 672, 659
- Albacete Colombo, J. F., Caramazza, M., Flaccomio, E., Micela, G., & Sciortino, S. 2007, A&A, 474, 495
- Beers, T. C., Flynn, K., & Gebhardt, K. 1990, AJ, 100, 32
- Caramazza, M., Flaccomio, E., Micela, G., Reale, F., Wolk, S. J., & Feigelson, E. D. 2007, A&A, 471, 645
- Crespo-Chacón, I., Micela, G., Reale, F., Caramazza, M., López-Santiago, J., & Pillitteri, I. 2007, A&A, 471, 929
- Donati, J.-F., et al. 2007, MNRAS, 380, 1297
- Drake, J. J., Ratzlaff, P., Kashyap, V., Edgar, R., Izem, R., Jerius, D., Siemiginowska, A., & Vikhlinin, A. 2006, Proc. SPIE, 6270,
- Farnik et al. 1996, Sol. Phys., 168, 331
- Favata, F., Flaccomio, E., Reale, F., Micela, G., Sciortino, S., Shang, H., Stassun, K. G., & Feigelson, E. D. 2005, ApJS, 160, 469
- Feigelson, E. D., et al. 2005, ApJS, 160, 379
- Feigelson, E., Townsley, L., Güdel, M., & Stassun, K. 2007, in Protostars and Planets V, (B. Reipurth et al., eds.), 313
- Flaccomio, E., Micela, G., Sciortino, S., Feigelson, E. D., Herbst, W., Favata, F., Harnden, F. R., Jr., & Vrtilek, S. D. 2005, ApJS, 160, 450
- Forbes, T. G., & Acton, L. W. 1996, ApJ, 459, 330
- Franciosini, E., et al. 2007, A&A, 468, 485
- Getman, K. V., & Livshitz, M. A. 1999, Astronomy Reports, 43, 615

- Getman, K. V., & Livshits, M. A. 2000, *Astronomy Reports*, 44, 255
- Getman, K. V., Flaccomio, E., Broos, P. S. and 21 co-authours 2005, *ApJS*, 160, 319
- Getman, K. V., Feigelson, E. D., Grosso, N., McCaughrean, M. J., Micela, G., Broos, P., Garmire, G., & Townsley, L. 2005, *ApJS*, 160, 353
- Getman, K. V., Feigelson, E. D., Townsley, L., Broos, P., Garmire, G., & Tsujimoto, M. 2006, *ApJS*, 163, 306
- Getman, K. V., Feigelson, E. D., Micela, G., Jardine, M. M., Gregory, S. G., & Garmire, G. P. 2008, *ApJ*, in press (Paper II)
- Giardino, G., Favata, F., Micela, G., & Reale, F. 2004, *A&A*, 413, 669
- Giardino, G., Favata, F., Micela, G., Sciortino, S., & Winston, E. 2007, *A&A*, 463, 275
- Glassgold, A. E., Feigelson, E. D., Montmerle, T., & Wolk, S. 2005, *Chondrites and the Protoplanetary Disk*, 341, 165
- Grosso, N., Montmerle, T., Feigelson, E. D., & Forbes, T. G. 2004, *A&A*, 419, 653
- Güdel, M. 2004, *A&A Rev.*, 12, 71
- Güdel, M., et al. 2007, *A&A*, 468, 353
- Hartmann, L. 1998, *Accretion Processes in Star Formation*, Cambridge: Cambridge Univ. Press
- Hiei, E. 1994, *IAU Colloq. 144: Solar Coronal Structures*, 163
- Hiei, E. 1997, *Memorie della Societa Astronomica Italiana*, 68, 491
- Hiei, E., Hundhausen, A. J., & Burkepile, J. 1997, *Magnetic Reconnection in the Solar Atmosphere*, 111, 383
- Hong, J., Schlegel, E. M., & Grindlay, J. E. 2004, *ApJ*, 614, 508
- Imanishi, K., Koyama, K., & Tsuboi, Y. 2001, *ApJ*, 557, 747
- Isobe, H., Shibata, K., Yokoyama, T., & Imanishi, K. 2003, *PASJ*, 55, 967
- Jardine, M., & Unruh, Y. C. 1999, *A&A*, 346, 883
- Jardine, M., Cameron, A. C., Donati, J.-F., Gregory, S. G., & Wood, K. 2006, *MNRAS*, 367, 917

- Kahler, S. 1977, ApJ, 214, 891
- Kopp, R. A., & Pneuman, G. W. 1976, Sol. Phys., 50, 85
- Long, M., Romanova, M. M., & Lovelace, R. V. E. 2008, MNRAS, in press (arXiv:0802.2308)
- Luhmann, J. G., Gosling, J. T., Hoeksema, J. T., & Zhao, X. 1998, J. Geophys. Res., 103, 6585
- Maggio, A., Flaccomio, E., Favata, F., Micela, G., Sciortino, S., Feigelson, E. D., & Getman, K. V. 2007, ApJ, 660, 1462
- Massi, M., et al. 2007, ArXiv e-prints, 712, arXiv:0712.0718
- Osten, R. A., & Brown, A. 1999, ApJ, 515, 746
- Osten, R. A., Drake, S., Tueller, J., Cummings, J., Perri, M., Moretti, A., & Covino, S. 2007, ApJ, 654, 1052
- Pallavicini, R., Serio, S., & Vaiana, G. S. 1977, ApJ, 216, 108
- Preibisch, T., et al. 2005b, ApJS, 160, 401
- Priest, E. R., & Forbes, T. G. 2002, A&A Rev., 10, 313
- Reale, F., Betta, R., Peres, G., Serio, S., & McTiernan, J. 1997, A&A, 325, 782
- Reale, F., & Micela, G. 1998, A&A, 334, 1028
- Reale, F., Güdel, M., Peres, G., & Audard, M. 2004, A&A, 416, 733
- Reale, F. 2007, A&A, 471, 271
- Rosner, R., Tucker, W. H., & Vaiana, G. S. 1978, ApJ, 220, 643
- Serio, S., Reale, F., Jakimiec, J., Sylwester, B., & Sylwester, J. 1991, A&A, 241, 197
- Shu, F. H., Shang, H., Glassgold, A. E., & Lee, T. 1997, Science, 277, 1475
- Shu, F. H., Najita, J. R., Shang, H., & Li, Z.-Y. 2000, in Protostars and Planets IV, Tucson: Univ. Arizona Press, 789
- Siess, L., Dufour, E., & Forestini, M. 2000, A&A, 358, 593
- Stassun, K. G., van den Berg, M., Feigelson, E., & Flaccomio, E. 2006, ApJ, 649, 914

- Sturrock, P. A. 1966, *Nature*, 211, 695
- Švestka, Z., Fárník, F., Hudson, H. S., Uchida, Y., Hick, P., & Lemen, J. R. 1995, *Sol. Phys.*, 161, 331
- Svestka, Z., Farnik, F., Hick, P., Hudson, H. S., & Uchida, Y. 1997, *Sol. Phys.*, 176, 355
- Sylwester, B., Sylwester, J., Serio, S., Reale, F., Bentley, R. D., & Fludra, A. 1993, *A&A*, 267, 586
- Testa, P., Reale, F., Garcia-Alvarez, D., & Huenemoerder, D. P. 2007, *ApJ*, 663, 1232
- Tsuboi, Y., Koyama, K., Murakami, H., Hayashi, M., Skinner, S., & Ueno, S. 1998, *ApJ*, 503, 894
- Wargelin, B. J., Kashyap, V. L., Drake, J. J., García-Alvarez, D., & Ratzlaff, P. W. 2007, ArXiv e-prints, 712, arXiv:0712.2791
- Wolk, S. J., Harnden, F. R., Jr., Flaccomio, E., Micela, G., Favata, F., Shang, H., & Feigelson, E. D. 2005, *ApJS*, 160, 423

Table 1. Flare properties 1

Source (1)	FlareNo (2)	NCf (cnts) (3)	Bgf (cnts) (4)	MEF (keV) (5)	t _{char1} (ks) (6)	t _{char2} (ks) (7)	t _{flare1} (ks) (8)	t _{flare2} (ks) (9)	CR _{char} (cnts/ks) (10)	CR _{flare,pk} (cnts/ks) (11)	t _{CR,pk} (ks) (12)	t _{T,pk} (ks) (13)	t _{EM,pk} (ks) (14)	t _{exp} (ks) (15)	t _{sep} (ks) (16)
7	1	3209	11.7	1.31	60.0	100.0	930.0	967.0	38.3	164.0 ± 11.5	951.1	948.9	951.2	967.0	960.0
9	1	3980	6.1	1.55	160.0	200.0	523.0	558.0	12.8	210.0 ± 7.7	542.4	538.5	544.2	553.0	549.0
11	1	1158	3.5	2.17	883.0	940.0	977.0	1009.0	3.4	105.5 ± 6.3	986.9	978.6	986.5	993.0	997.5
23	1	4370	13.5	1.37	440.0	480.0	740.0	788.0	51.8	306.7 ± 15.5	747.0	746.0	747.1	752.0	750.0
27	1	350	5.9	1.37	220.0	260.0	258.0	302.0	4.4	14.2 ± 1.8	282.6	283.2	285.4	295.0	
27	2	1653	28.1	1.31	220.0	260.0	681.0	890.0	4.4	19.5 ± 2.0	710.8	720.9	711.8	743.0	743.0
28	1	13308	22.9	1.44	200.0	300.0	615.0	790.0	3.6	300.3 ± 10.7	623.6	616.0	622.9	680.0	745.0
43	1	2744	7.5	1.42	470.0	520.0	665.0	800.0	4.3	39.4 ± 2.8	716.5	709.5	714.1	770.0	730.0
57	1	724	0.4	1.26	910.0	950.0	185.0	272.0	3.2	16.7 ± 1.9	202.7	205.6	204.5	221.0	233.5
57	2	306	0.2	1.22	910.0	950.0	852.0	900.0	3.2	11.2 ± 1.6	870.6	864.6	871.4	879.0	883.0
62	1	5933	30.6	1.39	245.0	295.0	260.0	788.0	3.0	30.9 ± 2.5	505.2	465.6	535.1	560.0	650.0
62	2	885	5.7	1.42	245.0	295.0	902.0	1000.0	3.0	19.3 ± 2.0	939.1	938.7	946.6	963.0	953.0
66	1	1667	4.7	1.52	0.0	100.0	468.0	658.0	1.6	25.7 ± 2.3	539.5	502.0	515.7	558.0	560.0
67	1	638	1.8	1.29	212.0	250.0	923.0	972.0	6.5	28.1 ± 2.5	933.7	931.8	934.1	948.0	948.0
71	1	2654	10.9	1.15	980.0	1010.0	481.0	770.0	3.6	35.1 ± 2.7	505.2	504.3	507.7	518.0	561.0
90	1	4368	15.9	2.03	650.0	770.0	960.0	1090.0	0.9	148.2 ± 5.3	979.1	966.0	982.0	1009.0	1006.0
101	1	8769	19.5	1.44	1100.0	1140.0	0.0	300.0	0.8	223.0 ± 9.4	1.9	3.9	2.7	40.0	29.0
107	1	2205	47.1	1.36	1080.0	1120.0	156.0	250.0	7.3	51.0 ± 3.2	174.1	171.4	171.4	200.0	201.5
108	1	1477	3.6	1.51	0.0	90.0	920.0	1000.0	3.7	36.4 ± 2.7	933.4	931.8	936.4	952.0	972.0
108	2	1223	2.6	1.45	0.0	90.0	1070.0	1128.0	3.8	46.8 ± 4.0	1080.2	1091.4	1081.2	1090.0	1108.0
112	1	3590	19.1	1.31	845.0	980.0	447.0	758.0	2.5	31.8 ± 2.6	499.5	490.6	498.6	530.0	560.0
113	1	2718	36.0	1.31	0.0	100.0	0.0	500.0	6.0	10.1 ± 1.3	443.7	242.1	421.1	485.0	487.0
113	2	2797	33.1	1.32	0.0	100.0	500.0	960.0	6.0	11.8 ± 1.4	700.7	661.6	648.0	750.0	800.0
115	1	321	0.4	1.77	425.0	469.0	1107.3	1127.3	4.0	40.6 ± 3.8	1115.8	1117.6	1115.4	1121.8	1117.0
122	1	2068	1.9	1.46	750.0	780.0	172.0	268.0	0.9	46.5 ± 3.1	214.1	205.6	215.9	228.0	224.5
123	1	1031	19.8	1.51	700.0	760.0	445.0	531.0	2.5	24.3 ± 2.3	459.6	481.5	463.3	506.0	501.0
123	2	1021	17.9	1.48	700.0	760.0	925.0	1003.0	2.5	32.7 ± 2.6	950.5	951.2	951.2	964.0	966.0
124	1	1272	34.7	1.44	664.0	760.0	440.0	530.0	3.2	32.7 ± 2.6	459.6	482.7	461.0	473.0	515.0
124	2	859	26.6	1.40	664.0	760.0	931.0	1000.0	3.2	25.2 ± 2.3	950.5	952.3	953.5	970.0	979.0
131	1	2751	8.1	1.74	20.0	70.0	270.0	540.0	3.0	44.9 ± 3.0	316.8	299.1	318.5	408.0	423.0
139	1	686	1.6	1.19	160.0	220.0	19.7	83.5	3.7	25.2 ± 2.3	37.1	24.4	39.2	52.0	64.0
139	2	730	2.4	1.25	160.0	220.0	864.0	960.0	3.7	16.9 ± 1.9	882.0	890.8	883.9	901.0	898.0
141	1	2857	1.0	1.46	390.0	460.0	1070.0	1140.0	6.4	75.7 ± 4.8	1094.2	1082.3	1099.4	1120.0	1108.0
141	2	1126	0.6	1.34	390.0	460.0	5.5	48.0	6.4	45.0 ± 3.7	13.3	14.1	15.3	40.0	26.0
142	1	642	0.3	1.44	640.0	690.0	23.0	45.0	3.1	193.3 ± 12.3	27.9	27.8	27.8	33.0	29.2
142	2	2138	3.4	1.33	640.0	690.0	857.0	1100.0	2.9	27.1 ± 3.1	959.0	896.5	962.6	986.0	996.0
150	1	2139	3.6	1.39	685.0	750.0	423.0	714.0	4.1	25.2 ± 2.3	448.2	448.5	449.6	468.0	466.0
152	1	808	1.7	1.15	1070.0	1128.0	40.0	181.0	3.8	16.5 ± 1.9	59.9	64.3	65.4	86.0	104.0
152	2	1973	3.3	1.21	1070.0	1128.0	618.0	889.0	3.8	28.0 ± 2.4	630.8	628.6	633.1	651.0	800.0
160	1	3533	2.9	3.22	200.0	300.0	731.0	787.0	0.4	283.0 ± 10.1	737.8	731.2	738.0	745.0	781.0
173	1	882	1.0	1.29	175.0	195.0	690.0	733.0	10.1	33.5 ± 3.3	709.8	714.1	712.9	725.0	726.0
183	1	546	0.6	2.11	955.0	985.0	402.0	460.0	3.7	19.5 ± 2.0	419.6	408.6	421.1	432.0	435.0
183	2	1216	0.9	2.01	955.0	985.0	686.0	770.0	3.7	29.6 ± 2.5	710.8	703.8	707.2	726.0	735.0
202	1	793	1.9	1.45	687.0	730.0	173.0	219.0	3.2	35.5 ± 2.7	191.3	198.8	190.8	205.0	198.0
205	1	1360	1.2	1.44	160.0	240.0	880.0	962.0	3.4	26.1 ± 2.3	910.6	918.1	915.9	942.0	956.0
205	2	1864	2.5	1.32	160.0	240.0	958.5	1124.0	3.4	44.3 ± 3.0	979.1	974.0	978.6	999.0	988.2
223	1	2789	4.2	2.07	10.0	40.0	245.0	322.0	5.6	106.0 ± 5.6	256.9	252.4	255.8	285.0	267.0
223	2	1808	3.8	2.27	10.0	40.0	1070.0	1140.0	5.6	48.0 ± 3.9	1086.6	1081.2	1086.9	1113.0	1100.0
262	1	2997	0.9	2.21	685.0	760.0	155.0	255.0	7.7	62.6 ± 4.4	169.4	173.7	169.2	194.0	205.0

Table 1—Continued

Source (1)	FlareNo (2)	NCf (cnts) (3)	Bgf (cnts) (4)	MEF (keV) (5)	t _{char1} (ks) (6)	t _{char2} (ks) (7)	t _{flare1} (ks) (8)	t _{flare2} (ks) (9)	CR _{char} (cnts/ks) (10)	CR _{flare,pk} (cnts/ks) (11)	t _{CR,pk} (ks) (12)	t _{T,pk} (ks) (13)	t _{EM,pk} (ks) (14)	t _{exp} (ks) (15)	t _{sep} (ks) (16)
270	1	624	0.3	1.19	860.0	900.0	36.0	89.0	4.8	19.7 ± 2.1	65.7	51.7	60.9	78.0	80.0
310	1	663	1.4	1.66	880.0	910.0	653.0	729.0	3.2	19.2 ± 2.0	665.1	661.6	668.5	679.0	696.5
323	1	1513	3.8	1.89	915.0	980.0	218.0	318.0	3.2	51.5 ± 3.2	236.9	238.7	236.4	262.0	239.0
325	1	445	2.6	1.32	640.0	740.0	65.0	101.0	3.9	25.4 ± 2.3	77.1	78.0	78.0	90.0	86.5
325	2	523	3.4	1.32	640.0	740.0	413.0	461.0	3.9	31.7 ± 2.6	436.7	432.5	434.8	450.0	457.0
325	3	630	5.8	1.33	640.0	740.0	921.0	1003.0	3.9	14.0 ± 1.8	950.5	934.1	947.8	971.0	962.0
331	1	2121	1.7	2.67	280.0	310.0	88.8	102.0	1.4	351.3 ± 15.4	95.2	95.1	96.2	97.0	99.0
331	2	1363	6.9	3.08	280.0	310.0	1082.0	1136.5	1.4	41.9 ± 5.3	1107.8	1123.3	1125.6	1121.0	1134.0
332	1	2862	4.9	2.61	860.0	980.0	2.0	560.0	0.5	21.0 ± 2.1	59.9	19.8	48.3	260.0	258.0
342	1	2440	0.8	2.38	180.0	220.0	624.0	680.0	12.4	86.1 ± 7.0	643.5	640.0	644.5	663.0	655.0
343	1	6138	0.7	1.40	840.0	960.0	198.0	287.0	24.9	118.6 ± 6.9	212.6	210.2	211.3	232.0	222.0
365	1	691	0.3	2.53	1110.0	1140.0	688.0	720.0	3.8	50.7 ± 4.2	700.4	699.3	703.8	708.0	710.0
382	1	428	0.6	1.32	442.0	505.0	47.0	96.0	4.3	12.6 ± 1.7	59.9	58.6	60.9	73.0	70.5
382	2	296	0.6	1.36	442.0	505.0	681.0	723.0	4.3	11.9 ± 1.6	693.6	693.6	697.0	706.0	701.0
387	1	1058	0.4	1.35	20.0	100.0	212.0	247.0	18.1	55.4 ± 4.8	224.0	218.2	223.9	233.0	230.0
394	1	1004	53.1	1.25	70.0	100.0	726.0	913.0	3.4	15.3 ± 1.8	762.2	749.4	758.5	782.0	882.5
417	1	827	0.9	1.38	620.0	680.0	453.0	530.0	3.7	27.3 ± 2.4	488.1	481.5	486.1	502.0	500.4
431	1	5439	14.9	1.44	240.0	320.0	0.0	220.0	15.6	71.7 ± 6.9	1.4	6.1	7.3	38.0	105.0
449	1	2601	3.3	2.24	500.0	530.0	709.0	981.0	5.1	38.0 ± 2.8	733.6	752.8	734.6	770.0	860.0
452	1	688	0.6	1.79	160.0	200.0	480.0	550.0	2.4	20.9 ± 2.7	493.5	494.1	499.8	505.0	507.0
454	1	2075	1.1	1.89	400.0	440.0	230.0	310.0	9.3	65.2 ± 4.4	245.5	238.7	245.5	270.0	274.0
454	2	3877	2.8	1.90	400.0	440.0	885.0	1084.0	9.3	56.0 ± 4.1	903.9	901.0	903.3	930.0	915.0
459	1	2370	7.0	1.33	650.0	700.0	1074.0	1130.0	4.6	126.7 ± 7.6	1083.5	1082.3	1084.6	1093.0	1099.0
470	1	1325	1.2	1.20	890.0	910.0	320.0	452.0	7.7	29.6 ± 3.1	390.1	347.0	385.8	406.0	419.0
485	1	2677	1.4	2.41	860.0	980.0	664.0	750.0	0.7	104.2 ± 4.5	676.5	674.2	675.3	690.0	683.0
490	1	896	6.5	1.71	280.0	320.0	665.0	748.0	5.2	48.1 ± 3.2	676.3	670.8	675.3	686.0	679.5
499	1	1369	10.7	1.51	620.0	650.0	178.0	291.0	3.9	25.7 ± 2.3	191.3	178.3	186.3	209.0	211.0
515	1	1213	2.2	1.77	619.0	650.0	247.0	456.0	2.8	21.3 ± 2.1	311.1	292.3	316.2	399.0	324.0
554	1	2095	0.9	3.69	385.0	435.0	0.0	100.0	1.8	34.6 ± 3.3	32.4	13.0	33.5	42.0	51.0
554	2	1585	0.6	3.84	385.0	435.0	477.0	547.0	1.8	40.7 ± 3.6	504.3	489.5	512.3	525.0	525.0
554	3	3831	2.4	3.61	385.0	435.0	850.0	1122.0	1.8	29.0 ± 3.1	983.9	909.0	952.3	1085.0	1010.0
561	1	3283	3.1	2.57	1080.0	1140.0	488.0	643.0	10.5	118.2 ± 5.9	511.9	507.7	510.0	522.0	553.0
567	1	1010	4.3	1.65	675.0	700.0	157.0	208.0	7.7	43.1 ± 3.7	161.8	164.6	163.5	174.0	168.5
567	2	1509	8.2	1.38	675.0	700.0	869.0	966.0	7.7	34.3 ± 3.3	888.7	882.8	889.6	906.0	916.0
567	3	2110	5.2	1.31	675.0	700.0	1074.0	1136.0	7.7	50.0 ± 3.9	1079.0	1074.3	1085.7	1096.0	1122.0
570	1	2478	1.9	3.44	670.0	760.0	153.0	318.0	0.5	28.0 ± 2.4	179.8	153.2	178.3	210.0	187.0
579	1	1828	2.8	1.79	50.0	100.0	892.0	960.0	3.0	93.1 ± 4.2	904.9	895.3	903.3	919.0	923.0
597	1	4710	4.7	1.15	635.0	695.0	858.0	1140.0	4.3	46.0 ± 3.0	887.7	870.3	891.9	950.0	965.0
600	1	726	0.8	1.33	1070.0	1140.0	470.0	551.0	3.2	11.2 ± 1.6	499.5	484.9	512.3	518.0	544.0
600	2	1025	1.2	1.39	1070.0	1140.0	653.0	774.0	3.2	22.7 ± 2.2	665.1	665.1	666.2	684.0	692.0
626	1	1621	8.9	1.71	1070.0	1140.0	729.0	920.0	3.4	34.8 ± 2.7	762.2	765.4	763.1	777.0	800.0
634	1	667	0.7	1.50	0.0	50.0	156.0	250.0	2.1	14.4 ± 1.8	162.7	164.6	164.6	183.0	172.0
645	1	741	0.9	1.98	465.0	490.0	698.0	780.0	1.6	14.2 ± 1.8	733.6	714.1	734.6	746.0	749.5
645	2	1600	1.3	1.98	465.0	490.0	864.0	992.0	1.6	21.8 ± 2.2	887.7	885.1	894.2	912.0	916.0
648	1	10053	13.0	1.49	50.0	75.0	164.0	516.0	23.8	53.3 ± 4.7	232.6	215.9	233.0	587.0	280.0
649	1	4279	15.3	1.86	40.0	100.0	185.0	785.0	1.2	66.1 ± 3.6	242.6	241.0	243.3	310.0	330.0
669	1	6729	6.6	1.56	490.0	516.0	782.0	1010.0	12.4	106.2 ± 6.5	846.2	862.3	842.9	920.0	883.0
670	1	6199	3.6	1.59	731.0	787.0	163.0	270.0	22.4	110.2 ± 6.6	175.5	169.2	174.9	184.0	188.0
670	2	2912	1.4	1.68	731.0	787.0	278.0	321.0	22.4	89.8 ± 6.0	295.4	303.7	298.0	309.0	313.0

Table 1—Continued

Source (1)	FlareNo (2)	NCf (cnts) (3)	Bgf (cnts) (4)	MEF (keV) (5)	t _{char1} (ks) (6)	t _{char2} (ks) (7)	t _{flare1} (ks) (8)	t _{flare2} (ks) (9)	CR _{char} (cnts/ks) (10)	CR _{flare,pk} (cnts/ks) (11)	t _{CR,pk} (ks) (12)	t _{T,pk} (ks) (13)	t _{EM,pk} (ks) (14)	t _{exp} (ks) (15)	t _{sep} (ks) (16)
682	1	2490	3.6	2.64	385.0	448.0	13.5	100.0	4.0	155.5 ± 8.3	21.9	14.1	21.0	35.0	35.0
682	2	711	3.2	1.97	385.0	448.0	464.0	540.0	4.1	32.5 ± 2.6	476.7	472.4	478.1	488.0	515.0
682	3	810	3.1	2.10	385.0	448.0	635.0	708.0	4.1	25.7 ± 2.3	653.7	652.5	653.7	670.0	670.0
682	4	684	2.7	2.36	385.0	448.0	867.0	930.0	3.8	30.0 ± 3.2	880.1	872.5	881.7	893.0	893.5
689	1	1374	62.9	1.32	260.0	290.0	863.0	980.0	4.8	22.2 ± 2.2	882.0	882.8	891.9	914.0	940.0
707	1	1022	2.1	1.55	1070.0	1140.0	429.0	535.0	3.2	22.2 ± 2.2	448.2	445.0	450.7	469.0	488.0
707	2	1054	2.6	1.55	1070.0	1140.0	624.0	752.0	3.2	22.4 ± 2.2	642.3	642.3	642.3	661.0	651.0
718	1	1662	0.4	1.64	640.0	690.0	1098.0	1132.0	14.1	59.9 ± 4.3	1113.3	1110.8	1121.1	1121.0	1128.0
720	1	3821	13.3	2.09	505.0	540.0	620.0	923.0	4.3	32.3 ± 2.6	687.9	655.9	695.8	780.0	761.0
737	1	2374	2.1	1.77	160.0	220.0	680.0	900.0	1.6	38.9 ± 2.8	710.8	719.8	714.1	725.0	775.0
752	1	29545	156.7	1.51	1075.0	1140.0	55.0	320.0	4.3	624.5 ± 15.2	87.0	74.5	88.2	102.0	105.0
753	1	1194	12.6	1.61	620.0	660.0	440.0	530.0	4.5	73.2 ± 5.5	448.8	448.5	449.6	460.0	451.0
761	1	1252	0.6	1.60	520.0	560.0	926.0	965.0	8.0	108.4 ± 5.6	934.4	931.8	934.1	942.0	937.0
794	1	470	3.5	1.80	180.0	210.0	264.0	306.0	2.8	19.0 ± 2.0	288.3	271.8	290.0	298.0	297.0
801	1	5713	4.4	1.74	660.0	720.0	720.0	1140.0	8.8	49.9 ± 29.9	1010.5	865.7	958.0	1098.0	1010.0
828	1	3009	1.4	1.68	710.0	740.0	390.0	550.0	6.4	29.3 ± 3.1	477.7	464.4	494.1	520.0	511.0
828	2	1287	0.8	1.63	710.0	740.0	636.0	723.0	6.4	47.9 ± 3.8	648.9	648.0	649.1	669.0	669.0
848	1	4292	1.2	1.55	620.0	900.0	1070.0	1140.0	1.8	128.5 ± 5.0	1076.1	1070.9	1076.6	1110.0	1094.0
867	1	1199	0.2	1.65	940.0	1000.0	294.0	318.0	11.2	128.5 ± 8.3	306.9	306.0	307.1	314.0	313.0
871	1	478	0.7	1.60	943.0	980.0	888.0	941.0	3.4	26.7 ± 3.0	901.5	898.8	903.3	911.0	930.0
874	1	5310	0.9	3.95	0.0	40.0	441.0	552.0	1.2	97.4 ± 4.3	471.0	471.3	471.3	490.0	502.5
881	1	2990	117.4	1.34	0.0	100.0	390.0	747.0	0.9	34.4 ± 2.7	442.4	423.4	443.9	471.0	700.0
891	1	2379	87.4	2.84	28.0	55.0	59.0	200.0	3.7	106.8 ± 5.6	74.2	67.7	72.3	88.0	80.0
891	2	8674	281.6	2.71	28.0	55.0	686.0	1140.0	3.7	125.7 ± 6.1	713.6	707.2	714.1	748.0	800.0
894	1	985	1.2	2.28	70.0	100.0	207.0	307.0	1.6	27.3 ± 2.4	225.5	222.7	229.6	234.0	254.0
894	2	1565	0.9	2.48	70.0	100.0	618.0	694.0	1.6	59.8 ± 3.4	625.1	621.7	625.2	639.0	654.0
894	3	467	0.5	2.55	70.0	100.0	732.0	775.0	1.6	17.4 ± 1.9	750.7	742.6	749.4	760.0	753.0
915	1	5828	4.2	2.80	940.0	970.0	990.0	1140.0	9.3	282.7 ± 57.3	1010.5	1008.2	1008.2	1075.0	1103.0
932	1	934	36.3	1.40	385.0	460.0	498.0	545.0	6.0	34.6 ± 2.7	516.7	508.9	515.7	534.0	531.0
942	1	1532	1.0	2.17	880.0	930.0	161.0	254.0	6.1	31.7 ± 3.2	184.6	177.1	182.8	205.0	212.0
942	2	2711	0.9	2.51	880.0	930.0	666.0	756.0	6.1	87.6 ± 5.1	683.2	681.0	683.3	699.0	694.0
960	1	3568	2.8	1.39	0.0	100.0	390.0	450.0	0.9	336.1 ± 12.2	396.8	398.3	397.2	413.0	413.0
971	1	4880	1.3	1.35	650.0	690.0	41.0	96.0	17.8	197.4 ± 8.7	58.5	54.0	59.7	80.0	71.0
976	1	2179	1.3	1.89	0.0	90.0	660.0	790.0	0.7	67.8 ± 3.6	682.2	681.0	681.0	715.0	685.0
976	2	825	1.6	1.68	0.0	90.0	842.0	1008.0	0.7	15.1 ± 1.8	870.6	869.1	883.9	916.0	923.0
982	1	512	0.7	1.57	870.0	910.0	168.0	226.0	3.2	18.5 ± 2.0	197.0	188.5	198.8	210.0	214.0
982	2	1701	2.3	1.70	870.0	910.0	224.0	410.0	3.2	28.8 ± 2.4	259.8	246.7	255.8	295.0	260.0
985	1	1723	0.5	1.77	20.0	58.0	58.0	102.0	25.9	63.5 ± 5.1	75.6	72.3	73.4	84.0	78.0
985	2	1247	0.3	1.70	20.0	58.0	288.0	316.0	25.9	76.7 ± 5.6	301.1	300.3	302.5	308.0	307.5
993	1	568	1.1	2.04	950.0	980.0	259.0	317.0	2.8	15.4 ± 1.8	276.9	276.3	282.0	289.0	290.5
997	1	4304	1.1	1.61	1070.0	1140.0	2.0	102.0	9.3	78.3 ± 4.8	17.1	14.1	17.5	47.0	68.5
1028	1	1144	0.7	2.20	150.0	220.0	847.0	918.0	3.0	44.4 ± 3.0	864.9	861.1	864.6	877.0	904.0
1040	1	4532	7.1	2.75	0.0	220.0	229.0	280.0	2.5	296.4 ± 10.4	239.4	231.9	239.8	255.0	256.0
1044	1	793	2.3	1.48	740.0	780.0	184.0	290.0	2.7	17.2 ± 1.9	219.8	230.7	219.3	240.0	255.0
1045	1	901	0.4	1.81	1080.0	1140.0	166.0	226.0	1.8	37.4 ± 2.5	186.7	176.0	187.4	202.0	211.0
1070	1	886	0.7	2.22	860.0	920.0	407.0	470.0	2.9	45.6 ± 4.1	415.8	421.1	416.5	428.0	426.0
1080	1	1305	7.7	2.76	1080.0	1140.0	744.0	781.0	2.8	80.4 ± 5.3	764.1	763.1	766.5	775.0	770.5
1083	1	11137	12.5	1.53	1070.0	1140.0	0.0	790.0	10.9	46.0 ± 4.0	100.9	97.3	162.3	210.0	325.0
1090	1	1105	49.1	1.60	400.0	450.0	156.0	307.0	2.3	16.2 ± 1.9	197.0	194.2	182.8	228.0	225.0

Table 1—Continued

Source	FlareNo	N Cf (cnts)	Bgf (cnts)	MEf (keV)	t_{char1} (ks)	t_{char2} (ks)	t_{flare1} (ks)	t_{flare2} (ks)	CR _{char} (cnts/ks)	CR _{flare,pk} (cnts/ks)	$t_{CR,pk}$ (ks)	$t_{T,pk}$ (ks)	$t_{EM,pk}$ (ks)	t_{exp} (ks)	t_{sep} (ks)
(1)	(2)	(3)	(4)	(5)	(6)	(7)	(8)	(9)	(10)	(11)	(12)	(13)	(14)	(15)	(16)
1090	2	2292	139.3	1.58	400.0	450.0	680.0	1108.0	2.3	12.8 ± 1.7	899.2	920.4	873.7	961.0	924.0
1096	1	2146	6.8	1.69	440.0	480.0	765.0	872.0	1.2	209.6 ± 56.5	790.7	784.8	784.8	857.0	790.0
1114	1	9496	27.8	2.08	617.0	643.0	424.0	638.0	19.5	145.9 ± 7.6	446.7	441.6	446.2	461.0	560.0
1127	1	1249	4.6	1.69	160.0	200.0	470.0	535.0	4.0	70.6 ± 5.1	494.2	495.2	494.1	508.0	500.5
1134	1	1083	14.7	1.28	42.0	100.0	619.0	729.0	3.4	15.3 ± 1.8	653.7	633.1	653.7	679.0	691.0
1140	1	1487	0.5	2.49	0.0	30.0	943.0	992.0	1.1	45.8 ± 3.0	962.0	955.8	961.5	976.0	981.0
1149	1	512	1.0	1.61	680.0	710.0	31.0	86.0	2.0	22.3 ± 2.7	43.5	40.3	44.9	54.0	53.0
1149	2	1160	2.3	1.63	680.0	710.0	852.0	982.0	2.1	16.2 ± 1.9	904.9	893.1	914.7	937.0	935.0
1151	1	1270	0.4	1.37	920.0	940.0	520.0	546.0	20.9	88.5 ± 7.7	533.2	531.7	532.8	541.0	539.0
1158	1	524	0.5	1.96	420.0	455.0	8.0	46.0	4.2	32.5 ± 3.4	18.9	15.3	19.8	29.0	31.0
1158	2	395	0.5	1.99	420.0	455.0	218.0	255.0	4.2	27.3 ± 3.1	227.7	222.7	228.4	235.0	236.0
1158	3	1266	1.1	1.82	420.0	455.0	625.0	706.0	4.4	36.2 ± 2.7	642.3	640.0	638.8	666.0	668.0
1161	1	1885	0.8	1.60	480.0	520.0	0.0	72.0	4.8	41.4 ± 2.9	31.4	55.2	35.8	55.0	44.0
1165	1	1346	1.2	3.35	700.0	760.0	403.0	490.0	1.4	48.9 ± 4.2	418.6	443.9	417.7	431.0	442.0
1178	1	443	4.9	1.78	930.0	970.0	722.0	762.0	2.1	34.6 ± 3.5	738.0	740.3	740.3	748.0	748.0
1236	1	982	4.0	1.45	940.0	1000.0	259.0	290.0	3.0	100.9 ± 6.2	268.6	267.2	269.5	275.0	280.0
1246	1	5240	2.2	1.63	160.0	254.0	840.0	940.0	1.8	192.7 ± 6.0	853.5	850.9	855.4	887.0	922.0
1248	1	2055	2.1	1.39	400.0	460.0	192.0	267.0	12.0	44.5 ± 3.7	211.2	207.9	206.8	230.0	230.0
1252	1	2166	3.0	1.60	420.0	540.0	986.0	1122.0	2.8	117.4 ± 6.4	996.1	997.9	996.8	1003.0	998.5
1261	1	745	0.7	1.46	200.0	540.0	670.0	770.0	1.6	15.5 ± 1.8	687.9	700.4	686.7	698.0	701.0
1268	1	1769	0.9	1.96	167.0	205.0	892.0	991.0	2.1	25.6 ± 2.3	950.5	913.6	944.4	972.0	970.0
1309	1	1501	0.9	2.01	505.0	535.0	848.0	954.0	6.7	34.9 ± 2.7	868.1	869.1	869.1	883.0	900.0
1311	1	969	1.1	1.23	687.0	770.0	510.0	710.0	3.9	19.7 ± 2.1	539.5	532.8	540.8	558.0	543.0
1335	1	1319	1.5	1.94	620.0	660.0	445.0	660.0	2.5	24.0 ± 2.2	459.6	463.3	462.1	485.0	511.0
1341	1	2546	0.9	2.36	70.0	100.0	232.0	310.0	5.2	95.7 ± 5.8	250.8	247.8	251.2	266.6	268.0
1343	1	9518	2.1	2.14	850.0	950.0	218.0	325.0	6.9	264.8 ± 11.0	232.1	226.2	231.9	266.0	270.0
1350	1	2043	1.8	1.30	480.0	515.0	623.0	669.0	28.4	62.8 ± 5.1	637.9	630.9	638.8	645.0	648.0
1354	1	6565	5.0	1.61	500.0	560.0	60.0	500.0	8.5	36.7 ± 3.4	199.8	205.6	212.5	265.0	326.0
1374	1	3333	55.1	1.54	1070.0	1140.0	184.0	675.0	0.9	25.4 ± 2.3	202.7	194.2	201.1	287.0	305.0
1380	1	2047	0.2	2.14	620.0	650.0	763.0	784.0	10.1	158.4 ± 6.8	774.5	772.2	774.5	782.0	776.0
1384	1	2557	2.2	1.23	540.0	560.0	175.0	324.0	9.0	39.1 ± 4.1	189.8	192.0	194.2	230.0	221.0
1384	2	2002	0.8	1.42	540.0	560.0	669.0	723.0	9.0	58.2 ± 4.9	683.5	678.7	682.2	706.0	693.0
1384	3	2525	0.7	1.36	540.0	560.0	860.0	906.0	9.0	103.3 ± 6.4	871.9	871.4	871.4	889.0	885.0
1409	1	1038	0.7	2.12	1098.0	1140.0	173.0	272.0	2.5	43.4 ± 3.0	191.3	194.2	190.8	204.0	207.0
1410	1	6931	24.6	1.74	0.0	26.0	48.0	557.0	1.2	84.8 ± 4.1	65.7	57.4	63.1	170.0	102.0
1412	1	822	0.5	1.22	904.0	940.0	418.0	478.0	5.0	23.6 ± 2.2	431.0	426.8	431.4	445.0	467.0
1429	1	2315	2.7	1.26	290.0	320.0	640.0	950.0	3.9	19.2 ± 2.0	676.5	690.1	684.4	740.0	727.0
1433	1	2485	17.3	1.43	1070.0	1110.0	30.7	190.0	2.1	50.4 ± 3.2	65.7	58.6	71.1	96.3	95.7
1433	2	939	25.9	1.35	1070.0	1110.0	458.0	696.0	2.1	12.4 ± 1.7	493.8	497.5	492.9	529.0	560.0
1443	1	3629	2.0	1.52	215.0	270.0	967.0	1140.0	4.5	217.3 ± 11.1	980.1	977.4	979.7	990.0	982.0
1444	1	685	0.2	1.81	48.0	100.0	299.0	318.0	2.8	60.6 ± 3.6	306.5	310.5	306.0	318.0	312.0
1444	2	1491	1.2	1.70	48.0	100.0	402.0	494.0	2.8	60.4 ± 3.6	409.5	420.0	409.7	443.0	436.0
1444	3	1180	0.8	1.97	48.0	100.0	944.0	1002.0	3.0	47.2 ± 3.1	956.3	974.0	956.9	972.0	975.0
1449	1	2584	8.1	1.70	1070.0	1140.0	697.0	872.0	2.5	94.3 ± 4.3	727.9	728.9	726.6	747.0	790.0
1462	1	3284	2.3	1.89	1080.0	1140.0	770.0	787.0	8.6	464.5 ± 19.0	780.6	779.1	779.1	784.0	784.0
1463	1	1133	3.6	1.26	660.0	752.0	173.0	270.0	6.7	24.0 ± 2.2	191.3	180.6	193.1	203.0	217.0
1463	2	459	0.9	1.29	660.0	752.0	400.0	424.0	6.4	42.8 ± 4.0	409.1	409.7	409.7	416.0	421.0
1463	3	1523	3.2	1.21	660.0	752.0	458.0	546.0	6.6	33.9 ± 3.4	471.2	473.5	471.3	486.0	487.6
1463	4	1015	4.0	1.24	660.0	752.0	847.0	956.0	6.7	17.4 ± 1.9	859.2	861.1	858.9	873.0	887.0

Table 1—Continued

Source	FlareNo	NCf (cnts)	Bgf (cnts)	MEf (keV)	t_{char1} (ks)	t_{char2} (ks)	t_{flare1} (ks)	t_{flare2} (ks)	CR _{char} (cnts/ks)	CR _{flare,pk} (cnts/ks)	$t_{CR,pk}$ (ks)	$t_{T,pk}$ (ks)	$t_{EM,pk}$ (ks)	t_{exp} (ks)	t_{sep} (ks)
(1)	(2)	(3)	(4)	(5)	(6)	(7)	(8)	(9)	(10)	(11)	(12)	(13)	(14)	(15)	(16)
1466	1	1912	1.7	1.63	715.0	750.0	954.0	1118.0	1.4	39.8 ± 2.8	984.8	985.4	978.6	1079.0	1010.0
1473	1	1901	0.9	1.47	80.0	100.0	269.0	318.0	19.2	68.2 ± 5.3	286.8	286.6	287.7	294.0	293.0
1479	1	971	8.6	1.25	156.0	181.0	179.0	272.0	3.0	21.8 ± 2.2	214.1	210.2	217.0	233.0	241.5
1481	1	1042	6.6	1.15	50.0	90.0	208.0	318.0	3.7	20.9 ± 2.1	236.9	239.8	236.4	262.0	300.0
1487	1	964	5.8	1.37	1070.0	1120.0	441.0	540.0	2.9	25.2 ± 2.3	459.6	459.9	457.6	474.0	517.0
1487	2	1178	8.6	1.38	1070.0	1120.0	630.0	776.0	2.9	17.9 ± 2.0	676.5	668.5	671.9	697.0	742.0
1489	1	2163	20.9	1.29	0.0	30.0	313.0	470.0	12.2	38.5 ± 3.7	386.3	392.6	391.5	415.0	432.0
1492	1	490	0.6	1.38	425.0	540.0	20.8	55.0	5.9	30.7 ± 3.3	42.0	40.3	43.8	49.0	51.0
1492	2	774	1.1	1.32	425.0	540.0	716.0	780.0	6.0	20.1 ± 2.1	733.6	728.9	736.9	760.0	763.0
1499	1	1226	2.4	1.61	240.0	300.0	304.0	323.0	1.1	286.0 ± 12.7	308.7	306.0	308.2	313.0	312.0
1499	2	2563	18.7	1.81	240.0	300.0	414.0	560.0	1.1	35.5 ± 4.5	452.7	454.2	484.9	522.0	506.0
1516	1	461	1.9	1.17	720.0	750.0	644.0	680.0	5.5	47.9 ± 3.8	658.4	658.2	658.2	662.0	660.0
1521	1	2662	3.7	1.36	635.0	665.0	840.0	975.0	6.7	30.6 ± 3.1	862.1	862.3	854.3	897.0	885.5
1568	1	39195	56.4	1.41	690.0	720.0	740.0	980.0	59.6	2029.3 ± 38.7	747.0	743.7	747.1	768.0	756.0
1570	1	1538	27.2	1.53	970.0	1002.0	236.0	513.0	0.9	15.0 ± 2.4	385.4	300.3	385.8	422.0	463.0
1595	1	692	4.0	1.09	722.0	762.0	13.5	89.0	5.9	15.1 ± 1.8	37.1	44.9	40.3	51.0	58.0
1603	1	857	8.4	2.26	629.0	715.0	921.0	992.0	2.3	21.7 ± 2.1	939.1	927.3	954.6	959.0	973.0
1608	1	3808	48.6	1.47	167.0	222.0	425.0	631.0	3.2	49.9 ± 3.2	459.6	449.6	461.0	522.0	550.0
1608	2	714	11.6	1.35	167.0	222.0	647.0	696.0	3.2	39.0 ± 2.8	659.4	655.9	659.4	672.0	664.5
1608	3	1297	43.2	1.32	167.0	222.0	911.0	1094.0	3.2	20.6 ± 2.1	956.3	951.2	964.9	1009.0	980.0

Note. — Column 1: COUP source number from Getman et al. (2005a). Column 2: Flare number. Columns 3-5: Estimated net flare counts, background counts during the flare, and median X-ray energy of flare counts. Columns 6-7: Start and stop times for measurement of the “characteristic” state. All times are measured from the start time of the COUP observation. Columns 8-9: Observed start and stop times of the flare. Column 10: Median count rate of the “characteristic” state. Column 11: Observed flare peak count rate. Columns 12-14: Time points when flare count rate, plasma temperature, and emission measure have maximum values. Column 15: Time point until which the lightcurve exhibits a pure exponential decay. Column 16: Separation time point between two distinct decay phases. This is relevant for cases with double slope decays (see Flag₁ from Table 2).

Table 2. Flare properties 2

Source	FlareNo	τ_r (ks)	τ_{d1} (ks)	τ_{d2} (ks)	$\log L_{X,pk}$ (erg s $^{-1}$)	T $_{obs,pk}$ (MK)	E M_{pk} (10 53 cm $^{-3}$)	T $_{EM,pk}$ (MK)	ζ_1	ζ_2	ζ_3	L $_1$ (10 10 cm)	L $_2$ (10 10 cm)	L $_{lim}$ (10 10 cm)	Flag $_1$	Type
(1)	(2)	(3)	(4)	(5)	(6)	(7)	(8)	(9)	(10)	(11)	(12)	(13)	(14)	(15)	(16)	(17)
7	1	13.5	13.0	13.0	31.62	40.62	40.37	27.85	0.6	1.3	-1.1	12.97	12.97	26.89	02	typ
9	1	10.0	19.2	19.5	32.18	103.28	117.11	32.49	-0.1	-0.6	0.4	44.06	44	inc
11	1	3.4	6.5	8.7	31.84	696.29	47.67	696.29	2.7	0.0	6.2	55.03	74.06	124.41	01	stp
23	1	2.4	5.5	14.9	31.98	60.34	72.48	54.54	1.2	8.4	0.6	4.15	21.22	45.93	13	typ
27	1	15.4	27.9	22.0	30.57	40.62	3.32	31.33	2.3	2.5	0.5	28.24	35.81	61.87	01	inc
27	2	21.0	70.6	123.3	30.69	33.65	4.87	26.69	0.6	-0.0	0.6	42.79	74.71	248.25	01	stp
28	1	208.4	30.9	40.8	32.05	67.31	86.29	41.78	0.5	0.7	-2.9	25.03	33.07	107.57	02	inc
43	1	50.6	55.5	55.0	31.18	59.18	11.96	41.78	1.4	4.2	0.8	50.72	51.20	146.19	03	srf
57	1	7.4	31.7	52.2	31.10	52.22	10.51	33.65	1.3	2.8	1.6	35.78	58.98	120.77	01	dbl
57	2	17.8	...	22.5	30.91	27.85	8.42	22.05	0.3	0.5	0.8	0.39	0.39	40.39	01	oth
62	1	117.0	232.0	197.6	30.94	62.67	7.83	23.21	0.3	0.4	-0.5	429.47	44	oth
62	2	18.4	39.0	41.6	30.77	94.00	3.92	48.74	2.0	10.3	1.9	62.54	66.79	120.30	03	typ
66	1	52.2	49.8	76.9	31.03	568.64	8.13	568.64	2.8	2.1	1.6	332.26	512.68	970.41	03	dbl
67	1	5.4	14.7	23.4	31.00	47.58	8.77	34.81	1.0	1.8	0.0	14.63	30.11	55.14	12	typ
71	1	12.2	11.5	107.6	30.94	35.97	7.91	35.97	1.0	1.9	0.5	5.71	108.37	259.18	13	stp
90	1	17.9	26.2	28.9	32.35	132.29	173.57	49.90	0.6	1.5	0.3	39.86	43.99	84.81	02	inc
101	1	...	24.5	47.9	31.95	53.38	69.92	44.10	0.6	0.7	0.6	16.95	33.14	130.22	01	inc
107	1	18.8	29.5	39.1	32.17	48.74	117.97	48.74	1.1	2.9	0.5	18.93	51.81	112.86	13	typ
108	1	8.6	26.4	45.0	31.30	140.42	13.52	39.46	1.3	1.3	-4.9	32.99	56.32	114.62	01	typ
108	2	10.0	11.9	24.4	31.35	48.74	19.96	27.85	0.7	0.3	-0.3	50.47	44	oth
112	1	83.0	87.5	116.3	30.99	29.01	10.83	20.89	0.4	1.0	0.5	26.93	84.79	202.03	23	typ
113	1	648.0	86.1	90.9	30.88	20.89	8.61	18.57	1.1	1.4	1.0	62.51	65.99	147.18	01	srf
113	2	280.2	98.4	334.7	30.97	25.53	10.20	22.05	1.1	1.2	1.1	78.39	266.69	600.75	01	oth
115	1	3.8	4.5	5.2	31.38	35.97	22.52	31.33	1.1	-8.3	1.6	5.15	6.02	11.56	03	typ
122	1	14.3	38.8	46.3	31.17	40.62	13.89	26.69	1.0	-2.1	1.8	42.29	50.40	93.18	03	typ
123	1	5.0	56.5	51.3	31.68	49.90	46.69	26.69	0.8	1.0	-0.3	113.77	44	dbl
123	2	8.4	15.0	29.9	31.89	45.26	64.08	45.26	1.5	1.5	0.9	21.24	42.27	82.71	01	stp
124	1	6.9	24.4	39.8	31.73	38.30	49.88	31.33	0.7	0.9	0.0	17.80	29.03	88.22	01	stp
124	2	9.0	24.7	35.2	31.60	38.30	36.21	32.49	1.6	2.7	0.4	29.62	42.26	79.73	01	typ
131	1	30.0	86.2	86.8	31.36	53.38	19.20	40.62	0.5	1.1	0.1	224.69	44	inc
139	1	12.1	22.2	21.5	30.73	22.05	5.99	22.05	0.9	1.1	0.3	15.52	15.99	39.77	01	typ
139	2	29.7	27.5	35.2	30.54	25.53	3.82	22.05	0.9	0.3	1.2	20.43	26.13	63.22	01	typ
141	1	20.4	30.1	32.5	31.41	96.32	17.67	33.65	1.1	0.2	2.0	30.90	33.41	75.25	01	typ
141	2	6.0	29.7	30.5	31.05	31.33	10.36	31.33	1.4	0.5	0.7	32.69	33.64	67.66	01	typ
142	1	0.6	2.4	2.8	31.81	197.28	40.81	197.28	0.8	16.9	0.3	0.25	6.82	18.56	13	typ
142	2	58.9	35.8	51.4	30.76	52.22	5.68	26.69	0.7	1.1	0.5	22.86	46.61	103.57	12	dbl
150	1	10.0	23.1	103.4	30.89	56.86	6.15	42.94	1.0	4.3	1.0	26.24	117.66	276.86	01	stp
152	1	23.2	73.8	70.8	30.54	27.85	3.45	26.69	0.8	1.7	3.8	76.51	79.75	148.62	02	inc
152	2	8.5	25.6	80.4	30.83	69.63	5.03	49.90	1.2	1.6	-0.4	35.74	112.30	235.53	01	stp
160	1	2.0	5.4	12.0	32.48	156.66	191.35	128.81	1.2	1.3	0.0	13.31	29.78	62.28	01	typ
173	1	14.5	28.9	32.1	30.91	27.85	8.19	26.69	1.4	2.7	-3.5	34.83	38.61	64.61	02	oth
183	1	17.8	16.5	20.0	31.17	64.99	11.90	48.74	2.6	0.8	-1.4	17.85	34.23	57.72	12	typ
183	2	25.2	19.1	31.1	31.35	49.90	18.95	42.94	1.4	-0.1	0.8	83.36	44	typ
202	1	5.7	23.5	25.5	31.03	42.94	9.39	29.01	1.6	-1.9	3.0	26.05	28.26	54.04	01	inc
205	1	21.9	76.6	71.6	31.03	68.47	7.74	55.70	4.0	4.0	2.9	141.52	151.46	239.75	01	inc
205	2	19.1	22.4	65.0	31.24	46.42	14.92	32.49	0.6	3.1	0.4	6.70	89.89	147.24	23	typ
223	1	9.1	17.6	22.3	31.91	128.81	52.40	103.28	1.7	1.9	1.6	42.76	54.29	101.06	01	typ
223	2	18.1	42.8	37.0	31.53	117.21	21.80	117.21	2.4	6.9	2.7	105.96	122.62	209.23	01	stp
262	1	15.1	34.1	49.5	31.72	76.59	36.57	61.51	2.1	4.7	-0.8	64.28	105.72	164.30	12	typ

Table 2—Continued

Source	FlareNo	τ_r (ks)	τ_{d1} (ks)	τ_{d2} (ks)	$\log L_{X,pk}$ (erg s $^{-1}$)	T $_{obs,pk}$ (MK)	E M_{pk} (10 53 cm $^{-3}$)	T $_{EM,pk}$ (MK)	ζ_1	ζ_2	ζ_3	L $_1$ (10 10 cm)	L $_2$ (10 10 cm)	L $_{lim}$ (10 10 cm)	Flag $_1$	Type
(1)	(2)	(3)	(4)	(5)	(6)	(7)	(8)	(9)	(10)	(11)	(12)	(13)	(14)	(15)	(16)	(17)
270	1	25.4	21.4	23.1	30.59	23.21	4.39	19.73	0.2	0.9	0.5	14.51	15.69	38.86	02	srf
310	1	6.8	16.0	37.4	31.08	37.14	11.41	20.89	0.7	1.5	1.1	8.43	33.30	65.01	12	stp
323	1	7.2	24.0	25.0	31.54	82.39	24.63	58.02	1.2	-8.6	1.1	35.83	37.40	80.31	01	typ
325	1	5.7	14.3	15.6	30.85	38.30	6.06	38.30	1.3	2.9	-0.0	21.55	23.55	38.98	02	inc
325	2	9.4	7.7	9.0	30.99	38.30	8.45	37.14	1.1	1.1	-0.0	8.39	9.82	22.05	01	typ
325	3	36.1	25.4	33.1	30.57	45.26	3.42	25.53	0.4	2.7	0.1	5.71	38.63	64.83	12	srf
331	1	3.4	4.6	5.0	32.50	148.54	210.36	52.22	0.6	0.7	1.2	3.73	4.07	14.93	01	inc
331	2	14.4	22.5	49.7	31.48	684.68	21.09	429.38	10.1	11.6	-34.7	530.32	44	srf
332	1	86.0	181.8	154.5	31.35	48.74	20.73	32.49	0.4	0.9	0.1	15.69	169.03	411.76	12	oth
342	1	13.1	25.4	24.2	31.83	62.67	51.22	49.90	1.3	1.4	0.9	34.69	36.45	74.38	01	typ
343	1	19.3	37.8	61.0	31.61	138.10	26.15	103.28	2.8	17.0	1.9	103.04	166.42	276.62	01	typ
365	1	5.7	14.0	10.4	31.62	266.91	27.71	56.86	-0.3	0.9	-2.8	13.39	18.06	44.32	02	typ
382	1	20.5	38.2	45.3	30.58	38.30	3.72	22.05	1.3	-0.2	4.1	33.62	51.54	81.28	13	oth
382	2	8.4	29.2	30.5	30.49	31.33	3.38	22.05	0.8	0.2	1.1	18.91	19.72	54.71	01	oth
387	1	10.8	13.9	16.2	31.15	23.21	15.74	20.89	0.1	0.5	0.0	28.18	44	typ
394	1	38.8	24.6	98.7	31.79	19.73	69.16	19.73	0.9	1.1	4.3	16.71	67.09	165.66	01	inc
417	1	20.9	11.2	15.3	31.01	55.70	7.98	41.78	0.6	2.0	0.1	8.18	22.44	40.31	12	typ
431	1	...	58.0	112.6	31.40	23.21	27.50	20.89	0.6	0.9	-0.1	39.51	76.61	195.60	02	inc
449	1	8.6	34.6	97.8	31.47	95.16	21.78	59.18	0.6	2.2	-0.9	31.29	181.61	317.38	12	stp
452	1	6.1	22.6	36.5	31.24	88.20	13.90	23.21	0.0	-0.0	0.4	67.56	44	stp
454	1	11.9	20.5	26.1	31.60	77.75	31.18	46.42	0.8	1.0	0.3	21.68	27.57	73.25	01	typ
454	2	12.8	42.4	84.6	31.52	60.34	25.65	51.06	1.5	2.1	1.5	64.33	128.24	251.40	01	stp
459	1	3.6	10.0	18.2	31.55	61.51	27.29	51.06	0.8	1.5	2.3	11.38	27.86	54.11	12	typ
470	1	104.0	28.0	62.1	30.75	18.57	6.60	16.25	0.4	-0.9	0.8	5.26	33.71	92.82	13	inc
485	1	12.0	19.3	19.5	31.87	255.31	46.62	255.31	1.7	2.2	1.9	81.04	81.95	151.93	01	typ
490	1	5.3	7.1	17.5	31.46	49.90	22.54	48.74	1.2	0.9	1.3	9.57	23.68	50.42	01	typ
499	1	142.3	34.0	49.0	31.07	30.17	11.73	27.85	1.0	2.1	0.1	29.42	57.15	101.21	12	inc
515	1	25.6	94.2	95.9	31.07	38.30	11.04	32.49	1.2	1.0	0.9	99.94	101.78	217.34	01	inc
554	1	45.3	27.3	56.9	31.81	152.02	52.01	49.90	0.5	0.1	0.3	16.12	33.60	166.70	01	oth
554	2	44.0	40.5	29.7	31.83	154.34	45.21	69.63	1.1	1.5	0.5	49.04	66.81	144.95	01	srf
554	3	159.9	127.8	130.2	31.75	87.04	53.32	30.17	0.2	-2.1	-0.8	282.05	44	inc
561	1	9.9	14.8	29.7	31.95	261.11	56.56	181.03	1.2	1.1	1.0	43.90	88.15	188.69	01	typ
567	1	6.6	27.3	24.3	31.26	499.01	12.73	464.19	4.7	0.4	5.4	174.37	196.29	305.16	01	inc
567	2	12.8	19.5	43.2	30.95	35.97	7.73	34.81	1.3	1.7	1.3	22.54	49.97	102.06	01	stp
567	3	13.2	94.4	70.6	31.14	25.53	14.77	20.89	1.0	1.2	0.1	52.75	70.60	164.13	01	inc
570	1	97.0	79.0	87.1	31.64	68.47	33.68	46.42	1.8	-2.8	1.9	120.14	132.53	244.42	01	inc
579	1	5.5	11.6	15.2	31.69	206.57	30.85	194.96	0.6	3.1	-0.9	18.72	61.53	100.75	12	typ
597	1	81.7	86.6	107.2	30.92	23.21	9.31	18.57	0.4	0.6	0.7	8.33	47.60	173.63	12	srf
600	1	40.5	83.6	177.1	30.45	29.01	3.21	17.41	2.8	3.4	4.5	275.86	44	oth
600	2	8.1	22.4	46.5	30.89	49.90	6.04	49.90	1.1	2.3	0.4	9.35	61.89	136.20	13	typ
626	1	13.0	36.9	72.0	31.34	80.07	15.42	68.47	1.8	2.9	-0.1	70.63	137.88	254.93	01	inc
634	1	96.9	34.7	51.3	30.77	475.80	4.02	475.80	3.0	12.7	2.0	239.16	353.83	581.82	01	inc
645	1	47.3	18.1	46.7	31.04	69.63	12.48	19.73	-1.4	-1.6	-1.3	78.44	44	srf
645	2	15.8	62.5	92.0	31.23	59.18	15.23	35.97	2.7	0.3	2.6	89.71	131.90	221.42	01	stp
648	1	163.9	279.5	279.5	31.20	47.58	15.12	27.85	0.9	-0.3	0.3	577.27	44	inc
649	1	36.6	29.1	61.3	31.57	123.01	24.52	81.23	0.5	1.5	0.4	22.17	122.56	240.60	12	dbl
669	1	40.3	59.3	64.8	31.63	106.76	28.44	81.23	1.6	2.9	1.0	122.94	134.27	254.22	01	inc
670	1	11.9	13.4	68.0	31.61	62.67	30.94	54.54	2.7	1.6	3.3	24.67	125.51	210.08	01	stp
670	2	20.4	52.6	63.5	31.53	73.11	26.11	54.54	-0.0	-3.8	-3.5	196.39	44	inc

Table 2—Continued

Source	FlareNo	τ_r (ks)	τ_{d1} (ks)	τ_{d2} (ks)	$\log L_{X,pk}$ (erg s $^{-1}$)	T $_{obs,pk}$ (MK)	E M_{pk} (10 53 cm $^{-3}$)	T $_{EM,pk}$ (MK)	ζ_1	ζ_2	ζ_3	L $_1$ (10 10 cm)	L $_2$ (10 10 cm)	L $_{lim}$ (10 10 cm)	Flag $_1$	Type
(1)	(2)	(3)	(4)	(5)	(6)	(7)	(8)	(9)	(10)	(11)	(12)	(13)	(14)	(15)	(16)	(17)
682	1	3.6	12.0	14.1	31.98	499.01	65.40	499.01	2.7	0.0	3.7	87.63	103.18	164.98	03	typ
682	2	6.5	12.8	19.1	31.26	126.49	11.85	111.41	1.2	1.2	-2.4	28.75	42.95	90.46	01	typ
682	3	12.2	24.2	25.2	31.17	160.15	9.37	126.49	1.2	1.5	1.6	57.52	59.88	129.02	01	typ
682	4	10.7	9.1	18.7	31.21	499.01	11.34	499.01	3.2	1.9	6.5	65.34	133.90	218.05	01	typ
689	1	13.4	85.0	70.7	32.23	23.21	196.53	17.41	0.6	0.9	-0.6	32.14	51.49	132.33	12	srf
707	1	15.3	38.9	42.4	30.98	41.78	10.02	25.53	0.5	-0.5	2.4	83.15	44	typ
707	2	17.9	17.3	43.7	31.04	46.42	8.79	46.42	0.8	5.3	0.4	7.14	45.38	122.69	13	typ
718	1	27.2	62.6	68.1	31.40	78.91	18.27	32.49	-0.3	-1.3	-3.8	154.24	44	inc
720	1	63.6	99.8	110.7	31.46	45.26	26.91	33.65	0.5	-0.4	1.5	256.08	44	oth
737	1	7.1	55.5	75.0	31.31	684.68	15.44	638.26	2.4	8.6	0.8	436.65	589.54	1013.89	01	stp
752	1	14.8	57.7	70.3	32.37	134.62	184.66	42.94	0.6	0.8	0.6	39.17	47.69	188.16	01	typ
753	1	1.8	9.0	18.6	31.58	295.92	24.63	266.91	1.6	22.1	1.5	38.21	78.95	148.73	01	typ
761	1	4.7	7.1	8.0	31.64	88.20	29.37	81.23	1.2	5.3	0.9	12.96	14.43	31.21	01	typ
794	1	21.1	20.5	16.4	30.96	76.59	8.04	33.65	1.0	2.0	2.1	15.81	19.78	47.35	01	oth
801	1	121.5	79.4	96.9	31.51	183.36	22.78	44.10	3.0	-6.4	-6.7	263.70	44	oth
828	1	76.8	94.4	113.2	31.51	429.38	21.83	38.30	0.1	-6.0	-1.3	282.91	44	srf
828	2	4.6	20.2	24.3	31.80	696.29	43.64	696.29	3.1	10.4	0.6	69.47	235.29	346.49	23	typ
848	1	44.2	41.1	34.7	31.67	145.06	29.26	145.06	1.6	7.1	0.9	75.27	152.16	228.72	23	inc
867	1	4.5	6.7	6.5	31.75	284.32	35.48	164.79	2.7	4.2	-0.0	23.21	23.97	40.23	01	typ
871	1	5.2	14.5	14.6	31.05	61.51	9.38	33.65	1.0	1.0	-0.0	14.61	14.70	33.82	01	typ
874	1	22.1	47.3	48.6	32.23	545.43	109.89	545.43	2.3	1.8	2.2	337.59	346.59	597.84	01	stp
881	1	22.8	48.2	86.3	32.51	26.69	378.71	17.41	0.2	0.3	0.4	134.50	44	typ
891	1	13.9	14.2	22.4	32.61	394.56	256.22	170.59	1.0	4.8	0.8	36.07	56.99	137.04	01	typ
891	2	7.6	51.8	87.6	32.70	278.52	314.44	158.99	1.0	0.3	-0.0	131.36	222.11	514.43	01	typ
894	1	6.2	9.1	36.8	31.33	255.31	16.30	24.37	-0.7	-1.2	-2.6	70.06	44	stp
894	2	10.4	26.4	22.0	31.69	261.11	30.67	208.89	0.9	1.9	-0.2	61.38	73.67	182.81	01	typ
894	3	15.5	16.3	28.9	31.15	162.47	10.07	61.51	0.2	-1.2	0.8	95.91	44	oth
915	1	9.7	46.4	61.0	32.45	499.01	215.74	499.01	0.1	-1.7	0.1	711.46	44	inc
932	1	20.7	20.9	20.4	32.77	19.73	676.20	18.57	0.3	0.7	0.0	10.72	10.94	33.79	02	typ
942	1	21.1	30.7	45.5	31.38	39.46	22.11	33.65	2.0	0.7	0.7	24.74	58.87	105.26	12	oth
942	2	7.0	23.2	28.6	31.87	142.74	46.26	111.41	1.6	6.2	1.1	57.74	71.19	135.52	01	typ
960	1	0.8	7.4	10.7	31.96	38.30	83.16	31.33	0.4	0.1	0.8	2.12	8.49	23.61	13	typ
971	1	9.2	21.1	21.0	32.01	80.07	79.22	37.14	0.7	1.9	0.4	16.43	16.57	51.91	01	typ
976	1	20.7	22.3	23.8	31.60	499.01	26.73	499.01	1.6	16.5	1.4	135.83	144.91	277.53	01	typ
976	2	11.9	62.7	49.7	30.89	84.72	6.18	37.14	1.2	0.1	1.3	57.86	72.98	153.77	01	dbl
982	1	19.2	14.7	16.9	31.21	133.46	10.61	102.12	5.1	6.9	0.4	42.82	49.34	76.07	01	oth
982	2	44.5	39.3	49.9	31.49	626.66	20.82	626.66	2.1	31.3	1.9	298.52	379.35	667.89	01	dbl
985	1	19.8	11.5	24.1	31.53	106.76	22.27	85.88	7.9	13.4	5.4	31.27	65.46	97.76	01	oth
985	2	8.5	15.0	17.0	31.61	46.42	37.97	33.65	1.7	0.7	0.9	18.57	21.00	39.29	01	typ
993	1	11.1	47.3	54.2	31.01	83.55	8.37	35.97	0.3	-1.6	2.4	130.50	44	oth
997	1	17.2	69.0	61.0	31.54	148.54	23.61	63.83	2.4	2.8	2.1	121.29	137.28	234.42	01	stp
1028	1	8.6	13.2	21.0	31.55	60.34	28.26	45.26	0.9	0.8	-0.9	14.39	22.89	58.10	01	typ
1040	1	3.5	13.7	13.0	32.61	167.11	273.75	84.72	0.4	1.1	0.5	7.25	25.44	55.28	12	typ
1044	1	14.5	30.6	43.0	30.77	47.58	5.31	27.85	1.0	1.8	0.2	26.48	37.22	88.77	01	stp
1045	1	7.4	19.2	19.6	31.27	156.66	12.17	87.04	1.1	2.8	-1.6	47.19	48.09	80.18	02	typ
1070	1	2.4	13.7	18.6	31.45	615.05	19.13	342.34	2.9	1.8	4.3	77.22	105.04	173.41	01	typ
1080	1	8.3	15.7	13.8	32.14	55.70	108.77	37.14	0.6	0.1	0.7	8.72	9.95	38.55	01	typ
1083	1	53.2	278.3	354.3	31.28	89.36	15.92	26.69	0.7	0.8	0.6	192.61	245.21	713.35	01	inc
1090	1	59.6	29.7	48.0	31.97	33.65	91.37	27.85	1.0	3.6	-0.3	38.24	61.73	99.06	02	srf

Table 2—Continued

Source	FlareNo	τ_r (ks)	τ_{d1} (ks)	τ_{d2} (ks)	$\log L_{X,pk}$ (erg s $^{-1}$)	T $_{obs,pk}$ (MK)	E M_{pk} (10 53 cm $^{-3}$)	T $_{EM,pk}$ (MK)	ζ_1	ζ_2	ζ_3	L $_1$ (10 10 cm)	L $_2$ (10 10 cm)	L $_{lim}$ (10 10 cm)	Flag $_1$	Type
(1)	(2)	(3)	(4)	(5)	(6)	(7)	(8)	(9)	(10)	(11)	(12)	(13)	(14)	(15)	(16)	(17)
1090	2	125.6	174.7	266.6	31.84	27.85	81.36	16.25	0.2	-3.0	0.2	398.39	44	srf
1096	1	15.4	21.5	21.7	31.92	359.75	54.40	359.75	1.3	31.6	0.9	208.44	44	inc
1114	1	20.0	34.2	65.4	32.01	178.71	65.00	114.89	1.1	1.8	-1.1	89.75	171.57	316.24	02	stp
1127	1	7.4	10.7	11.7	31.58	59.18	28.89	44.10	1.1	1.6	1.0	12.86	14.06	31.72	01	typ
1134	1	94.4	69.1	61.6	30.68	44.10	4.28	20.89	0.4	1.0	-0.1	11.95	51.88	120.09	12	srf
1140	1	25.3	24.3	34.2	31.56	76.59	25.55	63.83	1.3	2.1	-0.5	46.49	65.55	116.17	02	oth
1149	1	5.8	12.7	23.0	31.14	111.41	9.85	52.22	2.2	2.6	2.0	21.75	39.49	69.24	01	stp
1149	2	39.8	58.6	63.0	30.88	46.42	6.07	46.42	2.9	1.8	2.7	99.16	106.56	176.74	01	srf
1151	1	9.7	9.0	10.7	31.38	53.38	20.44	37.14	1.4	2.2	-0.7	11.06	13.20	26.28	01	typ
1158	1	9.1	12.8	11.4	31.29	661.47	12.60	88.20	0.4	3.2	-1.5	28.71	32.47	52.98	02	typ
1158	2	4.4	7.8	13.1	31.19	615.05	10.85	615.05	3.6	5.2	1.8	64.33	108.08	172.92	01	typ
1158	3	18.9	25.2	27.7	31.27	66.15	14.35	55.70	0.6	1.8	-0.2	42.96	47.21	86.62	02	typ
1161	1	19.0	68.1	71.8	31.19	45.26	13.46	33.65	-0.6	-4.8	0.6	166.22	44	oth
1165	1	13.6	13.1	21.6	31.89	119.53	64.03	40.62	-0.0	-0.4	-0.4	55.93	44	oth
1178	1	3.9	12.5	10.8	31.33	58.02	16.13	58.02	0.2	1.2	0.6	15.98	18.53	40.07	02	typ
1236	1	2.4	8.1	7.7	31.49	45.26	25.73	41.78	0.3	0.0	1.7	0.84	11.44	21.25	13	typ
1246	1	6.5	23.3	22.6	31.90	649.87	55.59	56.86	0.7	0.9	-2.5	23.85	24.62	73.97	01	stp
1248	1	29.1	35.7	49.0	31.09	24.37	12.94	23.21	1.1	2.1	1.2	29.27	40.17	90.69	01	srf
1252	1	6.2	22.4	37.2	31.68	62.67	37.59	44.10	1.0	-9.4	1.0	101.18	44	inc
1261	1	22.0	16.8	45.1	30.71	145.06	4.36	39.46	1.8	-3.4	1.7	114.75	44	stp
1268	1	70.6	87.4	99.4	31.11	140.42	8.26	104.44	6.6	-2.6	8.6	453.61	44	srf
1309	1	9.3	14.1	42.9	31.33	188.00	13.51	188.00	4.6	2.6	4.4	58.64	179.06	278.78	01	stp
1311	1	13.2	43.3	82.6	30.67	24.37	5.13	23.21	0.5	10.2	0.5	152.94	44	inc
1335	1	11.0	51.0	60.9	31.19	83.55	10.70	68.47	0.4	0.3	1.0	19.57	90.38	215.61	13	stp
1341	1	7.4	19.2	22.4	31.88	194.96	54.83	55.70	0.8	3.6	0.1	21.66	43.67	69.99	12	typ
1343	1	16.0	24.0	30.1	32.25	615.05	111.73	225.13	1.7	1.8	3.2	93.00	116.80	218.10	01	stp
1350	1	19.7	32.8	46.9	31.25	26.69	19.90	19.73	0.4	1.1	0.6	78.81	44	inc
1354	1	118.6	145.8	215.3	31.20	63.83	12.75	42.94	1.1	1.5	2.1	576.42	44	oth
1374	1	99.7	126.0	150.6	31.03	33.65	9.80	32.49	0.1	0.0	0.3	341.07	44	inc
1380	1	7.1	23.5	17.9	31.96	638.26	68.24	638.26	3.1	7.9	2.8	148.13	194.50	317.64	01	inc
1384	1	10.3	47.5	71.6	30.93	31.33	8.09	31.33	1.0	2.9	-0.1	63.75	96.12	158.75	02	typ
1384	2	36.1	32.8	32.1	31.22	67.31	12.13	58.02	2.2	1.8	2.9	59.27	60.66	105.37	01	srf
1384	3	7.5	28.0	25.6	31.44	49.90	21.68	49.90	1.5	3.6	1.4	38.84	42.48	82.08	01	stp
1409	1	6.2	13.7	20.2	31.44	98.64	19.07	70.79	1.0	0.2	2.0	21.25	40.79	73.05	13	typ
1410	1	9.6	61.2	122.2	31.76	107.92	37.86	98.64	0.9	1.2	0.6	103.86	207.46	538.77	01	typ
1412	1	9.7	27.5	42.2	30.81	31.33	6.38	29.01	1.3	1.4	4.3	28.09	43.03	89.21	01	typ
1429	1	31.6	116.6	146.9	30.68	39.46	4.30	30.17	0.9	4.8	0.3	3.49	130.89	318.35	13	typ
1433	1	35.4	47.0	43.6	31.28	76.59	16.28	22.05	0.3	1.4	0.3	2.28	42.47	84.31	12	typ
1433	2	28.5	57.9	93.9	30.58	24.37	4.22	22.05	0.3	1.0	-3.8	168.61	44	oth
1443	1	3.8	5.2	31.6	31.91	591.84	53.62	295.92	1.9	7.7	1.9	24.27	148.47	269.23	01	stp
1444	1	3.1	13.9	13.9	31.50	176.39	20.71	92.84	1.3	-1.0	2.2	28.43	28.43	59.25	01	inc
1444	2	1.6	26.0	23.6	31.50	661.47	20.82	94.00	0.7	4.8	-0.9	65.20	71.72	111.24	02	stp
1444	3	8.8	25.8	21.4	31.38	661.47	16.35	475.80	0.3	-2.0	9.6	292.59	44	dbl
1449	1	7.8	14.4	25.4	31.71	211.21	32.80	181.03	1.0	3.1	0.1	55.96	98.38	161.26	02	stp
1462	1	3.5	9.0	7.3	32.92	696.29	629.91	696.29	5.2	6.3	-4.4	67.91	83.48	128.58	01	inc
1463	1	18.9	25.2	44.2	30.79	41.78	5.93	25.53	0.7	-0.5	1.8	16.27	47.33	86.55	13	stp
1463	2	5.1	5.9	8.5	31.02	38.30	9.06	38.30	1.1	1.3	0.0	6.61	9.55	21.13	01	typ
1463	3	10.2	32.6	50.5	31.03	67.31	8.63	32.49	2.1	4.0	1.1	41.67	64.60	114.43	01	stp
1463	4	18.7	36.0	65.9	30.72	78.91	3.59	75.43	3.6	7.2	0.8	51.47	154.38	247.51	13	stp

Table 2—Continued

Source (1)	FlareNo (2)	τ_r (ks) (3)	τ_{d1} (ks) (4)	τ_{d2} (ks) (5)	$\log L_{X,pk}$ (erg s $^{-1}$) (6)	T $_{obs,pk}$ (MK) (7)	EM $_{pk}$ (10 53 cm $^{-3}$) (8)	T $_{EM,pk}$ (MK) (9)	ζ_1 (10)	ζ_2 (11)	ζ_3 (12)	L $_1$ (10 10 cm) (13)	L $_2$ (10 10 cm) (14)	L $_{lim}$ (10 10 cm) (15)	Flag $_1$ (16)	Type (17)
1466	1	22.3	125.8	87.8	31.28	54.54	17.45	25.53	0.5	-5.5	-0.5	246.67	44	inc
1473	1	13.0	11.7	28.4	31.42	77.75	18.60	44.10	1.6	1.6	0.2	77.30	44	stp
1479	1	16.8	32.8	40.2	30.71	42.94	4.73	27.85	1.2	1.9	0.2	31.44	38.56	82.99	01	typ
1481	1	11.2	43.8	52.6	30.66	26.69	4.95	20.89	0.9	1.0	0.2	30.11	36.11	91.36	01	stp
1487	1	23.6	14.4	31.5	30.93	30.17	8.87	24.37	0.8	0.8	-0.0	10.30	22.58	60.00	01	typ
1487	2	31.8	30.7	52.1	30.76	30.17	5.62	30.17	1.1	1.6	-0.5	29.87	50.65	112.82	01	stp
1489	1	59.1	58.4	82.2	30.99	27.85	10.27	23.21	1.3	0.4	1.4	53.37	75.04	152.13	01	inc
1492	1	12.1	7.2	8.3	30.92	51.06	7.79	29.01	1.0	0.9	13.6	6.33	7.29	17.46	01	srf
1492	2	16.1	64.7	44.0	30.78	49.90	5.30	25.53	0.6	0.7	1.6	29.18	67.06	126.79	23	srf
1499	1	0.8	3.0	3.2	32.19	49.90	132.64	39.46	0.2	1.6	-0.1	4.05	4.28	8.17	02	typ
1499	2	25.7	77.0	70.9	31.19	148.54	11.25	49.90	1.7	3.0	1.9	111.16	120.81	225.78	01	srf
1516	1	4.8	4.2	6.4	31.12	48.74	10.32	48.74	1.3	0.0	1.0	5.84	8.98	18.63	01	typ
1521	1	99.3	80.2	109.8	30.91	37.14	7.44	27.85	1.6	3.7	1.0	87.30	119.60	226.79	01	inc
1568	1	5.9	9.8	33.7	32.92	545.43	622.12	545.43	1.4	2.8	1.3	60.82	209.35	415.23	01	typ
1570	1	91.8	121.4	118.2	30.77	44.10	5.92	23.21	1.3	0.9	-0.7	105.23	108.07	224.67	01	inc
1595	1	20.5	38.6	54.1	30.53	26.69	3.75	20.89	1.5	2.2	-0.0	34.79	48.72	94.02	01	oth
1603	1	15.1	46.9	41.1	31.30	52.22	18.04	23.21	-0.2	-0.3	0.6	86.88	44	typ
1608	1	25.8	76.4	79.6	31.29	161.31	15.81	33.65	1.0	1.4	0.4	74.16	77.21	184.12	01	stp
1608	2	8.0	10.7	13.0	31.09	37.14	12.35	25.53	0.5	3.0	0.4	4.04	4.89	25.44	01	typ
1608	3	25.9	80.5	80.7	30.78	24.37	6.50	24.37	1.3	2.0	-0.0	153.87	44	inc

Note. — Column 1: COUP source number from Getman et al. (2005a). Column 2: Flare number. Column 3: Rise e-folding timescale. Columns 4–5: Decay e-folding timescales: τ_{d1} is measured within the time interval $[t_{CR,pk} - t_{exp}]$, and τ_{d2} is measured within the time interval $[t_{CR,pk} - t_{flare2}]$ (see Notes to Table 1 for the description of t_{flare2} , $t_{CR,pk}$ and t_{exp}). Column 6: Flare peak X-ray luminosity. Column 7: Flare peak observed plasma temperature. Column 8: Flare peak emission measure. Column 9: Observed plasma temperature at the time point when the emission measure has maximum value EM $_{pk}$. Columns 10–12: Inferred slopes of the trajectory in the log T – log(EM) $^{1/2}$ diagram: ζ_1 is the average slope derived over the full $[t_{EM,pk} - t_{flare2}]$ decay time interval; ζ_2 is the slope derived within the $[t_{EM,pk} - t_{sep}]$ interval; ζ_3 is the slope derived within the $[t_{sep} - t_{flare2}]$ interval (see Notes to Table 1 for the description of t_{flare2} , $t_{EM,pk}$ and t_{sep}). Columns 13–14: Inferred length range of the flaring structure [L $_1$ –L $_2$] obtained under the assumption of sustained heating using the combination of both decay timescales, τ_{d1} and τ_{d2} , and inferred slopes defined by Flag $_1$. Column 15: The limiting maximum loop length assuming the scaling law of Serio et al. (1991) for a freely decaying loop with no sustained heating. Column 16: Flag $_1$ defines the best or dominant (over most of the decay time) slope or a combination of possible slopes (generally for a double slope decay) which, in combination with decay timescales τ_{d1} and τ_{d2} , are used to estimate the range of flaring loop sizes: 01 = ζ_1 ; 02 = ζ_2 ; 03 = ζ_3 ; 12 = ζ_1, ζ_2 ; 13 = ζ_1, ζ_3 ; 23 = ζ_2, ζ_3 ; 44 = unable to estimate loop sizes. Column 17: Flare morphological classification: typ= typical; stp= flare with step decay; srf= slow-rise-and/or-top-flat; dbl= double flare; inc= incomplete; oth= other.

Table 3. Time-Resolved Spectroscopy Analysis

Source (1)	FlareNo (2)	Type (3)	SegNum (4)	$< N >_{seg}$ (cnts) (5)	N _{char} (cnts) (6)	T _{char} (MK) (7)	T _{pk, TRS, noCH} (MK) (8)	T _{pk, TRS, CH} (MK) (9)	$\zeta_{TRS, noCH}$ (10)	$\zeta_{TRS, CH}$ (11)
7	1	typ	8	202	1458	12.69	37.11	37.48	1.14	0.95
9	1	inc	9	261	484	16.02	66.01	66.54	-0.10	-0.12
11	1	stp	6	152	194	12.21	927.22	927.22	2.13	2.09
23	1	typ	12	333	2090	16.16	53.72	54.10	1.15	0.99
27	1	inc	3	80	175	12.10	32.50	33.61	1.51	1.38
27	2	stp	11	130	175	12.10	45.83	50.22	0.67	-0.49
28	1	inc	22	586	381	15.76	59.45	59.48	0.69	0.67
43	1	srf	8	208	210	15.96	74.90	77.30	2.09	2.15
57	1	dbl	5	136	115	12.74	43.64	46.88	2.00	1.91
57	2	oth	3	76	115	12.74	29.60	61.54	-1.88	-2.89
62	1	oth	13	273	149	29.90	39.97	40.42	0.79	0.74
62	2	typ	4	172	149	29.90	68.25	71.53	2.15	1.87
66	1	dbl	5	160	155	11.29	77.00	77.97	1.24	1.16
67	1	typ	4	145	227	12.97	41.94	45.77	1.96	0.49
71	1	stp	9	276	113	10.95	43.10	46.87	1.89	0.56
90	1	inc	11	261	108	11.17	66.45	66.46	0.55	0.54
101	1	inc	21	462	34	11.61	67.90	67.93	0.53	0.44
107	1	typ	8	224	290	19.72	69.08	70.83	1.21	1.13
108	1	typ	6	222	339	20.10	78.83	80.04	0.77	0.54
108	2	oth	5	214	339	20.10	49.64	49.90	1.09	1.02
112	1	typ	12	213	362	19.22	23.65	23.67	0.70	0.78
113	1	srf	4	122	559	15.12	19.99	20.73	0.50	-0.58
113	2	oth	8	213	559	15.12	22.98	24.59	1.59	1.30
115	1	typ	3	74	182	15.15	122.33	129.24	1.89	1.84
122	1	typ	7	224	23	23.62	64.30	64.77	0.91	0.89
123	1	dbl	5	201	141	26.50	48.66	49.41	0.57	0.46
123	2	stp	5	171	141	26.50	52.59	52.83	1.87	1.81
124	1	stp	6	192	280	18.61	41.85	42.42	0.54	0.43
124	2	typ	4	187	280	18.61	41.86	42.25	2.29	2.19
131	1	inc	9	219	161	20.72	38.85	39.05	0.58	0.36
139	1	typ	4	134	211	12.24	30.01	30.48	1.19	1.11
139	2	typ	4	150	211	12.24	28.78	29.92	0.92	1.14
141	1	typ	9	215	454	12.87	136.18	138.10	1.43	1.36
141	2	typ	5	209	454	12.87	37.74	38.26	2.10	2.03
142	1	typ	4	148	146	11.94	163.59	163.76	1.37	1.32
142	2	dbl	5	195	146	11.94	32.79	33.54	1.17	1.03
150	1	stp	10	205	264	12.76	52.56	59.11	1.42	0.96
152	1	inc	4	170	226	12.44	28.19	29.74	1.21	0.91
152	2	stp	9	213	226	12.44	62.42	65.21	1.55	1.31
160	1	typ	14	219	36	20.20	883.72	884.02	1.97	1.97
173	1	oth	4	151	201	12.88	59.10	86.64	2.97	0.64
183	1	typ	3	130	115	18.19	60.04	77.10	2.19	1.32
183	2	typ	5	172	115	18.19	40.32	41.30	1.07	0.60
202	1	inc	4	173	126	12.82	42.97	44.76	0.37	0.25
205	1	inc	6	169	259	25.30	83.90	85.64	0.76	0.69
205	2	typ	7	223	259	25.30	31.30	31.34	0.89	0.88
223	1	typ	11	213	149	21.93	156.21	158.63	1.71	1.56
223	2	stp	7	204	149	21.93	96.13	101.47	1.78	1.59
262	1	typ	12	214	573	18.04	103.82	106.89	1.67	1.54

Table 3—Continued

Source	FlareNo	Type	SegNum	$< N >_{seg}$ (cnts)	N _{char} (cnts)	T _{char} (MK)	T _{pk, TRS, noCH} (MK)	T _{pk, TRS, CH} (MK)	$\zeta_{TRS, noCH}$	$\zeta_{TRS, CH}$
(1)	(2)	(3)	(4)	(5)	(6)	(7)	(8)	(9)	(10)	(11)
270	1	srf	4	80	175	12.60	15.75	15.82	0.26	0.20
310	1	stp	4	160	108	18.61	31.23	33.45	1.99	1.99
323	1	typ	6	212	212	17.77	66.26	66.62	1.23	0.99
325	1	inc	3	125	359	12.34	35.68	36.02	0.47	0.38
325	2	typ	3	104	359	12.34	730.19	726.45	3.82	3.52
325	3	srf	3	150	359	12.34	29.26	36.72	-0.67	-0.85
331	1	inc	7	204	39	18.72	110.14	110.18	1.08	1.08
331	2	srf	5	199	39	18.72	825.90	887.00	27.04	26.27
332	1	oth	10	210	49	28.65	48.16	48.23	0.73	1.32
342	1	typ	8	207	443	14.02	61.13	62.83	1.23	0.95
343	1	typ	13	392	2958	16.38	99.39	101.33	2.47	2.35
365	1	typ	4	125	109	31.22	146.46	149.17	0.78	0.51
382	1	oth	3	124	264	12.72	31.55	33.24	2.39	1.56
382	2	oth	3	91	264	12.72	33.50	35.12	2.03	-0.01
387	1	typ	4	192	1417	23.28	31.30	31.46	1.05	1.21
394	1	inc	4	191	112	12.76	24.05	26.57	1.41	1.77
417	1	typ	3	154	219	15.51	52.65	53.73	1.35	0.82
431	1	inc	13	425	1251	16.49	25.11	25.37	0.77	0.69
449	1	stp	11	219	163	25.45	60.58	114.85	0.53	-0.47
452	1	stp	4	160	93	20.83	68.57	76.18	-1.63	-0.89
454	1	typ	8	204	373	16.26	51.20	52.37	1.03	0.74
454	2	stp	11	325	373	16.26	55.21	58.42	1.31	0.90
459	1	typ	10	208	224	12.22	68.46	68.60	1.04	1.00
470	1	inc	6	207	161	11.64	25.11	33.79	1.52	1.25
485	1	typ	10	215	98	11.27	201.74	202.23	1.52	1.49
490	1	typ	4	188	188	15.94	49.03	85.24	0.89	-0.32
499	1	inc	6	189	130	16.56	31.56	34.82	0.93	0.78
515	1	inc	4	211	88	12.90	26.43	36.84	0.65	-0.18
554	1	oth	7	208	95	21.14	72.14	73.46	-0.20	-0.24
554	2	srf	5	194	95	21.14	87.55	87.54	0.82	0.65
554	3	inc	7	198	95	21.14	54.67	62.51	-0.51	-0.64
561	1	typ	11	224	625	20.50	157.49	168.11	1.12	0.80
567	1	inc	5	192	193	19.44	262.02	361.60	2.26	1.12
567	2	stp	7	184	193	19.44	39.03	41.17	1.24	1.20
567	3	inc	10	201	193	19.44	26.16	26.39	1.16	1.25
570	1	inc	7	299	48	34.71	79.20	79.50	1.06	1.04
579	1	typ	7	208	170	47.96	236.88	237.94	0.92	0.85
597	1	srf	14	271	263	11.35	26.25	28.49	0.81	0.65
600	1	oth	3	200	225	15.59	22.97	24.20	4.97	4.92
600	2	typ	5	202	225	15.59	42.68	51.11	0.81	0.42
626	1	inc	7	196	225	16.08	70.60	72.23	1.28	1.00
634	1	inc	4	168	107	12.91	56.25	62.04	2.51	0.93
645	1	srf	3	162	44	59.22	32.41	29.82	-0.16	0.03
645	2	stp	7	211	44	59.22	36.78	36.11	2.70	2.61
648	1	inc	18	405	542	20.48	38.03	45.51	1.22	0.65
649	1	dbl	12	229	79	16.76	137.11	137.70	1.00	0.61
669	1	inc	16	402	336	18.84	81.25	86.36	1.45	0.82
670	1	stp	14	401	1206	23.45	51.63	53.60	1.35	1.27
670	2	inc	9	224	1206	23.45	96.67	101.36	-0.42	-0.43

Table 3—Continued

Source	FlareNo	Type	SegNum	$< N >_{seg}$ (cnts)	N _{char} (cnts)	T _{char} (MK)	T _{pk, TRS, noCH} (MK)	T _{pk, TRS, CH} (MK)	$\zeta_{TRS, noCH}$	$\zeta_{TRS, CH}$
(1)	(2)	(3)	(4)	(5)	(6)	(7)	(8)	(9)	(10)	(11)
682	1	typ	10	216	255	23.62	927.22	927.22	2.89	2.62
682	2	typ	4	151	255	23.62	147.22	152.22	0.65	-0.07
682	3	typ	6	103	255	23.62	86.16	87.51	1.03	0.80
682	4	typ	5	99	255	23.62	927.20	927.22	3.88	3.20
689	1	srf	7	177	147	15.48	24.18	25.08	0.80	0.79
707	1	typ	5	175	213	19.87	38.83	46.97	0.02	-0.04
707	2	typ	5	186	213	19.87	51.36	52.49	1.79	1.48
718	1	inc	6	177	719	20.54	103.44	108.12	0.01	0.24
720	1	oth	13	210	135	21.96	47.34	48.46	0.72	0.85
737	1	stp	11	200	100	12.18	927.22	927.20	3.58	2.76
752	1	typ	22	1153	286	11.53	60.65	60.68	0.54	0.52
753	1	typ	6	194	180	16.27	75.55	76.55	1.24	0.72
761	1	typ	5	180	296	12.93	79.70	80.40	1.30	0.84
794	1	oth	3	84	79	16.06	47.87	51.69	1.39	1.29
801	1	oth	7	210	535	37.43	194.19	334.06	-3.50	-4.21
828	1	srf	8	202	178	20.67	75.55	90.94	1.67	1.54
828	2	typ	6	199	178	20.67	927.22	927.05	3.33	-0.36
848	1	inc	12	334	377	12.66	156.59	156.77	1.53	1.52
867	1	typ	4	201	643	18.78	160.98	162.88	2.21	2.17
871	1	typ	3	140	130	19.96	41.72	42.56	1.30	1.21
874	1	stp	13	307	45	18.19	308.84	313.21	1.89	1.78
881	1	typ	12	206	95	14.75	22.69	22.71	0.22	0.19
891	1	typ	10	164	105	24.29	320.78	326.16	0.80	0.13
891	2	typ	19	428	105	24.29	141.77	927.22	1.14	-0.18
894	1	stp	5	183	49	21.58	361.01	387.24	7.97	6.85
894	2	typ	7	191	49	21.58	123.57	124.71	1.20	0.92
894	3	oth	3	113	49	21.58	84.80	95.01	-1.27	-1.29
915	1	inc	15	316	264	23.99	926.68	927.22	3.24	3.12
932	1	typ	4	150	447	13.14	20.75	20.86	0.57	0.51
942	1	oth	6	201	319	14.56	44.03	46.03	1.93	1.16
942	2	typ	11	207	319	14.56	926.56	927.22	2.70	2.24
960	1	typ	16	236	83	9.20	46.70	46.73	0.08	0.08
971	1	typ	12	316	687	12.34	74.23	75.00	1.13	0.98
976	1	typ	8	219	68	15.60	174.46	174.86	1.11	0.97
976	2	dbl	4	190	68	15.60	52.25	53.32	1.45	1.33
982	1	oth	4	70	134	26.71	754.96	927.22	4.62	4.07
982	2	dbl	6	193	134	26.71	98.24	103.18	1.55	1.62
985	1	oth	6	182	984	16.29	112.00	130.54	5.48	4.27
985	2	typ	5	170	984	30.56	118.71	124.95	2.76	2.56
993	1	oth	5	100	75	24.77	63.57	67.07	-1.07	-0.98
997	1	stp	12	309	651	16.01	65.89	67.04	1.94	1.79
1028	1	typ	5	186	186	14.14	44.74	45.03	0.89	0.73
1040	1	typ	12	325	399	20.25	102.43	102.45	0.90	0.90
1044	1	stp	3	229	101	16.20	37.95	51.28	0.64	-0.33
1045	1	typ	4	185	87	19.33	95.72	96.70	1.31	1.13
1070	1	typ	5	174	159	25.66	927.22	927.22	2.93	2.54
1080	1	typ	5	169	190	46.65	45.12	45.12	0.55	0.56
1083	1	inc	23	434	723	15.73	62.13	67.14	0.97	0.20
1090	1	srf	7	101	113	15.18	28.88	29.37	0.77	0.32

Table 3—Continued

Source	FlareNo	Type	SegNum	$< N >_{seg}$ (cnts)	N _{char} (cnts)	T _{char} (MK)	T _{pk, TRS, noCH} (MK)	T _{pk, TRS, CH} (MK)	$\zeta_{TRS, noCH}$	$\zeta_{TRS, CH}$
(1)	(2)	(3)	(4)	(5)	(6)	(7)	(8)	(9)	(10)	(11)
1090	2	srf	7	206	113	15.18	29.37	32.29	-0.09	-0.13
1096	1	inc	4	117	49	16.30	55.11	55.11	0.28	0.24
1114	1	stp	19	436	487	35.61	89.53	91.73	1.27	0.90
1127	1	typ	5	178	182	15.48	63.68	64.58	1.20	0.99
1134	1	srf	4	204	205	20.96	26.62	30.88	-0.21	-0.36
1140	1	oth	5	203	36	21.76	60.72	61.16	0.15	0.11
1149	1	stp	4	114	70	17.09	52.13	53.36	1.64	1.58
1149	2	srf	4	201	70	17.09	47.42	54.63	2.03	1.41
1151	1	typ	5	146	401	16.25	64.54	66.68	2.68	2.47
1158	1	typ	4	100	148	29.76	107.19	109.45	0.74	0.34
1158	2	typ	4	83	148	29.76	256.03	326.77	3.91	3.49
1158	3	typ	9	107	148	29.76	94.84	96.90	0.39	0.19
1161	1	oth	7	203	191	20.02	60.62	63.75	0.81	0.72
1165	1	oth	6	183	93	22.97	66.65	69.71	0.59	0.49
1178	1	typ	4	102	87	32.26	58.00	58.33	0.30	0.27
1236	1	typ	5	171	170	12.79	56.03	56.12	0.18	0.13
1246	1	stp	14	310	169	12.51	84.86	84.95	0.76	0.73
1248	1	srf	8	193	685	15.84	33.87	37.72	2.53	2.53
1252	1	inc	8	245	352	12.04	67.30	67.38	0.95	0.88
1261	1	stp	6	103	463	12.75	423.71	454.82	2.46	2.44
1268	1	srf	9	101	75	25.48	140.39	140.41	-0.14	-0.24
1309	1	stp	5	270	188	20.01	225.07	388.09	4.66	0.49
1311	1	inc	4	217	316	12.37	25.80	29.84	1.06	0.65
1335	1	stp	6	208	111	21.35	81.41	86.70	0.77	-0.08
1341	1	typ	10	205	153	16.34	131.42	134.18	1.23	0.93
1343	1	stp	18	428	681	23.12	457.83	458.68	2.15	2.10
1350	1	inc	7	212	937	15.35	26.00	28.72	-0.15	-0.31
1354	1	oth	16	313	494	18.87	48.63	54.60	0.92	0.31
1374	1	inc	10	322	48	19.03	41.38	42.96	0.16	-0.17
1380	1	inc	7	180	288	27.76	927.22	927.22	6.16	6.11
1384	1	typ	11	218	181	15.79	37.25	49.41	1.50	0.84
1384	2	srf	7	205	181	15.79	56.70	63.12	1.32	0.58
1384	3	stp	10	206	181	15.79	59.46	62.61	1.84	1.74
1409	1	typ	5	182	119	39.36	86.55	87.05	0.64	0.44
1410	1	typ	16	416	24	10.64	71.10	72.41	0.71	0.30
1412	1	typ	4	201	189	12.84	27.90	30.02	1.81	1.58
1429	1	typ	5	428	121	15.39	39.45	64.01	4.60	1.98
1433	1	typ	5	305	97	12.61	58.80	59.77	0.86	0.31
1433	2	oth	4	203	97	12.61	30.95	927.22	0.91	-2.49
1443	1	stp	10	350	265	15.35	97.64	97.86	1.22	1.07
1444	1	inc	5	101	145	78.97	527.15	522.87	-6.68	-6.60
1444	2	stp	7	207	145	78.97	129.64	130.35	0.96	1.21
1444	3	dbl	9	104	145	78.97	927.10	927.16	1.22	1.18
1449	1	stp	9	228	154	19.81	223.04	224.11	1.80	1.55
1462	1	inc	5	455	505	21.64	210.52	210.72	2.85	2.84
1463	1	stp	5	202	586	12.07	29.67	32.52	1.03	0.83
1463	2	typ	3	118	586	12.07	58.20	58.89	1.42	1.30
1463	3	stp	7	201	586	12.07	49.31	50.71	2.25	2.07
1463	4	stp	4	250	586	12.07	53.84	63.90	3.09	1.69

Table 3—Continued

Source	FlareNo	Type	SegNum	$< N >_{\text{seg}}$ (cnts)	N _{char} (cnts)	T _{char} (MK)	T _{pk, TRS, noCH} (MK)	T _{pk, TRS, CH} (MK)	$\zeta_{TRS, noCH}$	$\zeta_{TRS, CH}$
(1)	(2)	(3)	(4)	(5)	(6)	(7)	(8)	(9)	(10)	(11)
1466	1	inc	5	301	52	20.39	40.34	40.65	0.44	0.34
1473	1	stp	13	102	375	12.40	83.60	95.02	1.30	1.13
1479	1	typ	4	201	73	13.03	41.69	48.66	2.47	0.84
1481	1	stp	6	154	121	12.43	34.36	35.75	1.28	1.23
1487	1	typ	7	105	151	11.68	34.06	34.09	0.66	0.34
1487	2	stp	8	100	151	11.68	67.32	71.86	1.31	0.66
1489	1	inc	10	207	349	12.93	28.38	33.95	0.85	0.15
1492	1	srf	3	79	689	12.97	67.86	72.83	1.85	1.90
1492	2	srf	4	160	689	12.97	29.83	30.51	0.59	0.07
1499	1	typ	5	202	61	13.02	39.24	39.25	0.30	0.30
1499	2	srf	10	202	61	13.02	89.24	90.70	1.85	1.72
1516	1	typ	3	106	162	12.24	94.33	97.98	1.84	1.44
1521	1	inc	11	204	189	16.32	42.10	47.91	2.34	1.97
1568	1	typ	31	1900	1764	14.85	553.02	557.98	1.44	1.19
1570	1	inc	6	201	26	32.07	32.63	32.64	1.18	1.37
1595	1	oth	3	200	216	11.74	22.84	31.01	1.98	0.28
1603	1	typ	7	100	216	20.20	48.37	48.83	-0.22	-0.28
1608	1	stp	14	209	166	16.13	67.15	68.16	1.05	0.99
1608	2	typ	5	107	166	16.13	33.56	33.69	0.71	0.69
1608	3	inc	5	200	166	16.13	31.05	31.93	0.55	0.34

Note. — Columns 1-3: Source number, flare number and flare morphological type (reproduced from Table 2). Columns 4-5: Number of segments and the average number of X-ray counts per segment used in the TRS analysis. Columns 6-7: Number of X-ray counts in the “characteristic” segment and inferred “characteristic” plasma temperature. Columns 8-9: Inferred peak flare plasma temperatures without (“noCH”) and with (“CH”) account for the “characteristic” background. Columns 10-11: Inferred average slopes of the temperature-density trajectory without (“noCH”) and with (“CH”) accounting for the “characteristic” background.

Table 4. COUP star properties

Source (1)	NC (cnts) (2)	BG (cnts) (3)	ME (keV) (4)	$\log N_H$ (cm $^{-2}$) (5)	J (mag) (6)	H (mag) (7)	K_s (mag) (8)	F1 (9)	$\Delta(H - K_s)$ (mag) (10)	[3.6] (mag) (11)	[4.5] (mag) (12)	M (M_\odot) (13)	R (10 10 cm) (14)	P (day) (15)	R_{cor} (10 10 cm) (16)	EW(Ca II) (Å) (17)
7	41952	362	1.20	20.93	8.85	8.10	7.95	AAA000	-0.28	2.12	43.61
9	16271	199	1.34	21.37	10.22	9.65	9.46	AAA000	-0.15	2.11	20.72
11	5700	123	1.53	21.69	10.53	9.46	8.60	AAA000	0.25	0.69	24.22	-14.60
23	55449	320	1.29	21.24	10.01	9.33	9.09	AAA000	-0.16	8.873 \pm 0.003	8.817 \pm 0.002	2.17	26.74	3.45	86.69	...
27	5948	153	1.26	21.08	12.16	11.37	11.05	AAA000	-0.14	10.855 \pm 0.005	10.789 \pm 0.004	0.53	12.67	1.50	31.10	1.80
28	20863	149	1.39	21.10	11.53	10.84	10.53	AAA000	-0.09	10.332 \pm 0.004	10.264 \pm 0.004	0.53	16.10	4.41	63.83	1.60
43	7021	63	1.32	21.27	11.23	10.38	10.08	AAA000	-0.19	9.781 \pm 0.005	9.716 \pm 0.005	0.40	20.44	1.40
57	4093	5	1.13	20.68	11.01	10.53	10.28	AEE000	...	10.016 \pm 0.003	9.988 \pm 0.004	1.19	15.19	2.34	54.78	1.60
62	9294	66	1.39	21.08	11.23	10.21	9.53	AAA000	0.10	8.530 \pm 0.003	8.049 \pm 0.002	1.52	13.16	6.63	119.00	0.00
66	6237	28	1.37	21.04	12.13	11.20	10.63	AAA000	0.04	9.713 \pm 0.003	9.249 \pm 0.002	0.24	12.74	-2.80
67	7690	41	1.23	21.24	10.85	9.97	9.62	AAA000	-0.16	9.177 \pm 0.011	8.878 \pm 0.007	0.29	27.30	8.83	82.93	0.00
71	6597	43	1.10	20.00	11.88	11.19	11.01	AAA000	-0.22	10.837 \pm 0.005	10.788 \pm 0.004	0.37	13.58	2.03	33.76	1.60
90	7117	139	1.93	21.98	12.68	11.44	10.97	AAA000	-0.23	0.52	17.57	1.37	29.09	1.60
101	10019	74	1.39	21.12	13.09	12.45	12.05	AAA000	0.02	0.16	10.64	2.90
107	9004	571	1.28	20.71	8.95	8.23	8.06	AAA000	-0.25	7.915 \pm 0.003	7.923 \pm 0.002	2.69	40.32	17.40	273.88	...
108	6262	51	1.39	21.37	11.66	10.82	10.54	AAA000	-0.20	0.37	13.93	1.95	32.86	1.50
112	7398	70	1.34	21.47	12.49	11.64	11.29	AAA000	-0.14	10.520 \pm 0.003	10.213 \pm 0.003	0.33	11.06	6.52	70.73	-0.70
113	6724	82	1.32	21.37	10.32	9.65	9.37	AAA000	-0.11	2.20	20.79	5.77	122.71	...
115	6140	22	1.66	21.98	12.20	10.91	10.43	AAA000	-0.25	10.028 \pm 0.006	9.974 \pm 0.011	0.71	14.07	3.43	59.51	1.40
122	4939	22	1.37	21.30	12.51	11.72	11.32	AAA000	-0.06	10.510 \pm 0.010	10.039 \pm 0.010	0.26	11.06	9.19	82.13	0.00
123	5347	262	1.48	21.24	10.24	9.46	9.14	AAA000	-0.13	0.60	26.39	0.80
124	5074	440	1.40	21.14	10.24	9.46	9.14	AAA000	-0.13	0.60	26.39	0.80
131	9038	34	1.70	21.88	11.98	10.95	10.24	AAA000	0.12	9.275 \pm 0.007	8.962 \pm 0.006	1.20	15.61	14.41	184.55	1.40
139	6094	29	1.22	20.95	12.12	11.28	10.91	AAA000	-0.11	9.941 \pm 0.005	9.475 \pm 0.005	0.33	11.90	9.04	87.95	0.90
141	13727	16	1.31	21.07	10.23	9.42	8.99	AAA000	-0.04	8.146 \pm 0.004	7.744 \pm 0.002	2.11	23.10	-17.80
142	5311	16	1.26	20.98	9.51	9.35	9.25	AAAc00	...	9.179 \pm 0.006	9.122 \pm 0.006	2.65	14.49
150	6138	14	1.32	21.34	11.48	10.61	10.29	AAAcc0	...	9.664 \pm 0.007	9.523 \pm 0.006	0.29	21.35	1.92	29.99	1.50
152	6023	14	1.15	20.00	11.38	10.60	10.30	AEEc0	...	9.497 \pm 0.006	9.196 \pm 0.003
160	4699	59	3.10	22.45	16.42	14.10	12.75	AAAc00	...	11.655 \pm 0.031	11.471 \pm 0.018
173	12329	26	1.20	21.06	10.91	10.15	9.86	...	-0.15	9.484 \pm 0.004	9.372 \pm 0.005	0.37	19.67	2.33	37.00	1.00
183	5763	12	1.85	22.13	12.03	10.31	9.23	...	0.12	7.984 \pm 0.006	7.631 \pm 0.005	0.00
202	5102	47	1.31	21.28	11.24	10.44	10.12	AAA000	-0.14	0.37	19.11	4.45	56.96	1.50
205	6383	17	1.28	21.07	12.08	11.19	10.90	...	-0.22	10.022 \pm 0.004	9.765 \pm 0.004	0.33	13.30	10.20	95.32	1.20
223	10243	62	1.85	22.05	11.53	10.10	9.34	AAA000	-0.04	8.222 \pm 0.008	7.810 \pm 0.006	1.19	19.53	8.46	129.03	1.70
262	11540	10	1.95	22.15	11.66	10.07	9.30	...	-0.12	8.629 \pm 0.006	8.539 \pm 0.008	1.13	11.06	2.30
270	6647	7	1.19	20.93	11.45	10.68	10.38	...	-0.15	10.251 \pm 0.012	10.363 \pm 0.030	0.41	16.31	1.91	33.54	1.50
310	6167	21	1.72	22.02	11.76	10.40	9.62	AAA000	0.01	8.802 \pm 0.018	8.191 \pm 0.010	8.90
323	5146	43	1.72	21.95	12.44	11.11	10.46	AAA000	-0.10	9.893 \pm 0.009	9.810 \pm 0.004	0.57	13.23	6.40	83.82	2.00
325	4890	81	1.25	20.90	11.26	10.38	9.83	AAA000	0.04	1.30	12.39	0.00
331	5789	144	2.50	22.21	12.48	10.55	9.36	AAA000	0.11	6.09
332	3258	10	2.61	22.37	13.80	11.69	10.56	...	-0.04	9.055 \pm 0.010	8.470 \pm 0.007
342	16568	17	1.98	22.21	11.73	10.25	9.62	...	-0.20	8.926 \pm 0.016	8.850 \pm 0.035	1.23
343	33934	9	1.31	21.02	10.46	9.66	9.39	...	-0.19	8.941 \pm 0.022	8.781 \pm 0.030	0.59	22.61	19.50	178.20	1.90
365	6486	12	2.18	22.16	11.14	9.66	8.82	...	0.01	7.458 \pm 0.010	6.852 \pm 0.010	0.72	5.18	0.00
382	5065	15	1.25	21.28	11.24	10.39	9.94	...	-0.04	9.009 \pm 0.047	8.664 \pm 0.059	0.69	16.17	7.33	97.79	0.00
387	20090	12	1.32	21.33	9.70	8.83	8.26	...	0.07	7.363 \pm 0.005	6.967 \pm 0.003	2.34	24.43
394	4051	324	1.20	20.00	8.97	8.14	7.89	...	-0.23	7.638 \pm 0.014	7.581 \pm 0.018	0.74	53.76	8.00	106.11	1.90
417	6124	13	1.32	21.17	12.12	11.30	11.04	UAA0cc	...	9.888 \pm 0.009	9.688 \pm 0.007	0.41	11.48	2.94	44.71	...
431	20614	77	1.45	21.68	9.54	8.86	8.63	AAA000	-0.17	8.475 \pm 0.006	8.457 \pm 0.006	2.61	33.74

Table 4—Continued

Source (1)	NC (cnts) (2)	BG (cnts) (3)	ME (keV) (4)	$\log N_H$ (cm $^{-2}$) (5)	J (mag) (6)	H (mag) (7)	K_s (mag) (8)	F1 (9)	$\Delta(H - K_s)$ (mag) (10)	[3.6] (mag) (11)	[4.5] (mag) (12)	M (M_\odot) (13)	R (10 10 cm) (14)	P (day) (15)	R_{cor} (10 10 cm) (16)	EW(Ca II) (Å) (17)
449	8614	14	2.10	22.20	12.26	10.45	9.38	...	0.06	7.408 ± 0.007	6.730 ± 0.004	0.00
452	5002	10	1.76	22.06	11.03	9.73	8.99	AAE000	...	7.933 ± 0.007	7.419 ± 0.005	2.02	23.45	1.40
454	17125	16	1.82	21.99	10.83	9.61	9.10	...	-0.18	8.137 ± 0.006	7.835 ± 0.014	2.35	32.06	9.81	178.68	2.10
459	8058	142	1.19	20.51	11.07	10.34	10.08	AAA000	-0.16	0.27	17.43
470	12569	10	1.19	21.02	10.72	9.91	9.60	...	-0.16	8.976 ± 0.064	8.379 ± 0.049	0.52	17.08	1.50
485	4234	18	2.04	22.04	13.47	12.11	11.50	AAA000	-0.16	10.626 ± 0.103	10.309 ± 0.097	0.22	3.92	7.44	67.47	-1.00
490	6682	89	1.63	21.88	11.40	10.10	9.61	AAA000	-0.24	9.275 ± 0.008	9.240 ± 0.009	0.70	28.28	1.20
499	5381	108	1.47	21.74	11.68	10.71	10.35	AAA000	-0.19	0.69	18.69	9.08	112.79	1.20
515	4393	12	1.67	21.98	12.29	10.96	10.43	...	-0.22	9.824 ± 0.042	9.734 ± 0.024	0.90	23.24	4.41	76.15	0.00
554	14045	10	3.67	22.74	12.50	12.72	10.42	UAE0c0	...	7.934 ± 0.031	6.606 ± 0.015
561	13662	23	2.10	22.15	11.12	9.41	8.34	...	0.11	6.864 ± 0.006	6.041 ± 0.003	...	4.48	10.08	...	1.00
567	10847	96	1.32	21.26	10.18	9.26	8.62	AAA000	0.11	1.20	20.72	-3.50
570	4070	13	3.35	22.64	16.28	12.70	10.24	...	0.49	8.389 ± 0.051	7.428 ± 0.043
579	7100	47	1.69	21.68	10.80	9.59	8.78	...	0.13	8.140 ± 0.165	8.317 ± 0.518	0.33	21.84	-17.40
597	8523	19	1.12	20.00	11.47	10.61	10.06	...	0.06	8.927 ± 0.038	8.599 ± 0.042	1.49	14.07	4.50
600	5172	11	1.29	21.34	11.13	10.18	9.26	...	0.38	0.26	29.75
626	5511	53	1.58	21.79	12.38	11.19	10.78	AAA000	-0.26	10.380 ± 0.005	10.341 ± 0.016	0.41	15.33	8.30	89.31	0.70
634	4254	9	1.38	21.40	12.25	11.42	11.09	...	-0.15	11.031 ± 0.177	10.941 ± 0.340	0.33	10.15	-1.50
645	4471	12	1.91	22.14	11.57	9.88	9.01	...	-0.08	7.989 ± 0.008	7.378 ± 0.003	4.40
648	24413	42	1.45	21.52	10.44	9.53	9.14	...	-0.13	0.72	33.32
649	5076	29	1.83	21.95	12.64	11.38	10.84	...	-0.17	0.40	15.19	0.00
669	20431	33	1.47	21.51	10.92	10.06	9.76	...	-0.19	1.52	18.13
670	29745	38	1.51	21.60	10.27	9.31	8.66	...	0.10	7.683 ± 0.107	6.869 ± 0.290	1.68	27.30	8.67	147.14	-1.00
682	8958	48	2.12	21.91	10.78	9.26	8.63	...	-0.22	7.308 ± 0.011	6.891 ± 0.026	1.86	24.85
689	6931	613	1.32	20.85	10.06	9.30	9.02	...	-0.16	2.09	22.82	1.00
707	6548	23	1.55	21.68	11.41	10.36	9.77	...	-0.01	0.33	18.97	1.60
718	18079	12	1.47	21.57	10.08	9.17	8.73	...	-0.08	8.293 ± 0.028	8.246 ± 0.033	0.55	35.70	5.74	77.03	...
720	7238	50	2.02	22.18	12.72	10.93	10.03	AAA000	-0.10	8.790 ± 0.005	8.472 ± 0.004
737	4326	11	1.57	21.67	12.46	11.29	10.71	...	-0.08	9.722 ± 0.028	9.499 ± 0.018	0.37	11.27	9.66	95.50	0.80
752	34586	674	1.47	21.33	11.79	11.02	10.74	AAA000	-0.17	0.54	11.69	1.10
753	5729	160	1.47	21.58	11.63	10.77	10.32	AAA000	-0.04	0.91	14.42	1.80
761	10738	18	1.45	21.57	11.13	10.06	9.48	...	-0.03	8.548 ± 0.030	7.972 ± 0.016	1.35	12.81
794	4185	96	1.55	21.84	11.95	10.84	10.31	AAA000	-0.10	0.46	15.05	2.30
801	12283	12	1.64	21.63	10.14	9.19	8.61	...	0.04	7.951 ± 0.064	7.399 ± 0.063	0.70	28.98	-1.20
828	12067	10	1.58	21.55	10.01	9.18	8.89	...	-0.19	8.555 ± 0.117	8.139 ± 0.023	0.90	24.01	1.20
848	7193	19	1.42	21.22	12.43	11.67	11.30	...	-0.07	10.313 ± 0.307	10.403 ± 0.349	0.29	13.86	0.00
867	15382	11	1.44	21.58	9.44	8.56	8.19	...	-0.14	7.983 ± 0.016	7.980 ± 0.031	2.62	47.88	3.42	91.78	1.60
871	4417	15	1.50	21.71	12.65	11.58	11.12	...	-0.15	10.802 ± 0.099	10.668 ± 0.122	0.49	10.01	14.24	135.84	0.00
874	7754	9	3.85	22.77	...	14.31	12.46	10.631 ± 0.485	9.186 ± 0.113
881	4521	375	1.33	20.00	11.12	10.58	10.23	...	0.03	9.555 ± 0.185	9.245 ± 0.164	0.41	16.52	2.00
891	12686	707	2.64	22.07	10.91	9.08	8.21	AAA000	-0.15	7.665 ± 0.003	7.537 ± 0.002	2.43	33.95	6.83	141.94	1.80
894	5431	14	2.28	22.19	13.81	11.82	10.95	AAA000	-0.24	10.231 ± 0.027	10.047 ± 0.029
915	17307	32	2.55	22.29	13.63	11.21	9.98	AAA000	-0.11	8.817 ± 0.010	8.496 ± 0.006
932	6648	881	1.29	21.17	8.70	7.91	7.57	...	-0.12	7.118 ± 0.008	7.002 ± 0.009	2.52	57.61	8.53	166.61	-1.70
942	11014	12	2.11	22.23	11.98	10.43	9.67	...	-0.11	0.52	18.41	0.00
960	5226	53	1.28	21.09	12.92	12.27	11.95	AAA000	-0.06	11.459 ± 0.030	11.370 ± 0.022	0.24	15.12	0.00
971	26664	27	1.18	20.00	10.48	9.63	9.77	UUA00c	0.69	22.96	1.80
976	3883	11	1.74	21.79	12.76	11.57	11.01	...	-0.11	10.121 ± 0.014	9.839 ± 0.017	0.18	6.37	0.00
982	5995	14	1.54	21.47	10.70	9.77	9.82	UUA00c	0.73	8.40	1.80

Table 4—Continued

Source (1)	NC (cnts) (2)	BG (cnts) (3)	ME (keV) (4)	$\log N_H$ (cm $^{-2}$) (5)	J (mag) (6)	H (mag) (7)	K_s (mag) (8)	F1 (9)	$\Delta(H - K_s)$ (mag) (10)	[3.6] (mag) (11)	[4.5] (mag) (12)	M (M_\odot) (13)	R (10 10 cm) (14)	P (day) (15)	R_{cor} (10 10 cm) (16)	EW(Ca II) (Å) (17)
985	31842	13	1.63	21.88	8.69	7.75	7.37	...	-0.16	7.024 ± 0.004	6.869 ± 0.003	2.97	35.63
993	4873	22	1.79	22.06	10.78	9.58	8.84	...	0.06	7.625 ± 0.014	7.297 ± 0.004	1.88	24.71	-0.30
997	15283	13	1.50	21.60	11.63	10.68	10.31	...	-0.17	9.786 ± 0.169	9.651 ± 0.207
1028	5044	12	1.92	22.19	10.93	9.75	9.11	...	-0.03	8.504 ± 0.029	8.421 ± 0.028	1.60	14.14
1040	8120	159	2.50	22.28	13.99	11.49	10.16	AAAc00	7.83
1044	4217	25	1.42	21.56	12.61	11.73	11.34	...	-0.12	10.746 ± 0.097	10.504 ± 0.168	0.62	11.83	8.09	100.78	-2.80
1045	4273	7	1.72	21.80	11.08	9.99	9.17	...	0.20	8.485 ± 0.013	7.928 ± 0.006	0.29	18.76	-7.00
1070	4733	12	1.86	21.92	12.91	11.38	10.34	...	0.18	9.226 ± 0.006	8.652 ± 0.022	5.38
1080	5988	236	2.71	22.40	9.65	7.72	6.43	AAA000	0.21	1.98	65.59	-16.90
1083	13814	18	1.51	21.67	11.12	10.08	9.72	...	-0.23	9.166 ± 0.103	9.204 ± 0.159	5.89
1090	4306	371	1.56	21.67	8.10	6.87	5.92	...	0.25	5.00	92.05
1096	4756	72	1.50	21.44	11.62	10.72	10.16	AAA000	0.04	0.18	18.62	-5.00
1114	36348	148	1.98	21.98	9.80	8.58	8.04	AAA000	-0.15	1.73	...	-1.50
1127	5598	81	1.51	21.79	12.08	11.03	10.64	AAA000	-0.21	0.90	17.85	7.20	105.58	1.40
1134	4922	152	1.22	20.97	11.57	10.62	10.03	AAA000	0.05	1.17	13.02	1.44	39.41	1.30
1140	7031	12	2.20	22.18	12.80	11.28	10.40	...	0.03	9.526 ± 0.043	8.864 ± 0.057
1149	4491	20	1.50	21.70	11.67	10.77	10.24	...	0.01	9.102 ± 0.031	8.651 ± 0.031	0.70	14.00	10.50	124.86	...
1151	24094	18	1.28	21.03	10.48	9.64	9.40	...	-0.24	9.165 ± 0.008	9.129 ± 0.010	0.91	24.36	11.50	144.80	1.90
1158	8508	16	1.77	21.86	11.90	10.54	9.70	...	0.07	8.388 ± 0.017	7.925 ± 0.013	0.41	14.00	0.00
1161	9270	12	1.47	21.59	11.80	10.90	10.51	...	-0.13	9.737 ± 0.025	9.833 ± 0.072	0.54	10.50	3.90	59.17	1.50
1165	4517	16	3.20	22.59	16.70	14.01	11.91	...	0.61	9.575 ± 0.053	9.072 ± 0.044
1178	4035	139	1.63	21.89	12.74	11.54	11.05	AAA000	-0.19	0.22	17.78	6.34	60.65	0.10
1236	4379	148	1.23	20.98	12.02	11.22	10.87	AAA000	-0.11	0.41	14.00	13.87	125.77	0.90
1246	7615	25	1.51	21.43	12.60	11.56	10.96	AAA000	0.01	10.406 ± 0.006	10.018 ± 0.019	0.23	11.34	5.21	54.00	0.00
1248	14567	32	1.38	21.49	11.44	10.50	10.19	AAA0s0	...	9.950 ± 0.040	9.931 ± 0.025	0.47	17.57	3.28	50.34	1.70
1252	5687	25	1.44	21.62	11.99	11.12	10.79	AAA0ss	...	10.151 ± 0.039	9.962 ± 0.020	0.53	12.18	11.68	122.18	1.60
1261	5735	8	1.45	21.31	12.41	11.63	11.27	...	-0.09	10.361 ± 0.060	9.393 ± 0.063
1268	4668	10	1.77	21.80	11.40	10.11	9.38	...	0.00	8.031 ± 0.016	7.550 ± 0.007	0.41	11.62	-0.90
1309	8300	10	1.82	22.00	10.64	9.39	8.75	...	-0.07	7.826 ± 0.022	7.506 ± 0.022	1.90	18.69
1311	5107	6	1.22	21.21	11.01	10.17	9.94	...	-0.25	1.53	19.04
1335	5466	8	1.92	21.97	11.97	10.74	9.99	...	0.05	9.202 ± 0.045	8.896 ± 0.034	0.64	9.52	10.22	119.02	-2.50
1341	8230	13	1.99	22.17	11.42	9.96	9.32	...	-0.18	8.722 ± 0.014	8.689 ± 0.015
1343	16586	22	1.92	21.92	12.02	10.61	9.78	...	0.04	8.936 ± 0.005	8.622 ± 0.004	8.66
1350	29644	45	1.23	21.21	9.70	9.15	8.97	AAAsss	...	8.878 ± 0.009	8.859 ± 0.007	2.20	24.71	2.80	75.77	1.70
1354	13951	13	1.60	21.73	9.67	9.04	8.80	...	-0.13	7.961 ± 0.006	7.563 ± 0.003	2.34	27.65
1374	5309	128	1.54	21.64	12.75	11.76	11.16	AAA000	0.03	5.56
1380	14749	11	1.67	21.79	11.69	10.31	9.27	...	0.26	8.103 ± 0.004	7.632 ± 0.001	1.52	18.41
1384	25433	17	1.34	20.88	10.95	10.18	9.96	...	-0.23	9.734 ± 0.006	9.686 ± 0.011	0.52	17.22	2.85	47.41	1.90
1409	6381	8	1.98	22.02	11.70	10.15	9.20	...	0.08	8.120 ± 0.007	7.623 ± 0.004	0.74	7.35	9.57	119.57	-6.30
1410	8154	55	1.70	21.83	13.60	12.31	11.85	AAA000	-0.27	0.36	3.57	6.76	74.59	0.00
1412	7594	10	1.23	21.20	11.56	10.65	10.39	...	-0.26	9.587 ± 0.013	9.297 ± 0.016	0.37	18.27	9.23	92.64	1.80
1429	5527	10	1.19	20.81	12.00	11.11	10.90	...	-0.30	10.631 ± 0.027	10.496 ± 0.033	0.43	39.34	7.52	84.97	1.20
1433	6307	124	1.37	21.32	12.02	11.22	10.93	AAAcss	13.87
1443	9845	13	1.37	21.29	11.11	10.31	10.08	...	-0.23	9.800 ± 0.019	9.837 ± 0.013	1.32
1444	8199	15	1.76	21.65	11.78	10.94	10.43	...	0.03	9.678 ± 0.005	9.207 ± 0.007	0.60	13.58	7.78	97.12	-4.10
1449	5704	53	1.58	21.64	12.42	11.35	10.91	AAA00s
1462	12983	152	1.55	21.61	10.12	9.25	8.92	AAAddd	2.54	27.86	6.76	143.06	...
1463	8214	42	1.19	20.51	10.78	10.00	9.50	AAA0ss	...	8.768 ± 0.004	8.385 ± 0.002	0.59	20.51	10.66	119.14	...
1466	5271	12	1.61	21.74	11.69	10.78	10.38	...	-0.12	9.734 ± 0.028	9.361 ± 0.007	1.40	13.37	1.40

Table 4—Continued

Source (1)	NC (cnts) (2)	BG (cnts) (3)	ME (keV) (4)	$\log N_H$ (cm^{-2}) (5)	J (mag) (6)	H (mag) (7)	K_s (mag) (8)	F1 (9)	$\Delta(H - K_s)$ (mag) (10)	[3.6] (mag) (11)	[4.5] (mag) (12)	M (M_\odot) (13)	R (10^{10} cm) (14)	P (day) (15)	R_{cor} (10^{10} cm) (16)	EW(Ca II) (Å) (17)
1473	26525	20	1.37	21.35	7.79	7.64	7.54	AAA000	-0.01	7.175 ± 0.009	6.840 ± 0.008	5.00	30.38
1479	4999	105	1.18	20.32	12.28	11.65	11.33	AAA000	-0.05	10.982 ± 0.008	10.893 ± 0.006	...	17.57	5.54	...	0.00
1481	4147	68	1.07	20.00	12.66	11.95	11.78	AAA000	-0.24	11.501 ± 0.011	11.479 ± 0.015	0.21	12.39	1.58	23.65	0.00
1487	5660	67	1.35	21.47	11.55	10.61	10.28	AAA00s	0.40	20.16	5.70	68.95	...
1489	15457	152	1.20	21.14	9.31	8.61	8.40	AAA000	-0.20	2.59	33.25
1492	6781	19	1.20	21.07	11.63	10.88	10.57	AAA000	-0.12	10.340 ± 0.010	10.310 ± 0.010	0.37	15.12	1.10	22.44	1.60
1499	6200	146	1.66	21.77	11.39	10.46	9.85	AAA000	0.08	9.079 ± 0.004	8.776 ± 0.002
1516	7737	60	1.09	20.00	11.72	11.05	10.89	AAA000	-0.23	10.734 ± 0.010	10.763 ± 0.010	1.40	12.46	1.65	45.81	1.80
1521	10061	31	1.29	21.16	11.24	10.36	9.83	UAA0cc	...	8.904 ± 0.025	8.551 ± 0.018	1.40	13.16
1568	89438	268	1.25	20.44	9.36	8.84	8.63	AAA000	-0.10	2.55	27.93
1570	4146	112	1.53	21.64	11.39	10.57	10.12	AAA000	-0.02	0.92	13.30	9.56	128.48	1.80
1595	6861	60	1.06	20.00	11.89	11.19	10.97	AAA000	-0.19	0.29	15.05	4.91	56.08	...
1603	4198	135	1.95	22.24	13.18	11.41	10.67	AAA000	-0.25	0.00	...
1608	9098	269	1.38	21.22	11.96	11.06	10.41	AAA000	0.13	0.48	12.32	4.21	59.87	-1.30

Note. — Columns 1-5: COUP source number, source net counts, background counts within source's extraction region, source X-ray median energy, and inferred column density. All values are from Getman et al. (2005a). Columns 6-8: VLT and 2MASS JHK_s magnitudes as reported in Getman et al. (2005a). Column 9: Flag indicating source of the NIR photometry ("..."=VLT, otherwise 2MASS) and quality of the 2MASS photometry as discussed in Getman et al. (2005a). Column 10: Color excess measured from the rightmost reddening vector on the $J - H$ vs. $H - K_s$ color-color diagram (originating at $\sim 0.1 M_\odot$ assuming an age of 1 Myr and using PMS models of Siess et al. (2000)). Columns 11-12: *Spitzer*-IRAC [3.6] and [4.5] magnitudes and their statistical errors obtained in this work. Columns 13-14: Stellar mass and radius as listed in Getman et al. (2005a). Column 15: Stellar rotation periods with extended rotation data for COUP sources as listed in Flaccomio et al. (2005). Column 16: Calculated Keplerian corotation radius for stars with known M and P . Column 17: Equivalent width of the 8542 Å Ca II line as listed in Getman et al. (2005a).

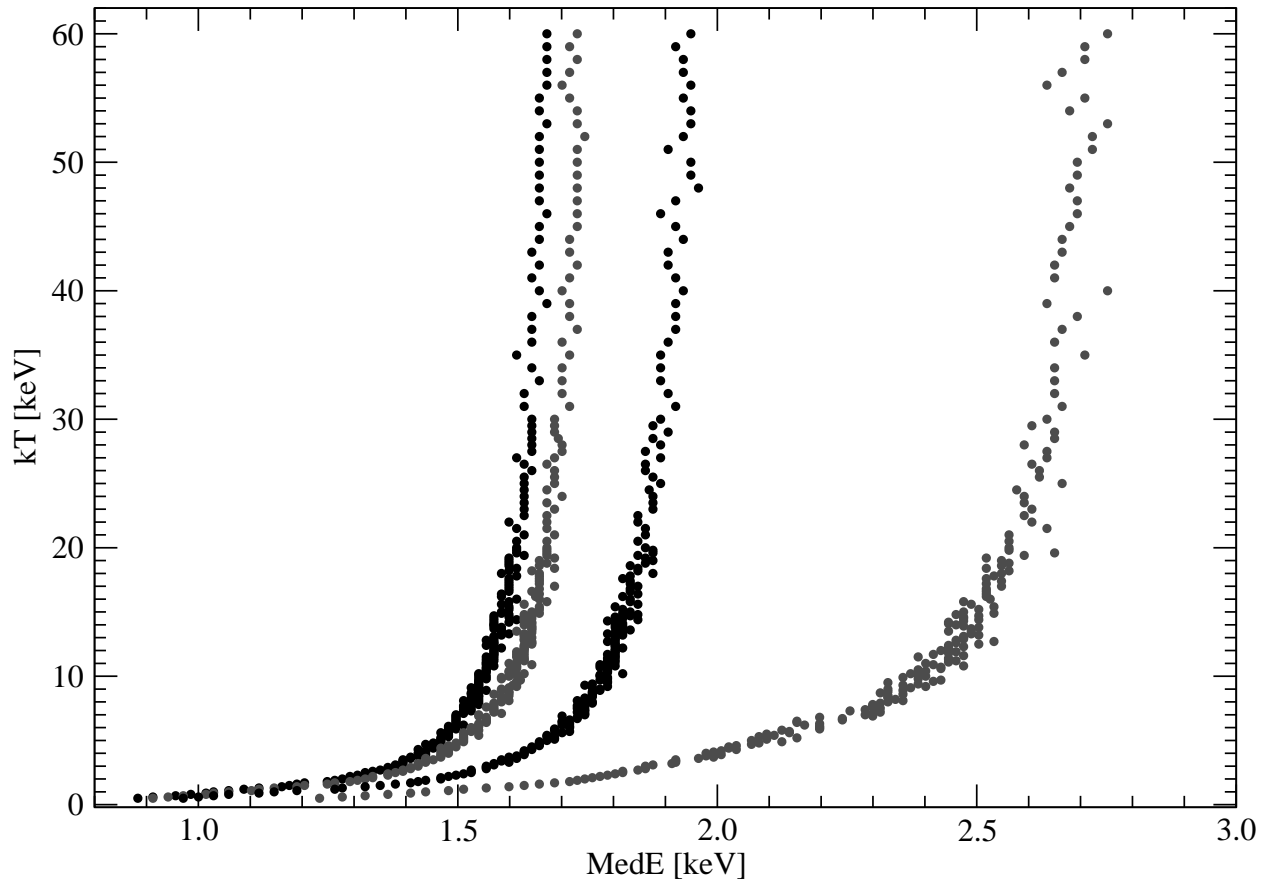


Fig. 1.— Calibration of plasma temperature vs. observed X-ray median energy for representative column densities ($\log N_H = (20.5, 21, 21.5, 22)$ cm $^{-2}$, from left to right) calculated from spectral simulations.

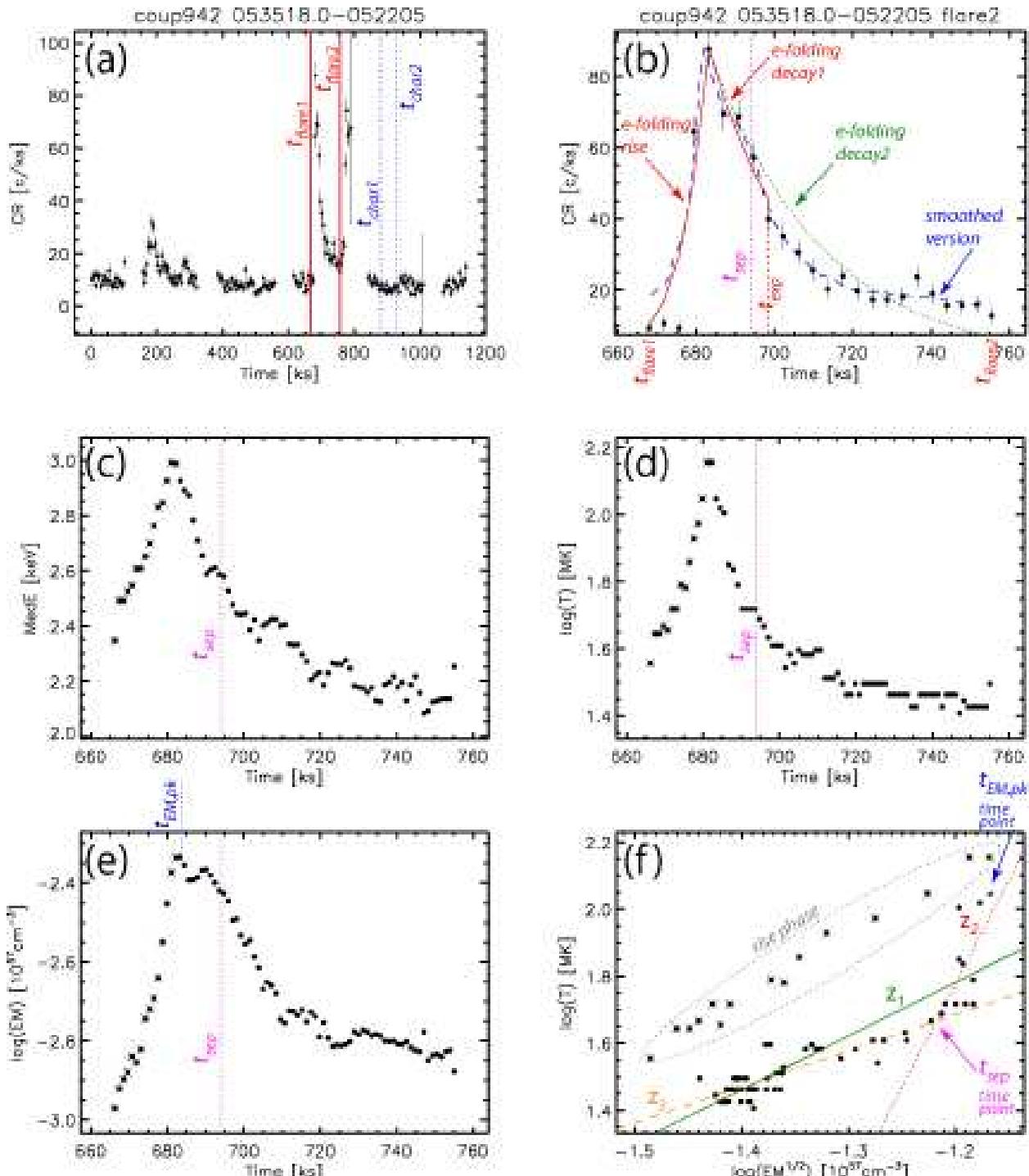


Fig. 2.— Illustration of our X-ray spectral modeling procedure using flare #2 of COUP #942 using the method of adaptively smoothed median energy (MASME). Details on specific symbols and lines are provided in §2.4. (a) X-ray lightcurve over the whole COUP observation (six nearly consecutive exposures) from the COUP Atlas of Getman et al. (2005a). (b) Lightcurve of the flare in binned histogram (black) and adaptively smoothed (blue) representations. (c) Evolution of the median energy. (d) Evolution of the plasma temperature. (e) Evolution of the emission measure. (f) Evolution in the $\log T - \log \sqrt{(EM)}$ plane. [See the electronic edition of the journal for the full COUP flare atlas, Figs. 2.2-2.216].

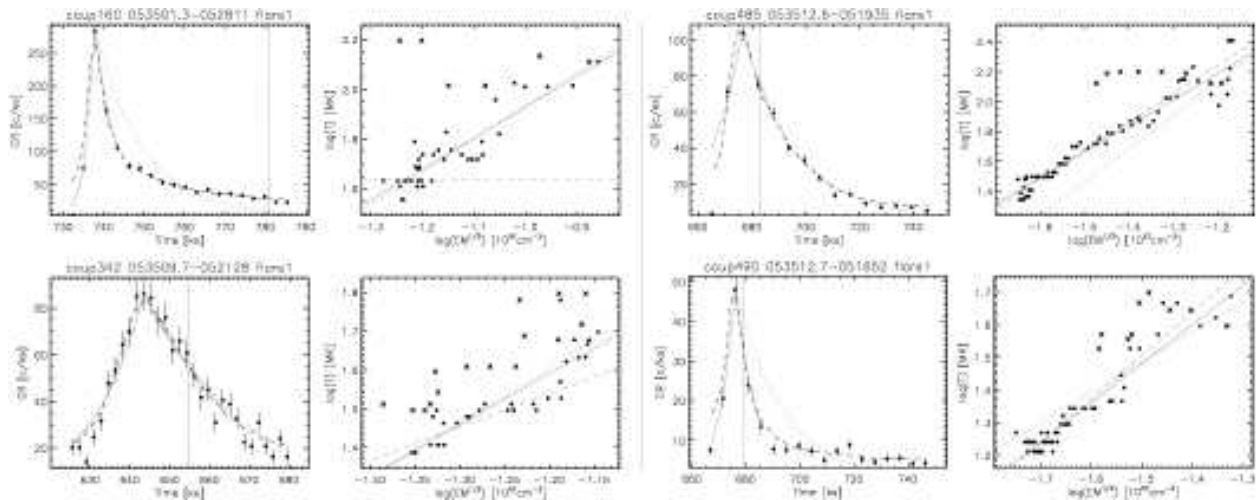


Fig. 3.— Lightcurves and inferred temperature-density trajectories for four representative flares in the class “typical”.

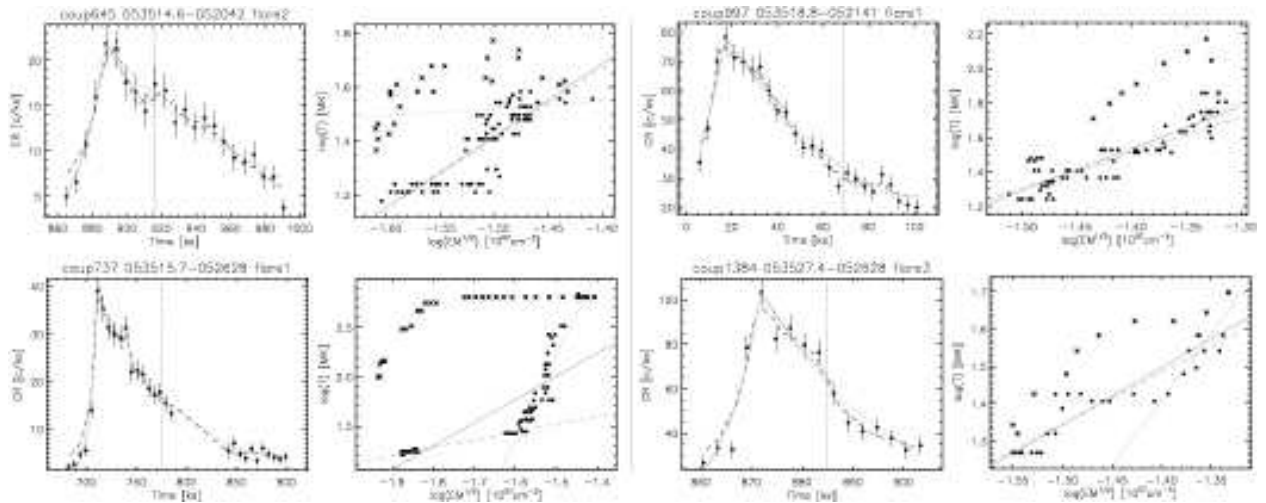


Fig. 4.— Lightcurves and inferred temperature-density trajectories for four representative flares in the class “step”.

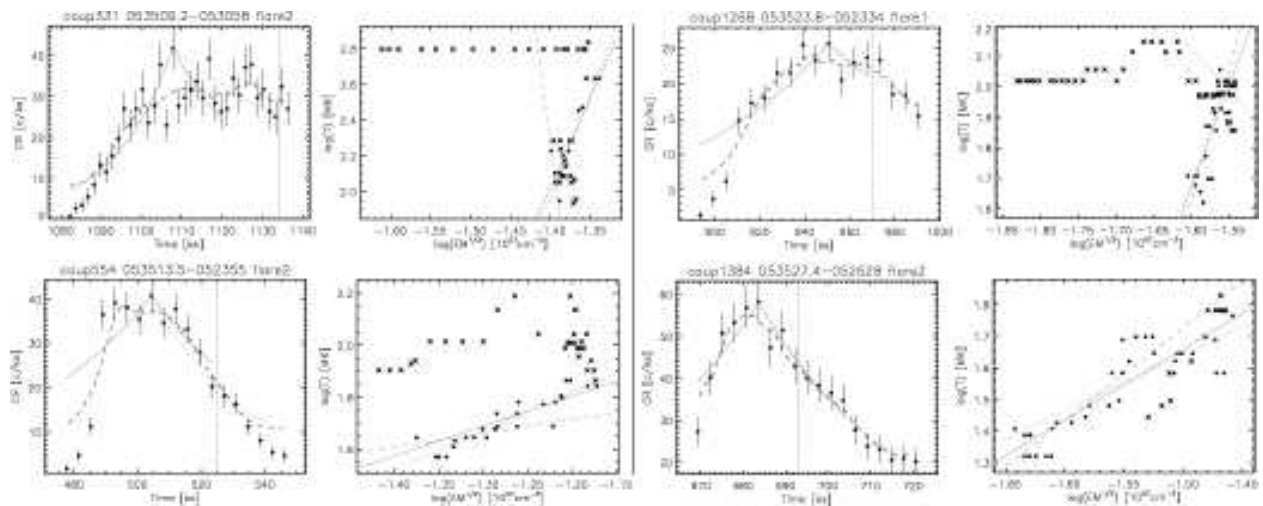


Fig. 5.— Lightcurves and inferred temperature-density trajectories for four representative flares in the class “slow-rise-and/or-top-flat”.

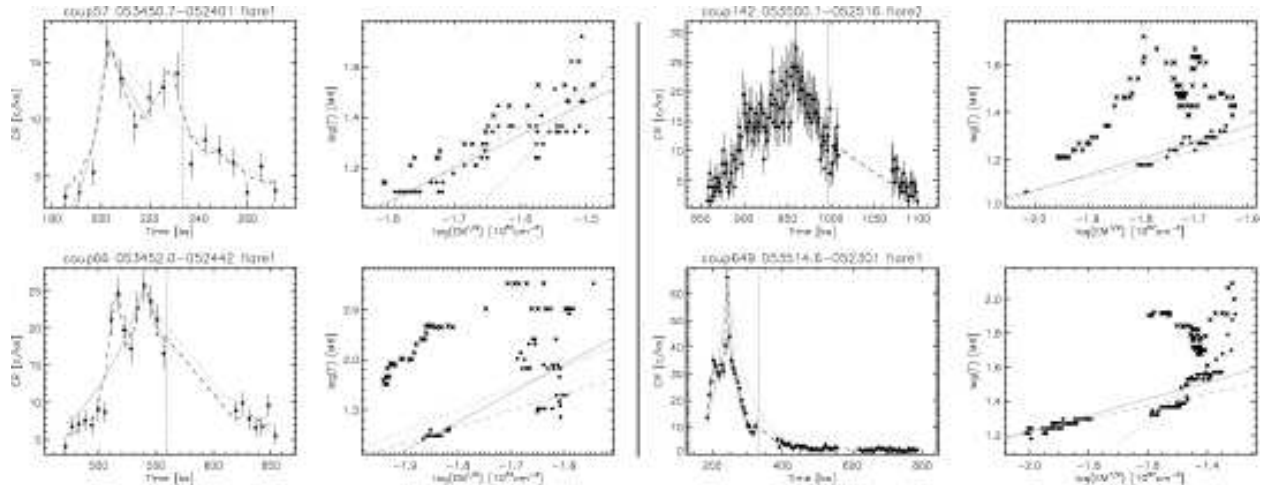


Fig. 6.— Lightcurves and inferred temperature-density trajectories for four representative flares in the class “double”.

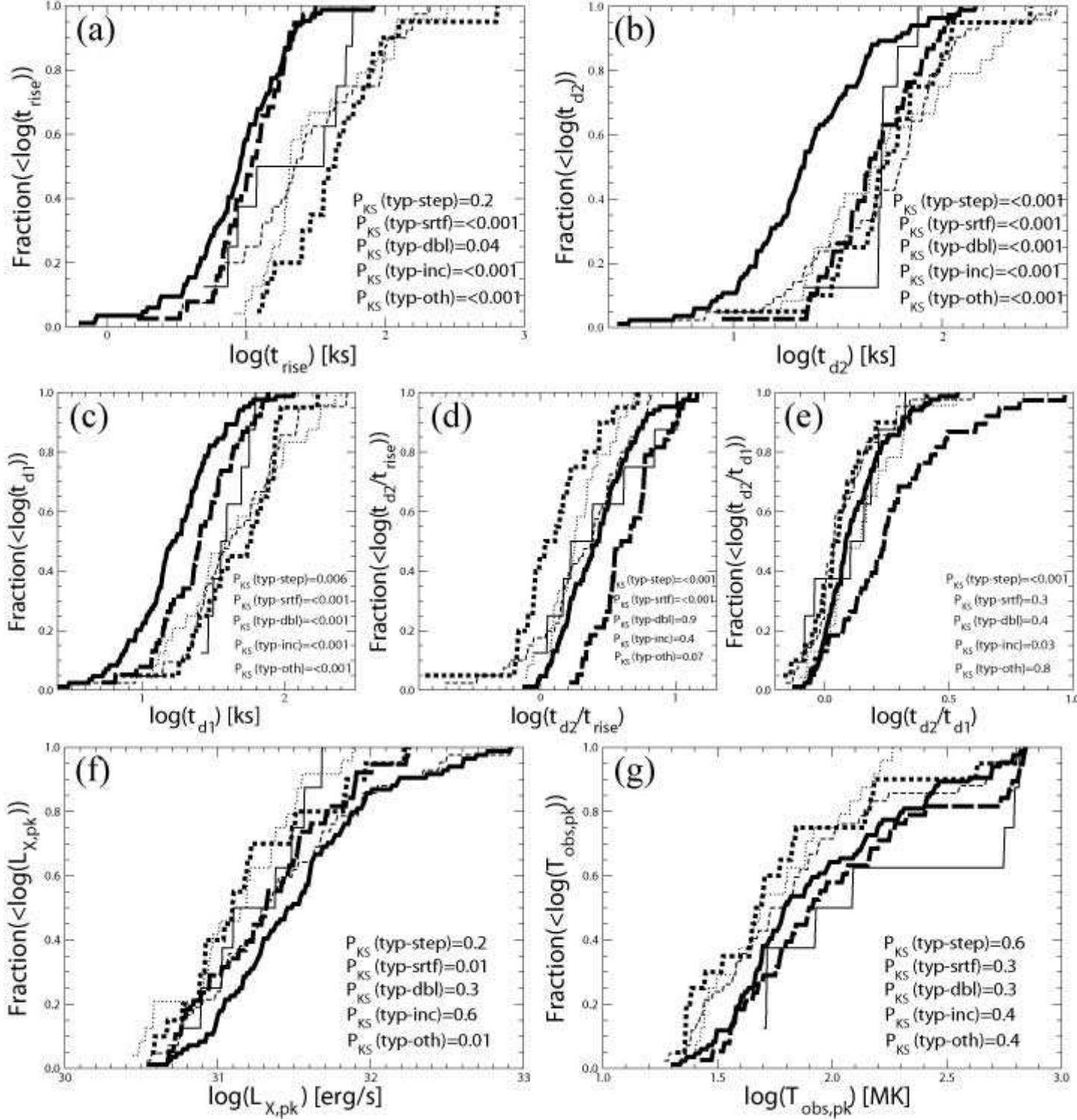


Fig. 7.— Cumulative distributions of flare properties: (a) rise time τ_{rise} , (b) decay time τ_{d2} , (c) decay time τ_{d1} , (d) ratio $\tau_{d2}/\tau_{\text{rise}}$, (e) ratio τ_{d2}/τ_{d1} , (f) peak luminosity, and (g) peak temperature. Line types indicate morphological classes: 84 “typical” flares (thick solid line), 38 “step” (thick dashed), 20 “srtf” (thick dotted), 8 “double” (thin solid), 42 “incomplete” (thin dashed), and 24 “other” (thin dotted). K-S probabilities test the assumption that “typical” and other flare types are drawn from the same underlying distribution.

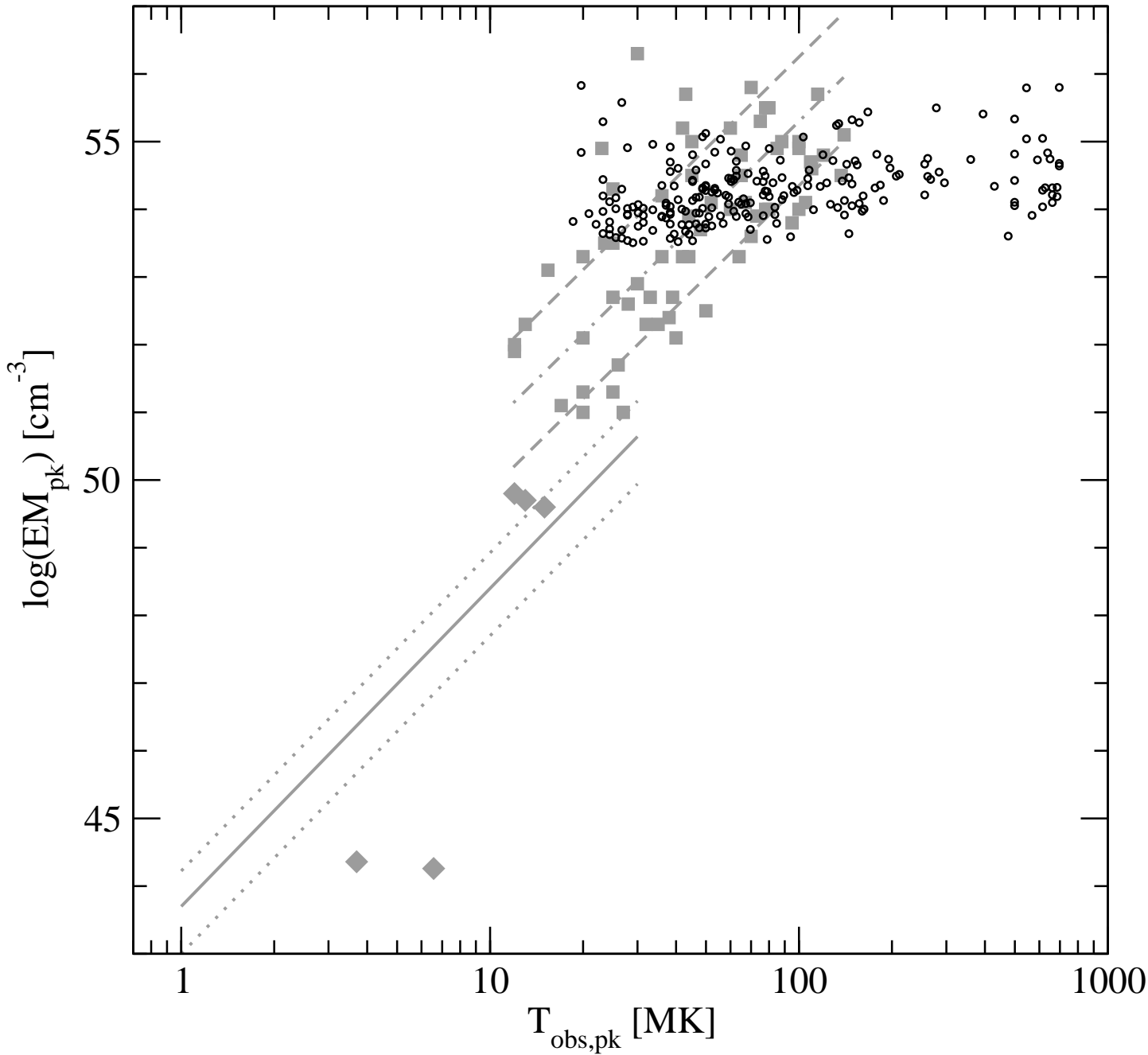


Fig. 8.— Plot of flare peak emission measure *vs.* peak temperature for different flare classes: 216 COUP flares (black circles); stellar flares compiled by Güdel (2004) (grey boxes) with their linear regression fit and 1σ -ranges (dashed-dotted and dashed lines); and the regression fit to solar flares compiled by Aschwanden et al. (2008) (solid and dotted lines). Representative solar LDEs discussed in the text are shown as grey diamonds.

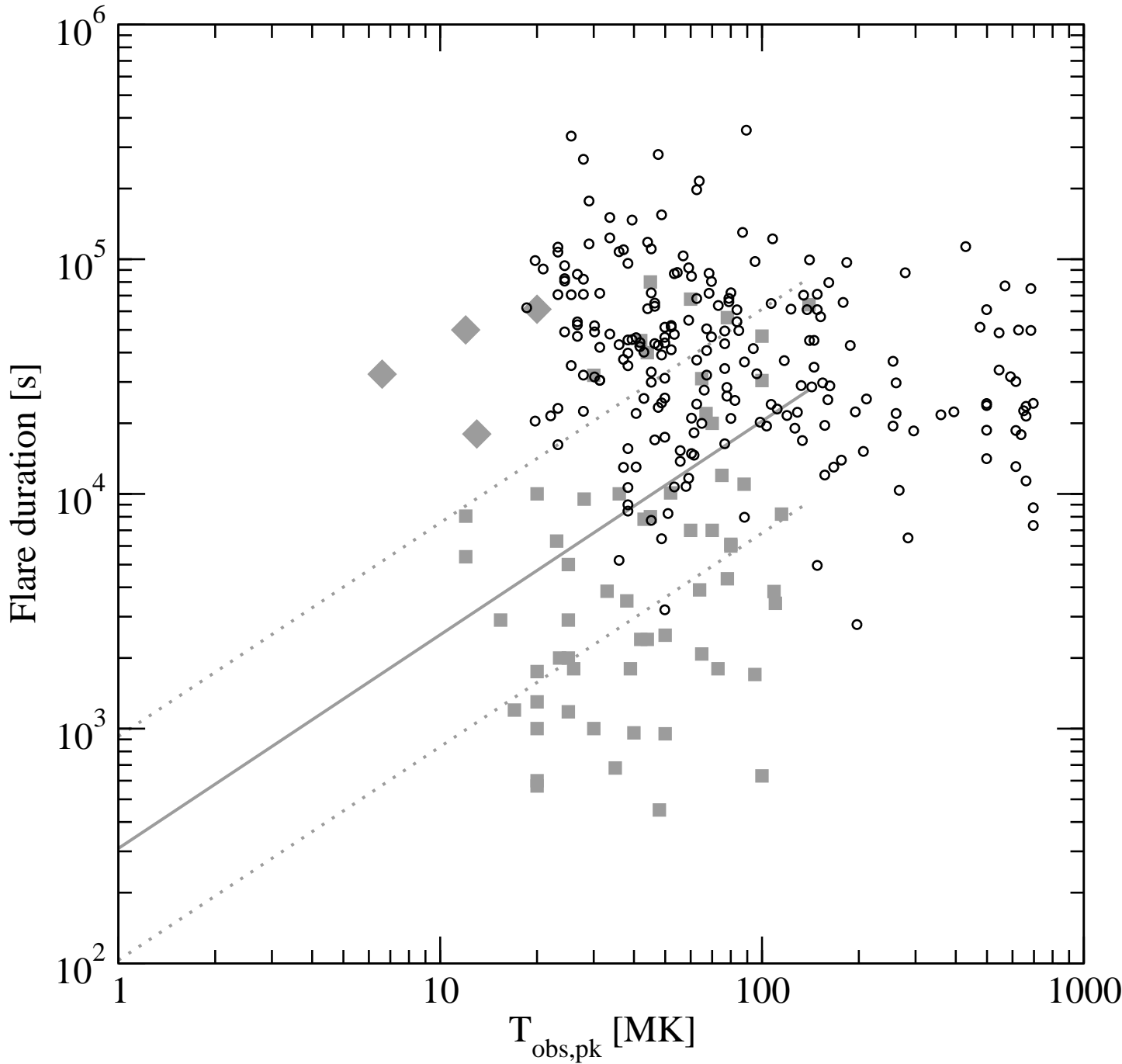


Fig. 9.— Plot of flare duration *vs.* flare peak temperature for different flare classes. Symbols and lines follow those of Figure 8.

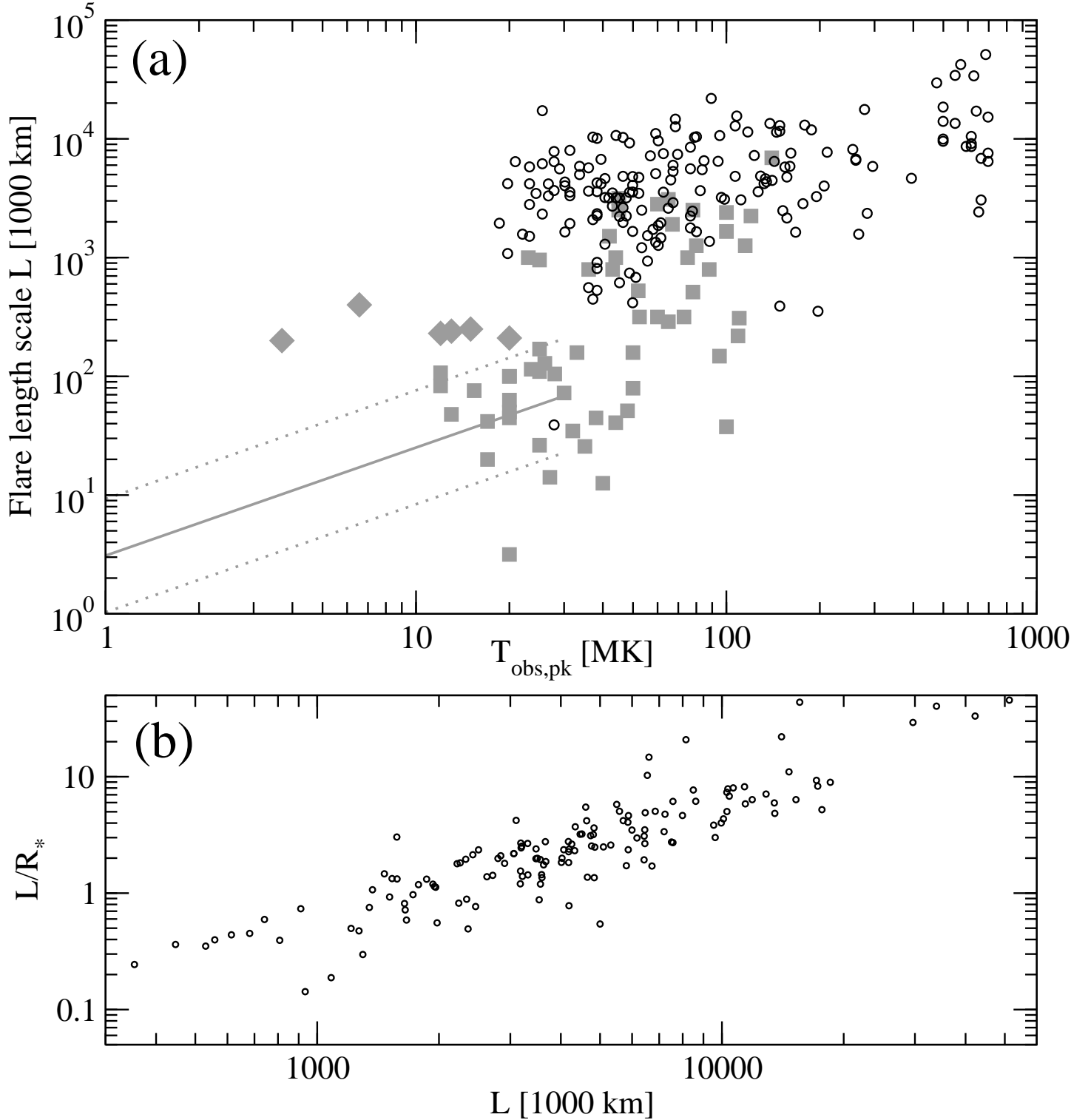


Fig. 10.— (a) Flare length scale *vs.* flare peak temperature for different flare classes. Symbols and lines follow those of Figure 8. (b) Comparison of inferred COUP flaring loop length to the loop length normalized by stellar radius (L/R_*) for 147 COUP stars with known radii.

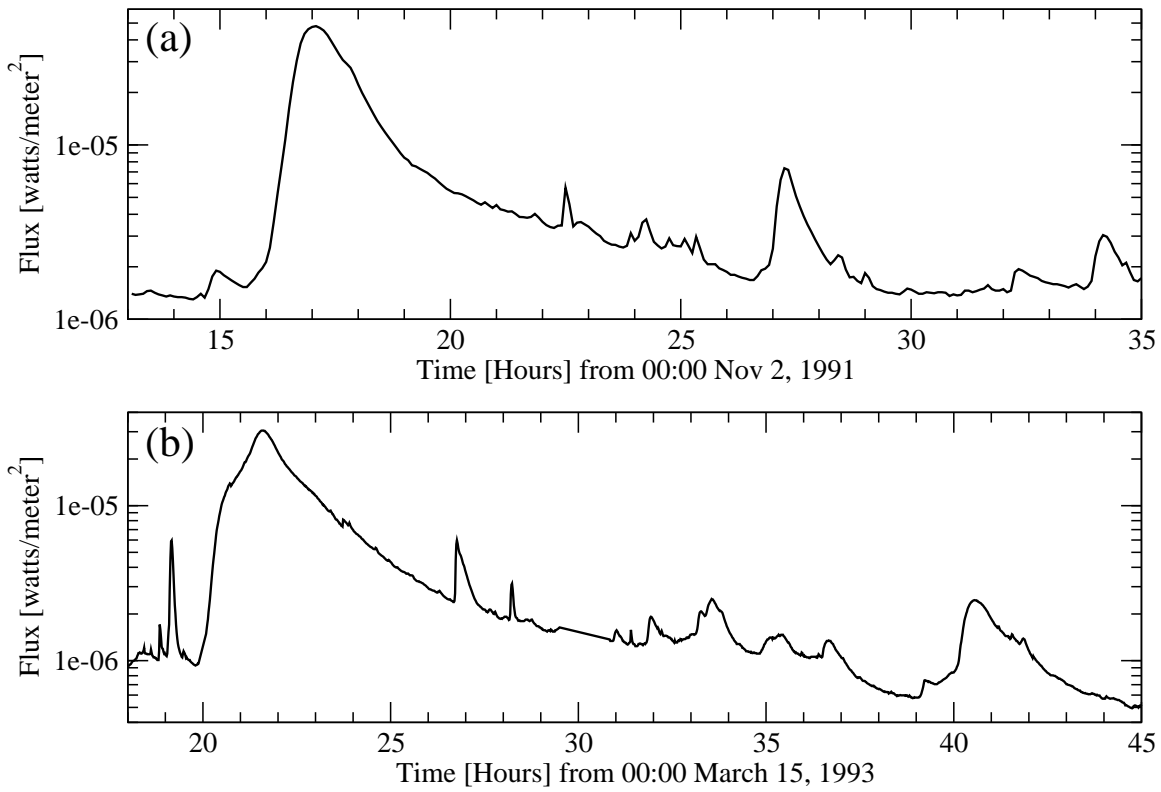


Fig. 11.— X-ray lightcurves obtained in $1 - 8 \text{ \AA}$ band by GOES satellites during formation of giant solar X-ray arches (Švestka et al. 1995) on: (a) 2 Nov 1991, and (b) 15 Mar 1993.

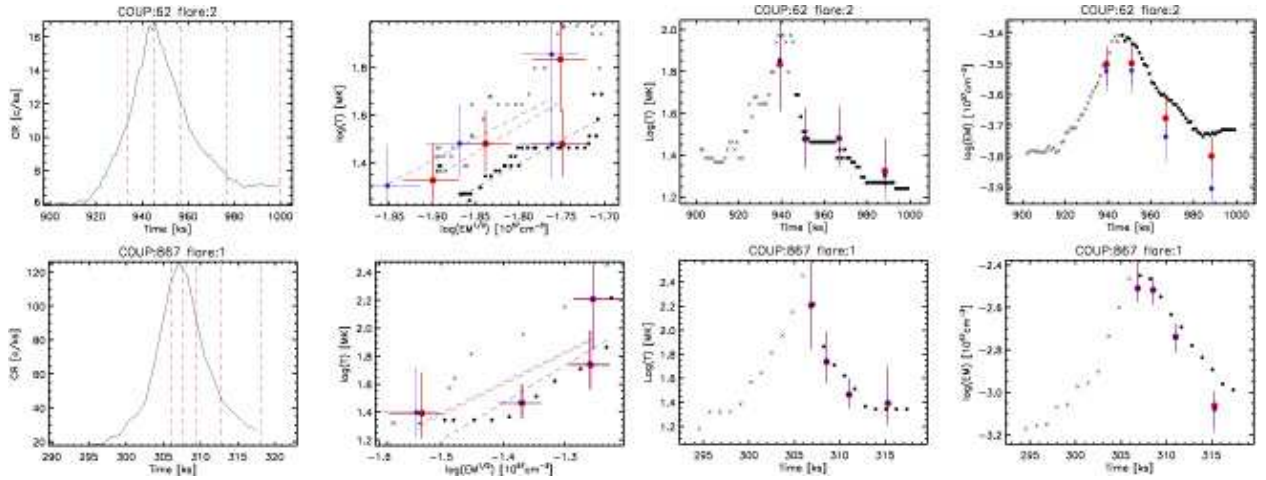


Fig. 12.— Comparison of MASME and TRS flare analyses for representative “typical” flares with 4 TRS segments. Each source is represented by four panels (from left to right): adaptively smoothed lightcurve with dashed red lines indicating TRS segments; $\log(T) - \log(EM^{1/2})$ diagram; temporal evolution of plasma temperature; and temporal evolution of emission measure. Black circles (\times s) indicate MASME-derived decay (rise) points. Blue (red) circles with error bars are TRS-derived points for the peak-decay lightcurve phase with (without) accounting for the “characteristic” background. Dashed lines are linear regressions to MASME points over the whole decay phase (black; denoted as slope ζ_1 in Table 2) and to TRS points over the peak-decay phase (blue and red for the “CH” and “noCH” cases, respectively).

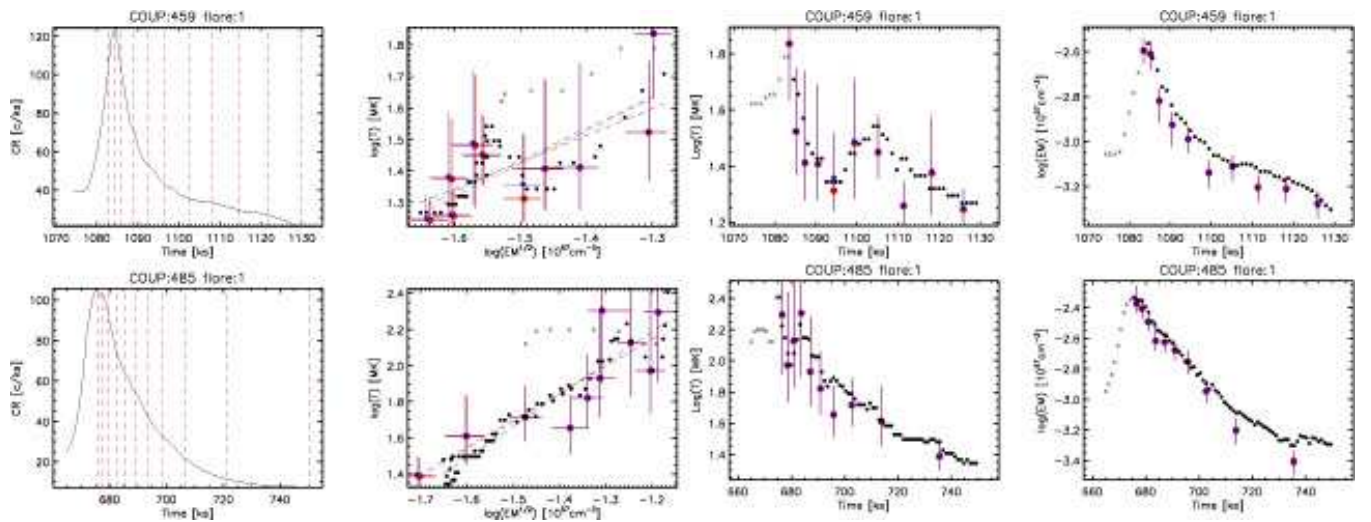


Fig. 13.— Comparison of MASME and TRS flare analyses for representative “typical” flares with 10 TRS segments. See Fig. 12 for details.

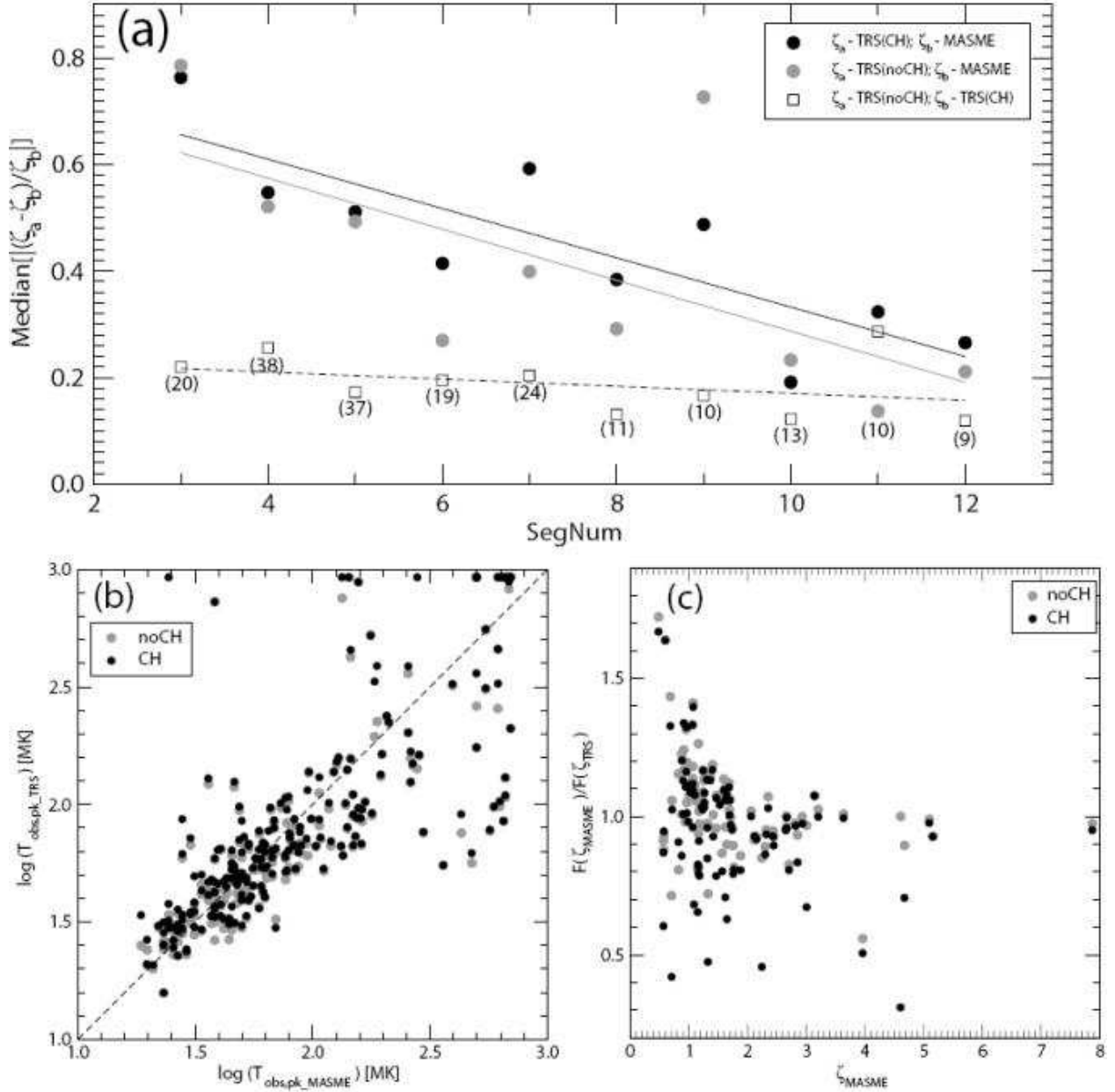


Fig. 14.— Comparison of MASME and TRS flare analyses results. (a) Median fractional difference between inferred slopes in the $\log(T) - \log(EM^{1/2})$ diagram as a function of number of TRS segments. Black circles indicate correction for “characteristic” background emission (“CH”) while grey circles indicate no correction (“noCH”). Open boxes indicate median fractional difference between TRS “CH” and TRS “noCH”. Lines represent linear regressions of the data points. Numbers in parentheses report the number of flares that have the specified number of TRS segments. (b) Comparison between MASME- and TRS-inferred peak flare temperatures. (c) Ratio of the MASME to TRS correction factors $F(\zeta)$ for prolonged heating (see §2.3) versus the MASME slope.

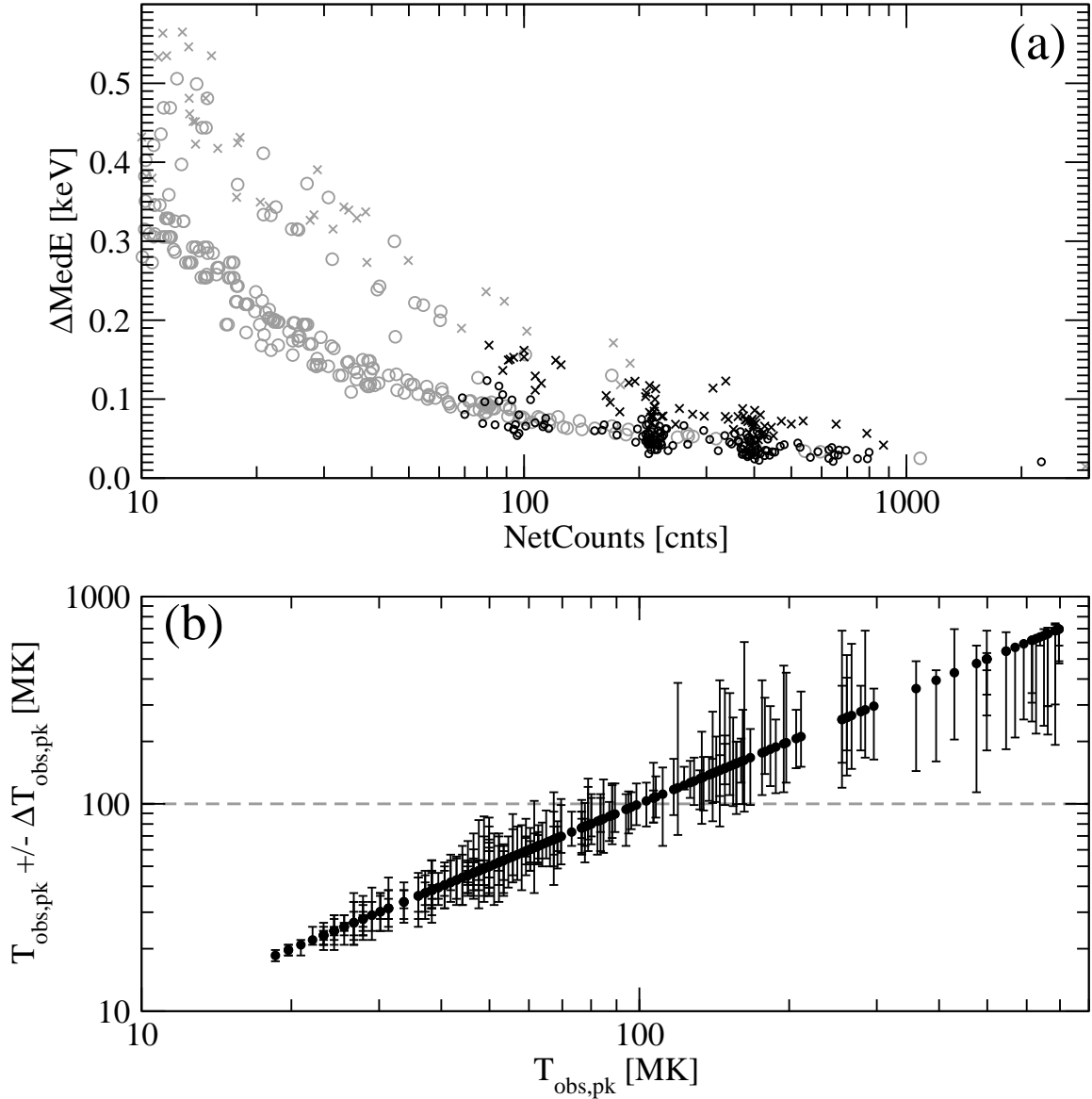


Fig. 15.— Validation of median energy and peak temperature estimates. (a) Comparison between 1σ errors on median energy obtained from Monte-Carlo simulations of Cepheus B X-ray sources (grey symbols from Getman et al. 2006) and errors derived from the MAD technique applied to COUP flaring sources (black symbols). Circles indicate $\text{MedE} < 2$ keV and crosses indicate $\text{MedE} > 2$ keV. (b) Errors on peak flare plasma temperature derived for our COUP flare sample based on the median energy calibration curve in Figure 1. Upper errors on $T_{\text{obs},\text{pk}} \gtrsim 300$ MK are unreliable due to the lack of calibration data points above 700 MK .

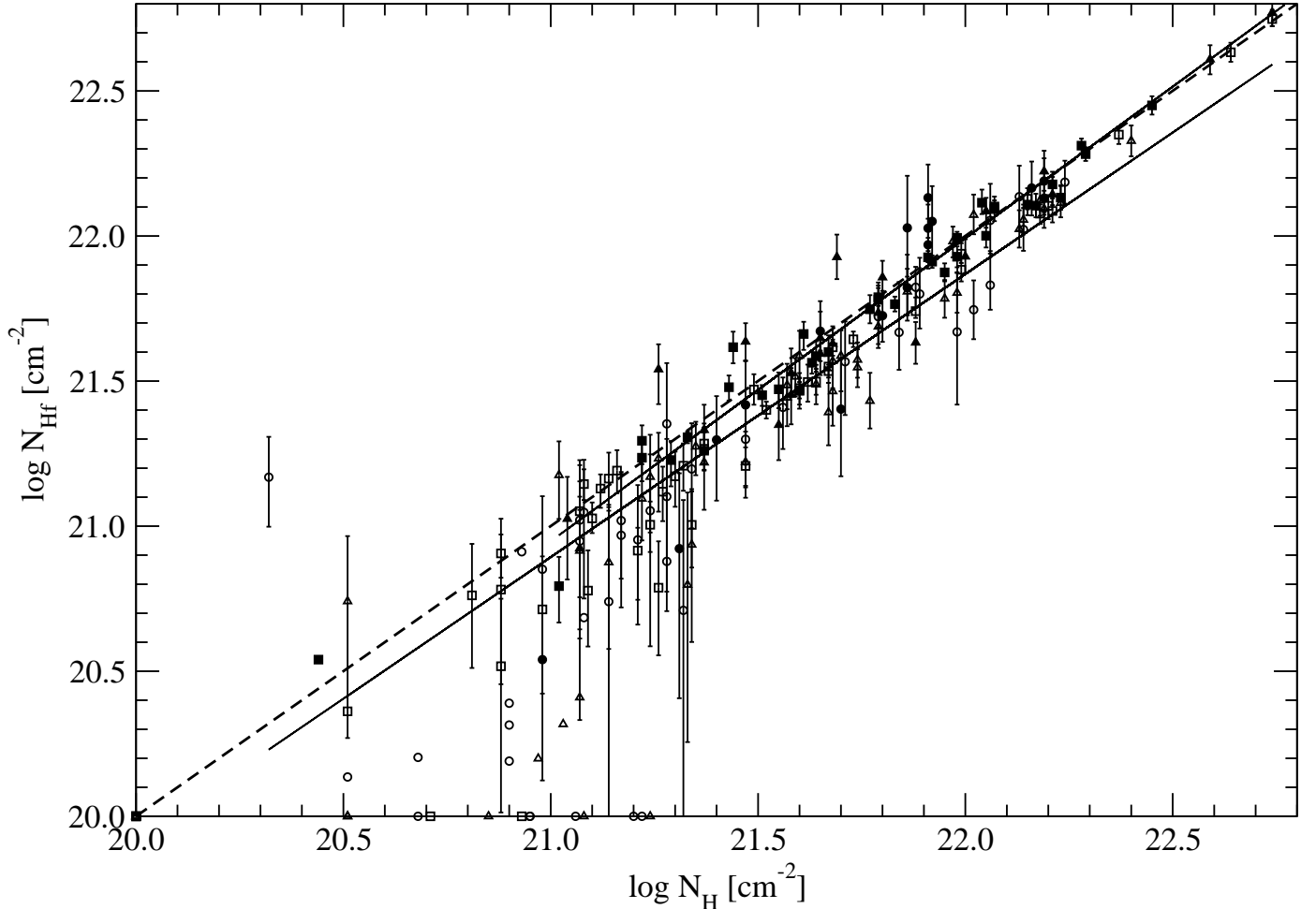


Fig. 16.— Comparison of column densities derived here from fits of flare spectra, N_{Hf} , with column densities (Getman et al. 2005a) derived from fits of time-integrated COUP spectra (within the whole COUP observation), N_H . Symbols represent different flare counts: circles ($NCf < 1000$), triangles ($1000 < NCf < 2000$) and squares ($NCf > 2000$). Filled symbols denote 73 super-hot flares. The dashed line shows values of $\log(N_{Hf}) - \log(N_H) = 0$. The shorter solid line is a regression line to all super-hot flares with known formal statistical errors on N_{Hf} (vertical bars). The longer solid line is a regression line to all cooler flares with known errors.